Aus der Radiologischen Universitätsklinik Tübingen

Abteilung Präklinische Bildgubung und Radiopharmazie

Development of a Quantitative PET/MRI Method to Simultaneously Measure β-cell Mass and Function

Inaugural-Dissertation
zur Erlangung des Doktorgrades
der Humanwissenschaften

Der Medizinischen Fakultät
der Eberhand Karls Universität
zu Tübingen

vorgelegt von

Michelotti, Filippo Carlo

2022

Dekan:	Professor Dr. B. Pichler
1. Berichterstatter:	Professor Dr. B. Pichler
2. Berichterstatter:	Professor Dr. K. Scheffler
Tag der Disputation:	03.05.2022

Table of Contents

List of Figures

List of Tables

Abbreviations

%ID/mL	percentage of injected dose per milliliter
%S.E.	percentage of signal enhancement
[Mn]	concentration of manganese
[^{18}F]FDG	2-deoxy-2-^{18}F-D-glucose
3D	three-dimensional
5-HT	serotonin
5-HTP	5-hydroxytryptophane
ACD	annihilation coincidence detection
APUD	amine precursor uptake and decarboxylation
B_0	external magnetic field
B_1	RF-coils gradient fields
BCM	β-cell mass
BSA	bovine serum albumin
BW	bandwidth
Ca	calcium
cAMP	adenylyl cyclase
CNS	central nervous system
DA	dopamine
DMSO	dimethyl sulfoxide
DOPA	3,4-dihydroxyphenilalanine
DPDP	dipyrodoxyl-diphosphate
DPP-4	dipeptidyl peptidase-4

DTBZ	dihydrotetrabenazine
EDTA	ethylenediaminetetraacetic acid
Ex4	Exendin-4
FA	flip angle
FID	free induction decay
FLAIR	fluid attenuation inversion recovery
FoV	field-of-view
GABA	γ-amino butyric acid
GAD	glutamic acid decarboxylase
GIP	gastric inhibitory polypeptide
GLP	glucagon-like-peptide peptide
GLP-1R	glucagon-like-peptide-1 receptor
GPCRs	G-protein-coupled receptors
G_{phase}	phase gradient field
GRE	gradient-echo
G_{read}	frequency gradient field
G_{slice}	slice selection gradient field
g	grams
HEPES	4-(2-hydroxyethyl)-1-piperazineethanesulfonic acid
h	hour
i.p.	intraperitoneal
i.v.	intravenous
LA-ICP-MS	laser-ablation inductively coupled plasma mass spectrometry
IA	injected activity
IHC	immunohistochemical
INS-1	rat insulinomas 1

IRSE	inversion-recovery spin-echo
keV	kiloelectronvolt
KRH	Krebs-Ringer-HEPES
LAT	large amino acid transporters
M_0	magnetization at the equilibrium
MAO-A	monoamine oxidase-A
MBq	megabecquerel
ME	manganese-enhanced
MIP	maximum intesity projection
Mn	manganese
MRI	magnetic resonance imaging
MSI	mass-spectrometry imaging
M_{xy}	magnetization in the transversal plane
M_z	magnetization in the longitudinal plane
NA	number of acquisitions
NET	neuroendocrine tumors
OSEM	ordered-subset-expectation maximization
PBS	phosphate buffer solution
PET	positron emission tomography
PMT	photomultipliers tubes
PP	pancreatic polypeptide
C2	quinoxaline
r	Paerson's correlation coefficient
r_1	longitudinal relaxivity
R_1	relaxation constant rate
RF	radiofrequency
RPM	revolutions per minute

RPMI	Roswel Park Memorial Institute
ROI	region of interest
S.I.	signal intensity
SD	standard deviation
SE	spin-echo
SPECT	single-photon emission computed tomography
SSE	sum-squared-error
STIR	short-tau inversion recovery
STZ	streptozotocin
T_1	longitudinal relaxation time
$T_{1/2}$	half-life time
T1D	type-1 diabetes
T_1-w	T_1-weighted
T_2	transversal relaxation time
T2D	type-2 diabetes
TE	time of echo
TI	time of inversion
TR	time of repetition
TSE	turbo-spin-echo
VDCC	voltage-dependent calcium channels
VFA	variable flip angle
VMAT	vesicular monoamine transporters
VOI	volume of interest
Zn	zinc

Dedication

I dedicate this work to my family. First, to my grandfather, Giorgio Lapidari, who I have deeply admired for his righteousness and endless kindness.

I am thankful to my loving parents, Laura and Bruno, who gave me strength and encouraged me during the most difficult times of my life. A special feeling of gratitude to my partner Jule and her family, who supported me in this over several years.

I remember the people of the Schranne a second family during my stay in Tübingen. I also would like to thank my colleagues and friends, Chamba, Greg, Hanna, Prateek, Johnathan, and Sabina for the extraordinary good time spent together and for their sincere support.

This dissertation is dedicated to the memory of my friend for life Marco, whose love for nature I will always carry with me.

1 Background

In the following sections some important steps and recent achievements in life sciences, medicine and imaging technologies are reviewed aiming to investigate the role of islet β-cells in the pathophysiology of diabetes.

1.1 Islet Cell Biology

1.1.1 Brief History of the Endocrine Pancreas

A German medical student described the endocrine pancreas for the first time in 1869. In his dissertation, “Beiträge zur mikroskopichen Anatomie der Bauchspeicheldrüse“ (“Contribution to microscopic anatomy of the pancreas“), Langerhans referred to clustered cells with a denser innervation system in the surrounding sea of acinar cells (Ceranowicz et al., 2015, Sakula, 1988). Laguesse, in 1893, by referring to “*Les ilôts de Langerhans*” (Laguesse, 1893) associated the capillary network of islets to their ability to secrete substances that influence the metabolism of sugars. Later in 1923, Banting and Macleod received the Nobel Prize for their studies on the role of insulin in the reduction of the blood glucose levels in diabetic dogs (Myers and Bailey, 1916). Following, Banting, Best and Collip demonstrated the efficacy of highly purified insulin as a therapeutic agent in diabetic patients (Banting et al., 1922).

1.1.2 The Islet-Cell Types

The development of methods for the identification of different islet cell subpopulations has been a major research interest of the last century. In 1908, Lane, by using chrome sublimate staining, was the first to demonstrate the presence of two islet cell types, α- and β-cells, based on the solubility in alcohol of their respective cytoplasmic granules (Fig. 1.1.1) (Lane, 1907).

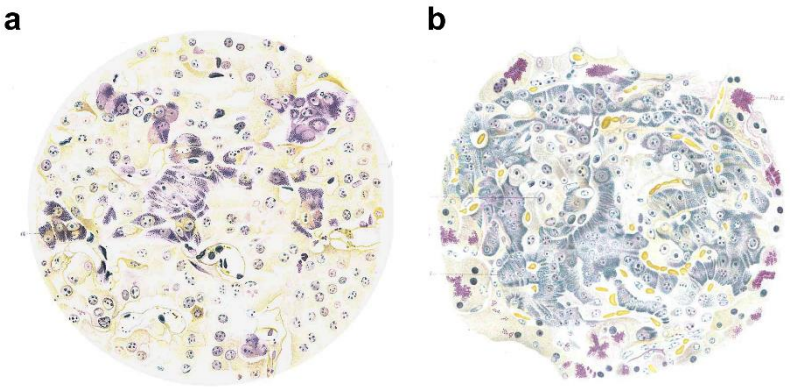

Fig. 1.1.1 Islet Langerans cytology

Drawing of the sections of an Islet of Langerhans from the Guinea pig fixed in (**a**) 70 percent of alcohol (α-cell stained in violet) or (**b**) fixed with aqueous chrome-sublimate (β-cell stained in blue) following Bensley's Neutral Gestian staining. The figure is adapted from Lane et al. (Lane, 1907).

When the role of pancreatic islet cells was still unknown, it has also been suggested that the granular content was associated with the distinct secretory function of cell types in the regulation of carbohydrate homeostasis. In the first half of the 20th century, various formulations of "Gomori's stain", based on the oxidation of cysteine disulphide groups of insulin (Barrnett and Seligman, 1952, Gomori, 1941, Schiebler and Schiessler, 1959), allowed to differentiate pathological β-cells in human pancreas sections. Bloom (Bloom) and later Hellman and Grimelius (Grimelius, 1968, Hellman and Hellerstrom, 1961) confirmed the presence of a third islet cell type (denominated D cells and later δ-cells), which induced the reduction of silver nitrate to metallic silver in presence of formaldehyde and, for this characteristic, were denominated 'argyrophilic cells'.

The advent of immunohistochemical (IHC) techniques (Coons and Kaplan, 1950) improved the identification of islet cells. Nowadays, five islet cell types are known including glucagon-producing α-cells (Baum et al., 1962), insulin-producing β-

cells (Lacy and Davies, 1959), somatostatin-producing γ-cells (Hokfelt et al., 1975, Luft et al., 1974), pancreatic polypeptide (PP or ε-cells)-producing cells (Kimmel et al., 1968, Larsson et al., 1974) and ghrelin-producing δ-cells (Wierup et al., 2002).

1.1.3 Ontogeny of Endocrine Cells

While the endodermal origin of the exocrine pancreas was commonly accepted, the origin of the pancreatic islets has been debated for a long time (Andrew et al., 1998). Langerhans himself described them as part of the central nervous system (CNS), due to their dense innervation system. When Pearse introduced the "amine precursor uptake and decarboxylation" concept, he proposed the hypothesis of a neuroectodermal origin, due to the common ability of islet cells and other neural cells to take up and produce precursors of biogenic amine as 3,4-dihydroxyphenilalanine (DOPA) and 5-hydroxytryptophane (5-HTP) through decarboxylation by L-amino acid decarboxylase (Pearse, 1969). He also observed that the islet cells have similar cytochemical characteristics with the endocrine cells of the gastrointestinal tract, adrenal medulla, the pituitary gland, the pancreas and the C-cells of the thyroid gland (Pearse, 1977). Although a common embryological origin has been excluded (Pictet et al., 1976), many studies indicated the importance of neuronal markers for the correct development and maturation of pancreatic islets referred to the "neuroendocrine programming" (Andrew et al., 1998). Those markers include the tyrosine hydroxylase, a rate-limiting enzyme required for the biosynthesis of catecholamines (dopamine, norepinephrine and epinephrine); receptors for the monoclonal antibody A2B5 and tetanus toxin as well as the expression of glutamic acid decarboxylase (GAD), which is involved in the synthesis of γ-amino butyric acid (GABA) (Baekkeskov et al., 1990). Remarkably, the autoantibodies against GAD is currently an important biomarker for the early onset of type-1 diabetes (T1D).

A link between the uptake of biogenic amine and the secretory capacity of neuroendocrine cells has been recently proven to involve the vesicular monoamine transporters (VMAT) regulating the cleavage of prohormone peptides in the intra-vesicle space of β-cells (Blackmore et al., 2001, Boyd, 2001).

1.1.4 The Cytoarchitecture of Islets

The pancreatic islets are micro-organs scattered in the parenchyma of the pancreas: in particular, the endocrine cells can integrate and respond to the internal paracrine signals from other islet cell types, simultaneously to a number of external stimuli such as the presence of nutrients and the autonomous nervous system (Da Silva Xavier, 2018). Among all the endocrine islet cells, the β-cells are still the most studied cell type for their importance in the secretion of insulin and the regulation of the blood glucose homeostasis. The secretion of insulin granules in the extracellular space is mediated by the metabolism of glucose, the depolarization of the plasma membrane and the rises of the intracellular levels of calcium (Hou et al., 2009). Another important aspect to consider is the intra- and inter-species differences of islet structures (Kim et al., 2009, Steiner et al., 2010). Whereas in rodent islets the spatial distribution of β-cells forms a dense core (~85-90%) surrounded by a typical “mantle” of α-cells (~5-10%), human and nonhuman primate islets are composed of a lower percentage of β-cells (~50-60%) which are heterogeneously distributed together with the α-cells (Fig. 1.1.2) (35-45%) along the core and the periphery of islets (Cabrera et al., 2006).

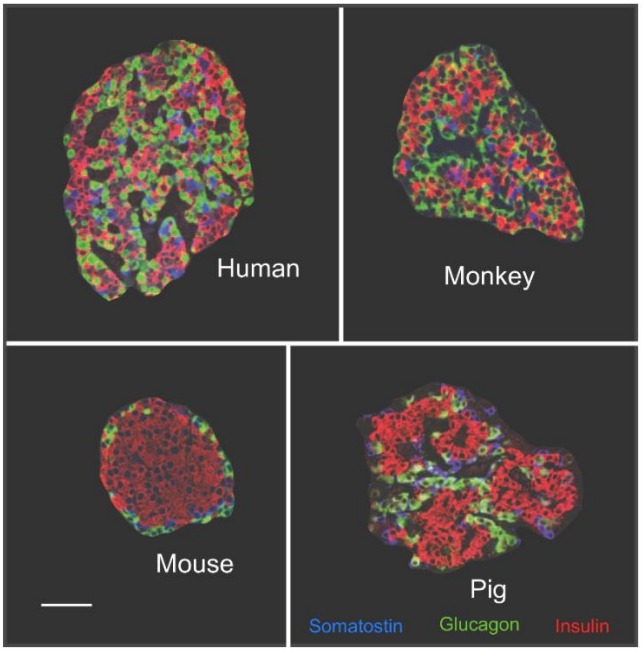

Fig. 1.1.2 Inter-species differences in the islet cell cytoarchitecture

The figure adapted from Cabrera et al. (Cabrera et al., 2006) depicts the confocal micrographs of pancreatic sections containing the islet of Langerhans from human, monkey, mouse and pig. Scale bar set to 50 µm.

Those differences correlated with the islet functionality in the respective oscillatory patterns of calcium in human and murine islets. Further, the nature of human and mouse islet structures differs in their innervation pattern, as the human islets are only barely innervated compared to the mouse islets (Rodriguez-Diaz et al., 2011). Most importantly, changes in the cell composition of islets occur also in response to pathological and physiological conditions, such as diabetes, obesity and pregnancy (Kim et al., 2009), a property so recalled “islet plasticity”. In a recent study investigating the role of single insulin-positive cells, single ‘hub’ β-cells seem to coordinate the response of islet cells (Johnston et al., 2016).

1.2 Diabetes

The term diabetes commonly refers to a disturbance of glucose homeostasis, which ultimately leads to hyperglycemia. The last estimates reported from the International Diabetes Federation accounted more than 400 million patients worldwide with numbers projected to increase up to ~700 million in 2045 (Cho et al., 2018). Only in Europe, almost 60 million cases have already been registered.

Insulin is a main regulator of blood glucose homeostasis and is uniquely synthesized, stored and secreted by islet β-cells of the pancreas. Whereas our organism conserved several mechanisms to elevate the glucose levels, insulin is the unique hormone that can lower the blood glucose levels. This can be explained in evolutionary and historically terms since the survival of species depends on the availability of food (Cantley and Ashcroft, 2015). By contrast, the contemporary sedentary life-style together with the high-sugar diet of the wealthy countries promote the risks that lead to obesity and to the impairment of blood glucose homeostasis.

Only less than 10% of diabetic patients are affected by T1D, characterized by a rapid decline of β-cell mass (BCM) after the autoimmune attack by islet autoantibodies, whereas the majority of the patients develops type-2 diabetes (T2D). This disease has been associated with a progressive dysregulation between the energy consumption, which is demanded from the peripheric tissues, and the capacity of β-cells to secrete insulin (Kahn et al., 2014, Kahn et

al., 1993). The wide heterogeneity of disease observed within the populations implicates that multiple driving factors are involved in the dynamics of diabetes onset. Among those, the genetic footprint and the environmental factors, such as diet and life style, seem to be crucial. Since insulin plays a fundamental role in the regulation of blood glucose homeostasis, lots of research focused on the mechanisms underlying the pathophysiology of β-cells. Recent studies indicate that the alteration of loci associated with β-cell dysfunction (Bonnefond et al., 2010) are crucial for the establishment of pre-diabetic conditions, such as insulin resistance and glucose intolerance (McCarthy, 2010, Scott et al., 2012).

The number of β-cells, mostly referred to as BCM, and their functionality are encoded in our genome and determine the capacity of each individual to correctly synthesize, store and secrete insulin in response to complex stimuli. In this view, low innate BCM and the defects in the production and secretion of insulin contribute to lower the threshold at which β-cell capacity is not sufficient to supply the high metabolic demand of circulating glucose (Cantley and Ashcroft, 2015). It has also been shown that β-cells have low self-replicating abilities and their number, following post-natal expansion, remains relatively constant across the adult life span (Meier et al., 2008, Perl et al., 2010).

In case of insulin resistance, the excess of circulating glucose in the blood stimulates the production and the secretion of insulin from the β-cells in a positive feedback. Whereas this condition contributes to maintain the ‘normoglycemia’ levels, the chronic exposure to high glucose levels represents a major risk for the deterioration of the functionality of the endocrine pancreas (Butler et al., 2003). This condition is transiently triggered in certain periods over the entire life span (e.g., during adolescence, in case of pregnancy and with aging), when the organism demands a higher metabolism of glucose (Amiel et al., 1991, Basu et al., 2003, Buchanan et al., 2002).

Possible causes of β-cell loss, such as apoptosis, oxidative stress, inflammation, amyloid plaque deposition, leading to the disruption of plasma membrane and stress on the endoplasmic reticulum, are currently under investigation (Jurgens et al., 2011, Mukherjee et al., 2015, Poitout, 2008).

A decrease in BCM can be induced by dedifferentiation of β-cells to other islet cell types. New therapies are currently focused on β-cell regeneration by exploiting the plasticity of islet cells to reconstitute the native cytoarchitecture (Chera et al., 2014, Thorel et al., 2010). The most promising approaches include the replication and neogenesis of β-cells from the ductal progenitors and the conversion of α-cells into β-cells (Dunning and Gerich, 2007, Lee et al., 2012, Talchai et al., 2012, Migliorini et al., 2014).

1.3 The Brain-Gut Axis and GLP-1R

On another level, the responsiveness to glucose, the survival and the proliferation of β-cells (and other endocrine cells) depend on the integration of signals between the gastrointestinal tract, the portal vein and the enteric nervous system, a system defined as the Gut-Brain axis.

The discovery of incretin hormones and glucagon-related peptides has been fundamental to understand the regulatory mechanisms involved in the homeostasis of nutrients. In brief, the 'incretin' concept was introduced in 1930 (La Barre, 1930), when La Barre hypothesized that certain humoral substances excreted by the gut in response to meal ingestion produced an increase of insulin secretion. In the following years, the study of incretins attracted a significant attention. The discovery of gastric inhibitory polypeptide (or glucose-dependent insulinotropic peptide, GIP) (Brown, 1971, Dupre et al., 1973, Brown, 1977), and glucagon-like-peptide (GLP) (Kreymann et al., 1987) found potential applications in the treatment of diabetic subjects (Doyle and Egan, 2007).

A fundamental criteria for the definition of incretin hormones is to potentiate the glucose-dependent insulin secretion response (Creutzfeldt, 1979). Interestingly, GIP, glucagon and other glucagon-like-peptides, such as GLP-1 and GLP-2, are all encoded by a single proglucagon gene (Bell et al., 1983, Kieffer and Habener, 1999, Irwin, 2001). Specialized endocrine cells distributed in the gut and brain regions can alternatively express GLP-1, GLP-2, glicentin and oxyntomodulin by post-translation modifications of pre-proglucagon (Rouille et al., 1995). Both GIP and GLP-1 inhibit the gastric emptying delaying post-prandial rises of glycaemia: however only GLP-1 inhibits the secretion of glucagon.

Among the broad range of physiologic effects elicited across the Gut-Brain axis (Baggio and Drucker, 2007, Campbell and Drucker, 2013), GLP-1 promotes β-cell proliferation, neogenesis, and it increases the transcription of insulin gene and the islet sensitivity to glucose. N-terminal truncated GLP-1(7-36) and GLP-1(7-37) (Kieffer and Habener, 1999) act through the activation of class B G-protein-coupled receptors (GPCRs) of the glucagon receptor family. Following the binding with GPCRs, cyclic adenosine monophosphate is produced via

adenylyl cyclase (cAMP), leading to the activation of secondary messengers and the increase of intracellular concentrations of calcium, the opening of voltage-dependent calcium channels (VDCC) and the release of calcium from the intracellular stores (Doyle and Egan, 2007).

Nowadays, the drugs targeting GPCRs constitute approximatively 35% of all the drugs approved by the Food and Drug Administration. A major limitation to the use of native GLP-1 as a therapeutic agent is its short plasma half-life (<2 min). Indeed, GLP-1 has fast kidney clearance and is rapidly metabolized by the dipeptidyl peptidase-4 (DPP-4) and neutral endopeptidase 24.11 through N-terminal sequence recognition (Mentlein et al., 1993).

The main strategies focused on the development of GLP-1R agonists with long plasma half-life, that are resistant to DPP-4 or on inhibiting the clearance of endogenous DPP-4. The first GLP-1R agonist introduced in the clinic for the treatment of T2D was a synthetic analogue of Exendin-4 (Ex4), a 39 aminoacid sequence isolated from the salivary gland of the Gila Monster (Eng et al., 1992). Ex4 showed higher potency and affinity binding to GLP-1R compared to GLP-1. Due to the Ala-Gly substitution at the N-terminal, Ex4 is also resistant to DDP-4 with a longer plasma half-life (2.4 h) compared to the endogenous ligand.

Following studies focused on the development of engineered and conjugated peptides with long-acting insulinotropic properties (Manandhar and Ahn, 2015) and orally active compounds binding GLP-1R (Chen et al., 2007, Knudsen et al., 2007). Interestingly, a subset of substituted quinoxalines molecules, referred to as ago-allosteric modulators, displayed an unusual bell-shape dose-response curve in the production of cAMP after the binding with the human GLP-1R (Knudsen et al., 2007, Sloop et al., 2010). Thus, quinoxaline has theoretically potential applications as co-adjuvant to increase the insulinotropic effects of endogenous ligand by lowering the activation threshold of glucagon-like-peptide-1 receptor (GLP-1R).

To date, a variety of modified GLP-1R analogues, including peptidic and non-peptidic compounds are currently under development with different pharmacodynamic properties (Manandhar and Ahn, 2015).

1.4 β-cell Imaging

Due to the heterogeneity of processes leading to the onset of diabetes, the dynamics and the respective contribution of the loss of BCM and function remain controversial (Chen et al., 2017, Matveyenko and Butler, 2008). The late diagnosis of T2D patients, typically ~10 years after the onset (Harris, 1995), limit the availability of human samples during the progression of disease and the comprehension of the underlying pathophysiological processes.

Nowadays, it is feasible to assess the overall insulin secretory capacity of patients by measuring the plasma concentration of insulin, glucose and C-peptides at steady state (fasting) or at different metabolic conditions (e.g., 15, 30, 60 or 120 minutes after oral/intravenous administration of glucose or insulin). However, those indexes are only indirectly related to β-cell function since they cannot be related to the respective BCM. Although it is broadly accepted that BCM decreases over time, recent studies indicate a large variability between healthy and T2D patients. In this perspective, low BCM does not necessarily seem to lead to the onset of diabetes (Rahier et al., 2008). On the other hand, the presence of viable β-cells with insulin content below the detection limits of the current methods might cause the underestimation of BCM in diabetic patients (Marselli et al., 2014, Meier et al., 2009).

In this scenario, imaging of β-cells holds the tremendous potential to non-invasively follow-up BCM and function longitudinally and, thus, preventing an excessive loss of residual endocrine pancreas. In addition, such a tool in the clinic might outline the risk of developing diabetes in patients displaying glucose intolerance. Despite the great momentum of clinical imaging in oncology, many questions on the signal quantification and the suitability of targets and probes that are specific for β-cells remain unanswered. The heterogeneous distribution of islets throughout the exocrine pancreas together with the very low density (<2% of the total volume of pancreas) and dimension (~150 µm of diameter) constitute an important technical burden. Furthermore, it has been shown that the number of islets is heterogeneous throughout the different pancreatic lobes (Hornblad et al., 2011, Ionescu-Tirgoviste et al., 2015). In case of pathophysiological cases

such as diabetes, tumorigenesis and loss of pancreatic islets, the size and the number of islets throughout the pancreas can be affected (Artinyan et al., 2008, Parween et al., 2016, Wang et al., 2013).

Ideally, both high image resolution and detection sensitivity would be required to quantify and discriminate the signal originated from the scattered islet cells. In practice, numerous trade-offs are defined by using each imaging modality (Andralojc et al., 2012). Although high resolution and sensitivity can be achieved by using optical imaging technologies, the quantification of the signal is often limited by the low tissue penetrance of light emitted from the pancreas (Villiger et al., 2010). Indeed, the trajectories of photons after the excitation of fluorophores are rapidly scattered and absorbed by the organs localized in the abdominal region. The advent of fluorescent probes with wavelength in the near infrared range would improve the sensitivity and detection limits of optical imaging techniques (Hornblad and Ahlgren, 2009). Other *in vivo* studies have shown that confocal microscopy of islet cells transplanted in the eye chamber of small animals is a promising platform to investigate on the functionality of single islet cells (Villiger et al., 2010). However, those methods are not easily transferable into clinical practice.

Alternatively, nuclear imaging techniques, such as positron emission tomography (PET) and single-photon emission computed tomography (SPECT) could be used to quantify picomolar concentrations of the probe. The high sensitivity of PET allows to monitor *in vivo* the specificity and the dynamic distribution of radiolabeled compounds, such as peptides and small molecules, throughout the different organs. Compared to PET, imaging techniques based on high-field magnetic resonance imaging (MRI) benefit of higher tissue contrast with broad applications in the clinic for the anatomical characterization of diseased tissues. Quantitative MRI techniques are implemented in the field of research and in the clinic to investigate a broad range of diseases.

As imaging with different modalities was a major focus of this work, the basics concepts of PET and MRI are briefly introduced in the following sections.

1.4.1 Positron Emission Tomography

PET imaging is a powerful diagnostic scanning technique that can monitor the pharmacodynamics of radiolabeled compounds non-invasively. In addition, the method can provide unique information on the functionality of organs, including blood flow, oxygen consumption and glucose metabolism, thus improving decision-making in the diagnosis and treatment of diseases. The following paragraphs introduce the basic principles of nuclear physics applied to detect radioactive PET tracers.

1.4.1.1 Positron (β^+) Physics

The radioactive decay is referred to the transformation of one nuclear species, 'the parent', into another, 'the daughter'. This spontaneous process results in the conversion of mass into energy, which is mostly imparted as kinetic energy to emitted particles or converted to photons. The type of emission, the transition energy and the average time of the radionuclide before it undergoes radioactive decay are properties that distinguish one radionuclide from another.

The number of radioactive atoms, as well as the activity of a sample containing radioactive atoms, decreases over time by a decay constant (ʎ). For a given ʎ, it is possible to determine the number of radioactive atoms decaying after a certain time. The time required for a radionuclide to decay to 50% of its initial activity is the half-life time ($T_{1/2}$) and is related to the decay constant as follow:

$$T_{1/2} = \frac{\ln 2}{\lambda} \qquad \text{eq. 1.}$$

A positron (β^+) is the antiparticle of an ordinary electron. The decay of β^+ occurs when the daughter nucleus has an excess of protons. The reaction of β^+ decay involves the conversion of the ejected proton into a neutron (*n*), a positively charged electron (e^+) and neutrino and is described by the general equation:

$$p^+ \rightarrow n + e^+ + v + \text{energy} \qquad \text{eq. 2.}$$

The emitted positron loses its kinetic energy in collision with the surrounding atoms, typically few millimeters away from its origin. When the positron collides

with its antiparticle, it shortly combines with an ordinary electron and can form an intermediate atom, called *positronium* before it annihilates.

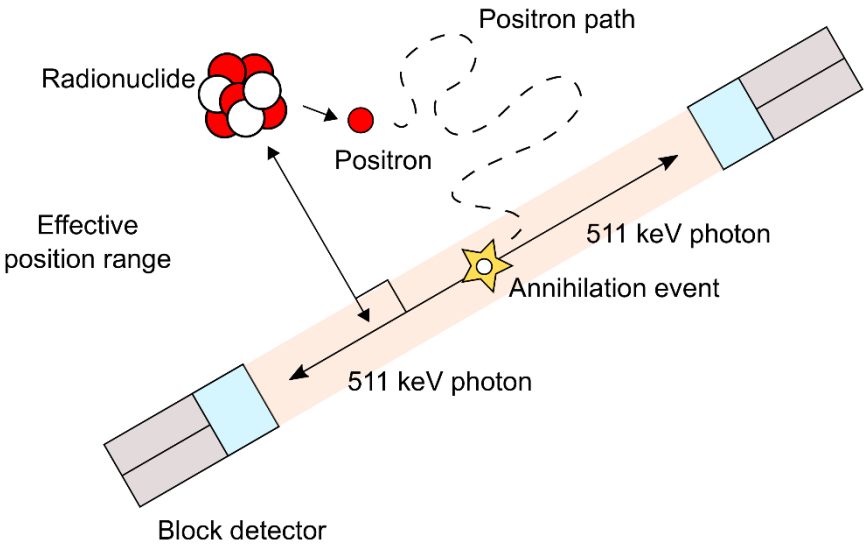

Fig. 1.4.1 Annihilation event and effective positron range

The positron ejected by the decaying radionuclides travels until the collision with its antiparticle is followed by the emission of annihilation photons (511 keV), near 180°, and detected within the areas (red shaded volume) between the two opposed PET detector blocks. The effective positron range defines the average perpendicular between the trajectory of photons and the emitting nucleus. The image was modified and adapted from the book section of Physics in Nuclear Medicine (Cherry et al., 2012a).

This state endures for approximatively 10^{-10} s before their mass is rapidly converted into electromagnetic radiation with an energy equal to 1022 kiloelectronvolt (keV). This reaction causes the decrease of the atomic number by one and therefore resulting in a transmutation of elements, which is represented by the following standard notation:

$$ {}^{A}_{Z}\mathrm{X} \xrightarrow{\beta^+} {}^{A}_{Z-1}Y \qquad \text{eq. 3.} $$

From this annihilation reaction, two 511 keV photons leave the origin in nearly opposite direction (180° apart) that can be detected by two opposite detectors (Fig. 1.4.1). The areas within the two emitted photons are detected is defined as the “line of response” and is typically described as a parallelepiped volume containing all the coincidence events.

1.4.1.2 PET Detectors

The energy of photons is converted into light or electron-hole pairs in the detectors. Dense radiation scintillators are made by several centimeters thick bismuth germanate, lutetium oxyorthosilicate or lutetium yttrium oxyorthosilicate with high stopping power. Detectors are arranged in rings or banks of discrete elements: a block detector consists of a piece of scintillator or crystal segmented in many elements by a fine saw and separated by a reflecting material to avoid light cross-talk between the different segments (Fig. 1.4.2). Nowadays, four individual photomultiplier tubes (PMT), which detects the light emitted by the scintillator, are combined with each block of scintillator to reduce the cost of PMT per detector element.

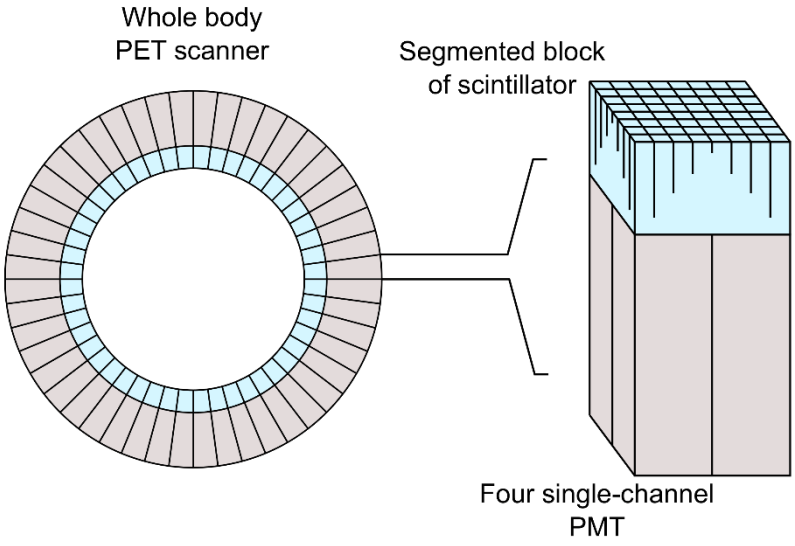

Fig. 1.4.2 PET scanners and block detectors

A trans-axial section of a representative whole-body PET scanner is shown, where each element of the ring consists of a block detector unit. Each segmented crystal block is combined with four PMTs. The image was adapted from the book section Physics in Nuclear Medicine (Cherry et al., 2012b).

1.4.1.3 Annihilation Coincidence Detection

As already mentioned in the previous paragraph, the radioactive decay of positrons results in the emission of two 511 keV γ photons directed in opposing directions (~180°) up to few mm from the emitted nucleus. The simultaneous

detection of the two photons emitted in opposed direction permits the localization of ‘coincidence events’ along a straight line, a method called annihilation coincidence detection (ACD) (Fig. 1.4.1). True coincidences are coincidence events resulting from detection of photons emitted from the same annihilation event. The limit in the coincidence timing window of PET scanners ranges between several hundreds of picoseconds to several nanoseconds, depending on the scanner performance. Due to this error, random coincidences (also called accidental events) are recorded by the detection of photons emitted from two separated annihilation events (Fig. 1.4.3). In this regard, the ratio between random-to-true coincidences increases for increased administered activity.

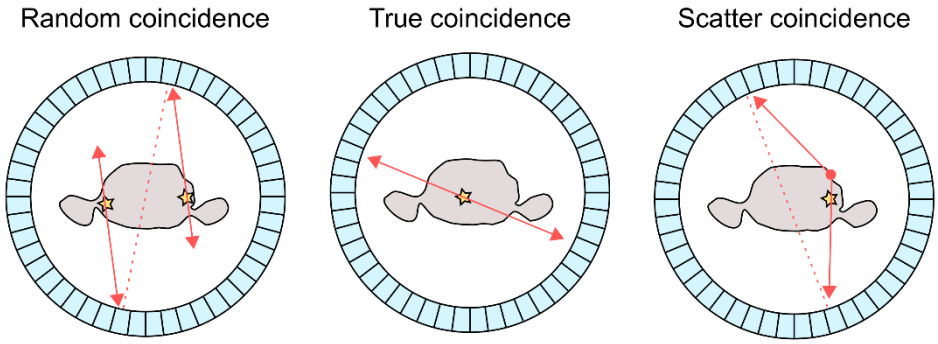

Fig. 1.4.3 Errors in the ACD detection of annihilation events

The figure shows the types of error in the detection of annihilation event (ADC) occurring in case of random and scatter coincidence events compared to the true coincidence events. The image was adapted from the book section Physics in Nuclear Medicine (Cherry et al., 2012b).

Another type of error is the scatter coincidence, which occurs when one or both the 511 keV photons interact with other tissues and, being scattered, are then wrongly assigned to a line of response (see Fig. 1.4.1). This typically leads to an increase of background noise due to the localization of mispositioned annihilation events.

1.4.1.4 Spatial Resolution and Sensitivity

The spatial resolution of PET systems is limited by the detector unit size. Indeed, the detector size defines the dimension of the ACD volume (see Fig. 1.4.1), where the coincidence events took place. Other factors include the range a positron

travels before it annihilates. The effective distance travelled is proportional to the energy distribution of the positrons.

In general, the sensitivity is proportional to the number of counts per unit of activity in the patient. In this regard, it is possible to determine the rate of true coincidence events, which mainly depends of the activity of the emitting source (*E*) and the intrinsic detection efficiency of each detector (*ε*). The geometric efficiency (g_{ADC}) is determined by the position of the emitting source and the two detectors.

$$R_{true} = E\varepsilon^2 g_{ADC} e^{-\mu T} \qquad \text{eq. 4.}$$

The rate of true coincidence (R_{true}) is degraded by the attenuation coefficient of the tissue (μ) and the overall thickness of the object (*T*) (Cherry et al., 2012b).

1.4.1.5 Sampling and Image Reconstruction

The processing of signals is accomplished by addressing to each coincidence event a digital 'time stamp'. Uncertainties in the time resolution mainly arise from the noise in the electronics of detectors and by the detection performance. Two main strategies rely on the reconstruction of images by filter-back-projection or, more recently, by using ordered-subset-expectation maximization (OSEM) algorithms allowing for iterative modelling of datasets. In the latter case, maximum-likelihood estimation of the statistical properties of raw PET data are calculated to produce an image with improved signal-to-noise (Riddell et al., 2001, Tong et al., 2010).

1.4.1.6 Radioactive Tracers

The possibility to synthetically label relevant biochemical molecules using different radioactive nuclei, combined with the high sensitivity of PET instrumentation, allows us to potentially investigate a wide range of biochemical processes (Schlyer, 2004). The radioactive tracers must show the same chemical and physical properties of the non-radioactive compound. Another essential condition required in the design of radioactive tracers is that it does not interfere with the biochemical processes that are under investigation.

The radiolabeling of small molecules is achieved by the direct integration of a radioactive isotope into the molecules. The most common short-life isotopes used for PET are fluorine-18 (^{18}F), carbon-11 (^{11}C), nitrogen-13 (^{13}N) and oxygen-15 (^{15}O), which must be rapidly labeled and imaged to ensure sufficient specific activity.

A particular emphasis is dedicated to 2-deoxy-2-^{18}F-D-glucose ([^{18}F]FDG)-PET. It can provide information on the anaerobic glycolysis of tumorigenic cells and, therefore, with broad applications in the oncology field for the staging of tumor malignancies. However, other methods can radiolabel macromolecules with larger molecular weights, either through labeling with a prosthetic group or using chelators (Jackson et al., 2017). In this regard, using chelators to sequester radioactive isotopes, such as copper-64 (^{64}Cu) and gallium-68 (^{68}Ga) is beneficial for labeling modified variants of peptides that target receptors and epitopes on the surface of human tissue cells. In addition, this approach can be adapted for radiotherapy to deliver high radiation doses to the tumorigenic cells.

1.4.2 Magnetic Resonance Imaging

Given the high abundance of hydrogen nuclei bound to water molecules, MRI can provide detailed information on the anatomical structure of organs at high spatial resolution. In the following paragraphs, the basic principles of MRI physics are briefly introduced.

1.4.2.1 Proton (^{1}H) Net Magnetization

The atoms with unpaired electrons in the orbital produce an intrinsic magnetic moment, where its direction is defined by its spin, that can produce magnetic interactions with its environment. Without an external magnetic field, the "free" protons are randomly orientated (Fig. 1.4.4a). When an external magnetic field is applied, the spin and the magnetic moment of protons tend to orient parallel (lower energy level) and in the same directions of the applied field. At the equilibrium, the difference between the two energy levels (parallel and antiparallel state), produced a small excess of protons that can induce an observable magnetic moment. This magnetic moment is defined as a net magnetization moment (M_0) (Fig. 1.4.4a, b).

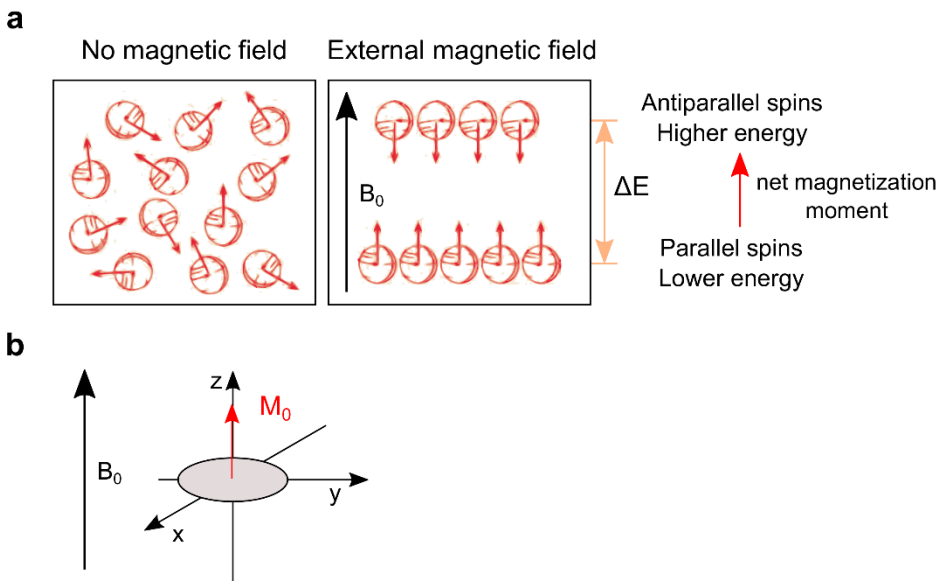

Fig. 1.4.4 The net magnetization moment at the equilibrium (M_0)

(**a**) Protons in the presence of an external magnetic field (B_0) assume a nonrandom orientation, parallel and antiparallel to the applied magnetic field. Since a slight greater number of protons are oriented in the parallel direction, this generates a net magnetization moment oriented in the direction of the applied field. (**b**) In the three-dimensional Cartesian coordinates, x, y and z, where the magnetic moment (M_0) precesses at the

Larmor frequency around the z-axis. The image was modified from the book section of The Essential Physics of Medical Imaging (Bushberg et al., 2012).

The resonance of nuclei is described as the energy coupling produced by the interaction of nuclear magnetic moment of atoms with an external magnetic field. The interaction of a material with the external magnetic field is defined as the magnetic susceptibility. Paramagnetic materials display unpaired electrons and positively interact by slightly enhancing the external magnetic field. Ferromagnetic materials, also known as “superparamagnetic” agents, display a high positive susceptibility as they can strongly increase the amplitude of the external magnetic field and might lead to distortions in the signal due to their self-magnetism. Diamagnetic materials have paired electrons in the electron orbitals and show negative susceptibility as they exhibit an opposed nuclear magnetic moment to the external magnetic field.

1.4.2.2 MR system components

The magnet is a central part of the MR system. A magnetic field can be induced by moving electric charges through a wire, which is typically wrapped many times as a coil to produce a high amplitude current. For higher magnetic field strengths (>1 T), the current-carrying wires are made of superconductive material (e.g., niobium-titanium alloys) and are kept at a very low temperature by using liquid helium to reduce the electrical resistance (Fig. 1.4.5). If the temperature rises over a certain critical value, the wire becomes resistant which ultimately leads to an increase of the temperature and to the “quench” of the magnet.

Other important components are integrated in the MR system. The active shim coils generate field gradients at high temporal stability and are used to reduce the inhomogeneities of the main magnetic field. The magnitude of the fringe field is minimized by passive shielding, consisting of thick plates of soft iron placed outside the main magnet. Further active shielding can be achieved by using additional coils generating a magnetic field with opposite orientation.

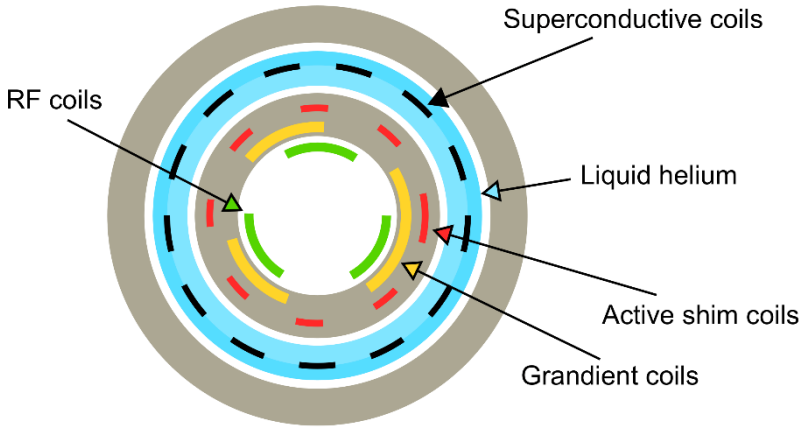

Fig. 1.4.5 MR components

The image illustrates the cross-section of a superconductive magnet and the other components important for maintaining the field homogeneity and for the generation of fast gradients in the three dimensions. The center of the bore hosts the RF-coils that transmit and receive the MR signal. The image was modified from the book section of The Essential Physics of Medical Imaging (Bushberg et al., 2012).

The gradient coils are designed to create stable field variations in the three dimensions at rapid temporal resolution (Fig. 1.4.5). The radiofrequency (RF) coils can be both transmitter of the RF excitation pulse and receiver of the NMR signal.

1.4.2.3 Relaxation effects, T_2 and T_1

To produce an observable MR signal, an additional strong magnetic field is applied by the RF coils at the equilibrium to induce the transition of spins to the higher energy state. Once the RF is switched off, the spins return to the lower energy state producing an amount of radiation at the Larmor frequency (ω). The frequency of the precession of spins (number of rotations/s around the axis) is described by the Larmor equation:

$$\omega = \gamma \cdot B_0 \qquad \text{eq. 5.}$$

In addition to the energy level separation, the applied RF pulse causes the precession of spins in a way proportional to the gyromagnetic ratio (γ) of the nuclei and the magnetic field strength (B_0). The emission of radiation is proportional to the “relaxation” of spins from their excited state. The amplitude

(B_1), the duration (t) and the degree (θ) of the flip angles (FA) of the applied RF excitation pulse determine the undergoing transition of protons:

$$\theta = \omega \cdot B_1 t \qquad \text{eq. 6.}$$

After a 90° RF pulse, the net magnetization moment oriented along the transversal plane (M_{xy}) reach a maximum when the proton spins are in phase coherence. Immediately after the application of the applied RF pulse, the proton spins rotate with the same Larmor (resonance) frequency, followed by the loss of the phase coherence (Fig. 1.4.6a, b). This phenomenon generates the free induction decay (FID) of the signal, which is recorded by the receiver antenna of the coil.

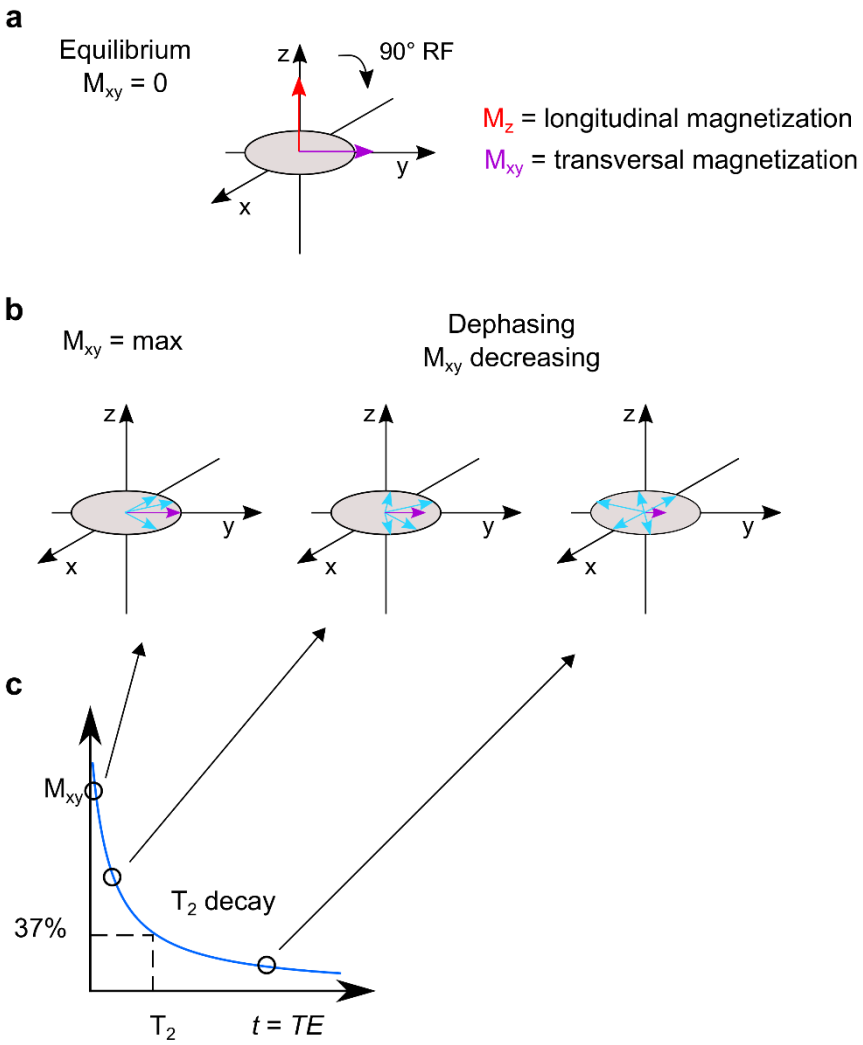

Fig. 1.4.6 Loss of the transversal magnetization

Immediately after a typical 90° RF excitation pulse, (**a**) the net magnetization vector along the z-axis is flipped along the transversal plane. (**b**) At this point the phase coherence is at the maximum (M_{xy}=max), following then by an overtime loss of phase caused by the intrinsic spin-spin interactions with the surrounding environment. (**c**) The exponential decay of T_2 describes the loss of phase of the net magnetization and the consequent loss of signal. At longer time of echo (TE) the resulting signal is lower for protons with fast dephasing processes. The T_2 is the time at which the initial magnetization component is reduced to 37% from the maximum. Images were modified from the book section of The Essential Physics of Medical Imaging (Bushberg et al., 2012).

The time constant that describes the loss of 63% of the transversal magnetization is the T_2 relaxation time (Fig. 1.4.6c), also called *spin-spin relaxation,* which is described by the following equation:

$$M_{xy}(t) = M_0 \cdot e^{-t/T_2} \qquad \text{eq. 7.}$$

Other extrinsic causes such as the inhomogeneities of the B_0, and the susceptibility of paramagnetic and ferromagnetic materials contribute to shorten the decay constant of the transversal magnetization M_{xy}, referred to T_2*. For tissue with amorphous structures, such as the cerebral spinal fluid, the mobile protons have longer dephasing process and T_2 relaxation times. By contrast, the dephasing process occurs more rapidly in presence of structural constrains, such as the protons of the hydration layer surrounding macromolecules in fat or bone tissues.

Contemporary to the dephasing processes, the vector M_z returns to equilibrium along the z-axis (Fig. 1.4.7a). The time constant T_1, or spin-lattice relaxation, describes the time to recover 63% of the initial M_z (Fig. 1.4.7b) after the applied RF excitation pulse:

$$M_z(t) = M_0 \cdot (1 - e^{-t/T_1}) \qquad \text{eq. 8.}$$

The T_1 varies for different tissue structures and on how they can dissipate the energy after an RF excitation. From a classical physics perspective, the energy transfer is maximal when the “tumbling” frequencies of the protons in the water bulk and the hydration layer overlap with the Larmor precessional frequency of the protons. This condition is typical for moderately large proteins and fatty tissues, where the rate of energy transfer is higher and results in shorter T_1 relaxation times (Fig. 1.4.7c).

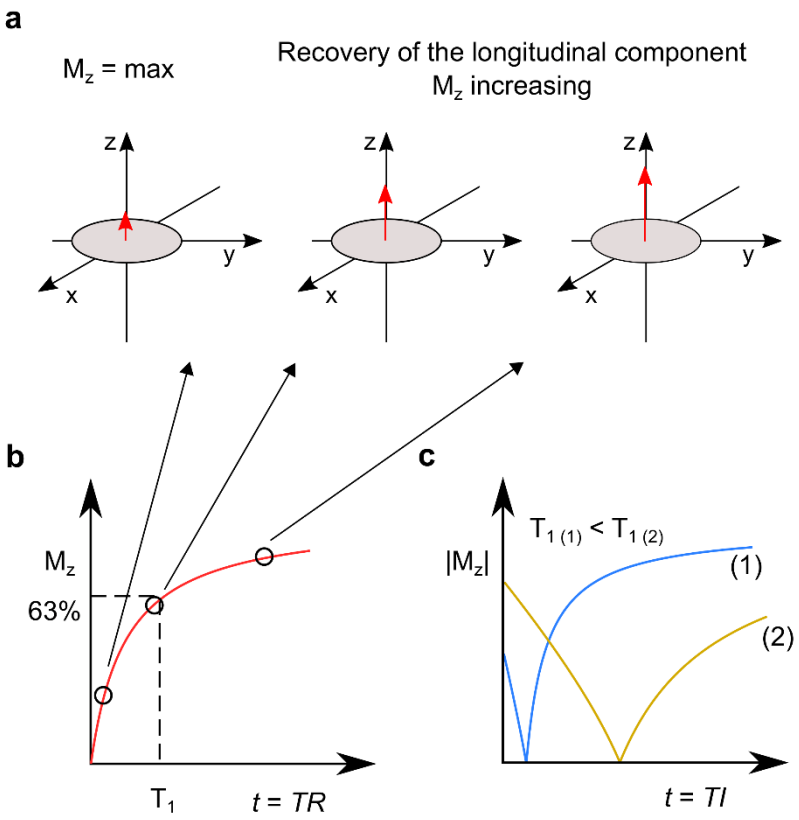

Fig. 1.4.7 Recovery of the longitudinal magnetization

(**a**) The recovery of the longitudinal magnetization (M_z) occurs immediately after an initial 90° RF pulse. The figure depicts the recovery of the M_z components (**b**), where T_1 is defined as the time at which the 63% of the initial magnetization is recovered. The components with lower T_1 will recover the full magnetization along the z-axis at time of repetition (TR) shorter compared to those with slower recovery. (**c**) In the graph are shown the M_z from two representative components, fast (1) and slow (2), which were acquired using an inversion recovery pulse sequence. This method allows a longer recovery time by applying a first 180°-RF pulse applied at different times of inversion (TI) before the first RF-excitation pulse. The images were adapted and modified from the book section of The Essential Physics of Medical Imaging (Bushberg et al., 2012).

1.4.2.4 RF pulses – Spin- and Gradient-echo pulse sequences

To understand the mechanism of contrast some important MR parameters, including the time of repetition (TR), time of echo (TE) and time of inversion (TI) are briefly described.

By referring to a single spin-echo (SE) sequence diagram, the TR is the time between the two 90° RF excitation pulses, therefore it limits the recovery of the magnetization in the longitudinal plane (M_z). The TE is the interval between the RF excitation pulse and the peak of signal following phase coherence of spins in the transversal place (M_{xy}). The phase coherence is induced by a further 180° RF

pulse to revert the phase of spins and cancel the extrinsic inhomogeneities of the main B_0 field (Fig. 1.4.8).

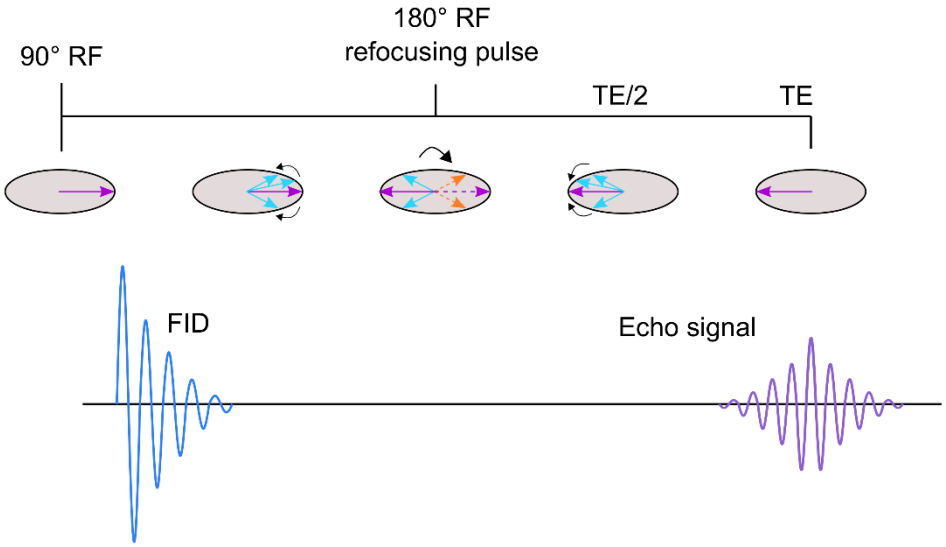

Fig. 1.4.8 Spin-echo pulse sequence diagram

The diagram adapted from the book section of The Essential Physics of Medical Imaging (Bushberg et al., 2012) shows the transversal magnetization (M_{zy}) following a 90°RF-excitation pulse, which induces the generation of FID. A further 180°-RF pulse is applied at TE/2 to induce the coherence of phase and the generation of echo signal at TE.

By “weighting” of those parameters it is possible to produce a variety of tissue-contrasts due to the intrinsic properties of tissues with different proton density, T_1 and T_2 decay.

The TI is defined as the time between the inversion of the M_z using a 180° RF pulse and the excitation pulse. Short Tau Inversion Recovery (STIR) sequences typically use the time of inversion to reduce the signal from the tissue with short longitudinal relaxation times such as in fat tissues. By contrast, Fluid Attenuation Inversion Recovery (FLAIR) sequence are designed with TI allowing the complete recovery of the tissue component with short T_1 while reducing the signal arising from the fluids, such as the cerebral spinal fluid. The saturation and inversion recovery methods are referred as the gold standard for the quantification of the T_1. In general, they consist in the acquisition of sequential weighted images at increasing recovery time by varying TR or TI. Subsequently, the T_1 is calculated by fitting of the signal according to eq. 8.

In case of coherent gradient-echo (GRE) pulse sequences, the phase coherence of spins is re-established by a reverse polarity gradient applied in opposed direction to the slice selective gradient (Fig. 1.4.9).

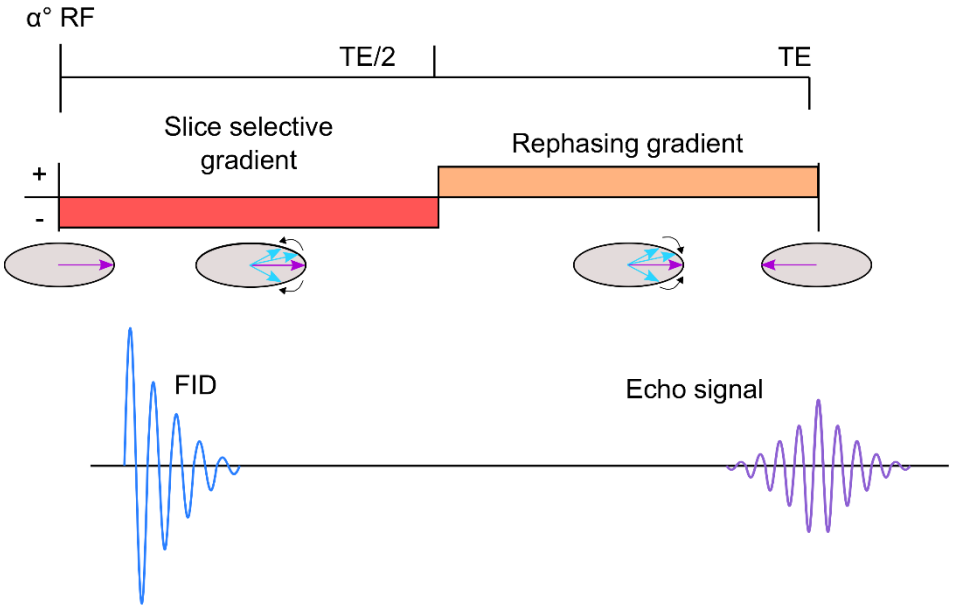

Fig. 1.4.9 Gradient-echo pulse sequence diagram

In a gradient-echo pulse sequence a FID is generated by an initial RF excitation pulse with flip angles (α) typically lower than 60°. As shown in the figure adapted from the book section of The Essential Physics of Medical Imaging (Bushberg et al., 2012), a second gradient applied in opposed direction to the initial slice selective gradient restores phase coherence of the spins and allows the readout of the signal at TE.

Incoherent or 'RF-spoiled' GRE pulse sequence are typically characterized by a very low TR (< 50 ms). The residual components along the transversal plane (M_{xy}) are eliminated by using strong field gradients at incremental phases at the end of each acquisition. Contrasted images in the T_1 are mainly produced by increasing the flip angles and short TE.

The variable flip angle (VFA) approach consists in the acquisition of at least two consecutive RF-spoiled GRE images and, therefore, it represents nowadays a valuable method for the implementation of rapid and quantitative T_1 maps into the clinic. For a determined TR/T_1, the two 'ideal' flip angles are typically set at the 71% of the signal intensity (Wang et al., 1987, Deoni et al., 2003). By contrast, the precision in the quantification of T_1 decreases as the two data points move

away from the peak of the curve, whose signal intensity (S_θ) is described by the following equation:

$$S_\theta = M_0 \frac{(1 - E_1)\sin\theta \cdot E_2}{1 - E_1 \cos\theta} \quad \text{eq. 9}$$

for:

$$E_1 = e^{-\frac{TR}{T_1}} \; ; \; E_2 = e^{-\frac{TE}{T_2}} \quad \text{eq. 10.}$$

This equation can be expressed linearly ($y = a \cdot x + b$) as:

$$\frac{S_\theta}{\sin\theta} = E_1 \cdot \frac{S_\theta}{\tan\theta} + M_0 \cdot (1 - E_1) \cdot E_2 \quad \text{eq. 11.}$$

Thus, by keeping TR and TE constant and varying the flip angle (θ), the slope ($a = E_1$) and intercept ($b = M_0 \cdot (1 - E_1)$) can be calculated by linear regression and the T_1 is calculated as follow:

$$T_1 = -\frac{TR}{\ln\theta} \quad \text{eq. 12.}$$

However, due to the presence of organs in the abdomen with heterogenous relaxation properties, a method using a higher number of flip angles is preferred to improve the quantification of a broader T_1 range.

1.4.2.5 Spatial encoding and k-space

As it has been previously mentioned in this section, the gradient coils can superimpose a stable gradient field to the main magnetic field B_0 and are fundamental to localize the protons within the excited sample. Initially, a slice selective field gradient (G_{slice}) is applied perpendicular to the desired plane and simultaneously with a RF excitation pulse, resulting in the production of the transverse magnetization M_{xy}. The thickness of slides depends on the frequency bandwidth (BW) and the field strength (mT/m) of the applied field.

At this time, a variation in the phase of protons is produced by using an additional phase gradient (G_{phase}) that is applied along the y-axis (k_y). After the refocusing

of phase coherence (typically by a 180° RF pulse at TE/2), a further frequency gradient field (G_{read}) is applied orthogonally to G_{slice} and G_{phase} to produce variations in the precession of protons which are dependent on their position in the x-axis (k_x). Simultaneously with the application of G_{read}, the data are acquired and stored in the *k*-space matrix: the digital data are converted into discrete frequency and corresponding amplitude by a one-dimensional inverse Fourier transformation. The *k*-space can be filled sequentially line-by-line at each increment of the G_{phase}. Alternatively, the phase encoded data are acquired in non-sequential order to fill specific portions of the matrix (e.g. centric *k*-space filling).

1.4.3 Current Strategies for the Development of β-cell Targeting Probes

Testing the specificity of a probe *in vitro* in isolated islets or insulinoma derived cells (INS-1) is often not sufficient. Indeed, following their systemic administration, some important dynamic processes such as distribution, metabolism, unspecific binding and excretion occur within the various organ compartments. The current imaging technologies offer a unique tool to investigate *in vivo* the specificity for the target tissue as well as to determine the accumulation of probes in off-target tissues. Eventually, the end-products of radioactive compounds 'trapped' in specific cell types can be exploited to obtain the signal-to-background and to enable the detection of a certain tissue compartment. The best-known example of 'metabolic trapping' is [^{18}F]FDG, which enters the cells thorough the glucose transporter and then remains trapped inside the intracellular space by escaping the further enzymatic reactions. PET imaging of [^{18}F]FDG finds many applications in oncology and neuroscience, e.g., to determine the metabolism of tumors (Gallamini et al., 2014) or the functionality and the connectivity of brain areas (Soddu et al., 2016).

The validation of imaging probes starts with the *in vitro* characterization using fluorescent molecules or radioactive isotopes as reporters to visualize the cellular localization and to quantify the binding affinity of the ligand with the target. One of the main strategies is blocking of the molecular target using high concentrations of the same non-radioactive compound. Another common approach is the suppression of enzymes that are linked to the metabolism of the radiolabeled compound. *In vivo* studies mainly focus on the direct elimination of the target by chemical ablation or overexpression of the target using genetically modified organisms or xenograft tumor animal models.

The specificity of tracers targeting β-cells is typically demonstrated by IHC staining and autoradiography of insulin-secreting islet cells. Another approach consists in the assessment of islets engrafted in separated anatomical sites, such as the liver, the kidney capsule, the muscle and the eye chamber to exclude the unspecific signal from the exocrine pancreas. A transplanted animal model also

represents a useful platform to develop *in vivo* imaging methods and for optimization of transplantation protocols.

1.4.4 Targets and Probes

Due to the heterogeneous nature of islets and to their diffuse localization throughout the exocrine pancreas, high affinity and specificity of a probe are both required to quantify the signal. The high levels of the biological target expressed by β-cells are also desirable due to the perfusion and the unspecific binding of the probe by the acinar and ductal cells of the exocrine pancreas.

Because of the neuroendocrine nature of pancreatic islets, the development of imaging probes has been based on the translation of neural imaging agents that could specifically target β-cells. *In vivo* imaging of VMAT2 and dopamine receptors located on the surface membrane of β-cells was performed using radiolabeled dihydrotetrabenazine (DTBZ) and fallypride (Garcia et al., 2011), respectively. However, the low expression levels of VMAT2 found in the rodent islets compared to the human's led to controversial conclusions on suitability of this molecular target (Simpson et al., 2006, Fagerholm et al., 2010, Schafer et al., 2013). More recent studies suggested that rodent models could be alternatively considered as 'null' model to exclude the off-target binding due to the unspecific tracer uptake in the sympathetic nerve terminals and mast cells, which were also positive for VMAT2 expression. Regarding DTZB, further studies are still required to demonstrate the specificity for the human islets.

The high turnover of biogenic amides in the pancreatic islets, such as dopamine (DA) and serotonin (5-HT) gated by large amino acid transporters (LAT) have been exploited using radioactive DOPA and 5-HTP and PET (Di Gialleonardo et al., 2012, Eriksson et al., 2014a, Eriksson et al., 2014b). Interestingly, PET imaging of ^{18}F-DOPA is currently in the clinical routine for the localization of neuroendocrine tumors (NET) including the pancreatic insulinomas (Imperiale et al., 2015). The specific uptake of DOPA in β-cells is mediated by LAT and is metabolized to DA by DOPA decarboxylase. Despite the high background decarboxylase activity in the whole pancreas, ^{18}F-DOPA uptake differentiated

between focal and diffuse forms of congenital hyperinsulinemia, such as in case of β-cell hyperplasia and insulinomas (Mohnike et al., 2008).

^{11}C-5-HTP was conceived as a PET neural imaging probe to assess the serotonergic biosynthesis in the CNS. In close relationship with DOPA, 5-HTP is transported by LAT into the vesicle space, where it is subsequently converted to 5-HT and secreted with insulin in the extracellular space. Eventually, 5-HT is transported by VMAT2 and degraded to 5-hydroxyindoleacetic acid by the monoamine oxidase-A (MAO-A) to be finally excreted by the urine. The inhibition of MAO-A activity using clorgyline has been shown to increase the retention of radiolabeled 5-HTP in β-cell-derived tumorigenic INS-1 cells in contrast to a ductal cell line (Di Gialleonardo et al., 2012). The specific accumulation of the tracer has been demonstrated by autoradiography of the pancreas of mice, which were previously treated with clorgyline before the injection of the radiotracer. An unspecific accumulation of the tracer has been observed in the exocrine pancreas of control mice and associated to the enzymatic activity of MAO-A. Since 5-HTP could also be retained by the serotonergic α-cells, the islets of non-human primates and humans, being constituted of higher α-to-β-cell ratio, might show a different metabolism and accumulation of 5-HTP (Eriksson et al., 2014b).

1.4.4.1 GLP-1R Agonists

GLP-1R is the most promising target for the quantification of BCM *in vivo*. As already mentioned in the previous paragraphs, GLP-1R is an important neuro-hormonal receptor as it mediates the action of incretins along the Brain-Gut axis. Nowadays, several isoforms of GLP-1 analogues are currently used in the clinic for the treatment of T2D diabetes to promote insulin secretion response induced by glucose, survival and proliferation of the β-cells.

The high receptor specificity of GLP-1R for β-cells in comparison with other islet cell types and the other cells of the exocrine pancreas paved the way for the development of novel GLP-1 analogues with improved pharmacodynamics. Interestingly, radiolabeled Ex4 has been shown to accumulate specifically into the pancreatic islet cells of rats (Gotthardt et al., 2006). Even if the expression level of GLP-1R in the islet α-cells is still uncertain, a decrease in the

accumulation of the tracer has been shown to correlate with the loss of insulin-positive cells in alloxan-treated mice (Brom et al., 2015). The high signal-to-background from the pancreatic islets is due to the high affinity binding and the internalization of the radiopeptide into the intracellular compartments of β-cells after the binding and the activation of GPCRs (Roed et al., 2014). The ligand-receptor complex can be recycled back to the cell surface, reside in the endosomes, or can be transported and degraded in the lysosomes. Interestingly, the stimulation with Ex4 promotes the internalization of GLP-1R and the co-localization in the intracellular endosomes two to three times longer (up to 60 minutes post stimulation) compared to the endogenous GLP-1 ligand. The internalization of the complex is crucial for the transduction of the cellular response. Ex4 has been also shown to be more efficient compared to the C-terminal truncated form of exendin 9-39, which acts as antagonist at the binding site of GLP-1R, in promoting the internalization of the complex (Brom et al., 2012, Roed et al., 2014). To avoid the endogenous response of peptides targeting GLP-1R, the radiolabeling should be performed at high specific activity and peptide doses not exceeding 0.1 µg per animal.

Recent studies have shown that radiotracers targeting GLP-1R find potential applications in the detection and the follow-up of hidden insulinomas and other GLP-1R expressing tumors, such as in the gut, the lung and the brain (Korner et al., 2007). However, SPECT enabled the localization of pancreatic NETs in transgenic animals only after bilateral excision of the kidneys (Wild et al., 2006). Due to the elevated retention of radiopeptides in the renal cortex, the quantification of radiolabeled exendin derivatives *in vivo* to estimate the endocrine pancreas is still challenging, especially for the tail of the pancreas, lying nearby the left kidney (Connolly et al., 2012b).

At the current state, Ex4 labelled with reporter nuclides for SPECT (^{111}In, ^{99m}Tc) is currently tested in the clinic for the localization of pancreatic insulinomas. At the same time, a variety of GLP-1R agonists labeled with β^+ emitters detectable with PET, such as ^{68}Ga, ^{18}F and ^{64}Cu, are under preclinical development (Brom et al., 2010, Keliher et al., 2012, Mikkola et al., 2014, Xu et al., 2015). Long-lasting radioactive Ex4 labeled with high energy emitting radioisotope has been used as

dual diagnostic and therapeutic ('theranostics') agents showing potential applications in the treatment of localized NETs (Wicki et al., 2007).

To summarize, specific tracers targeting HTP, VMAT2 and GLP-1R are currently under clinical investigations. The large overlap observed between the pancreas measured in healthy individuals and T1D patients might be caused by the wide inter-subject variability and represents a major concern for the interpretation of data (Normandin et al., 2012, Brom et al., 2014, Eriksson et al., 2014a). In this regard, the establishment of standardized and reproducible protocols would enable the comparison of results from multicenter clinical trials. Radiolabeled DTBZ might accumulate in the exocrine pancreas and PP cells expressing VMAT2. Other islet cell types can contribute to a decrease of 5-HTP uptake in T1D patients. By contrast, radiolabeled GLP-1 agonists have been shown to bind the receptors of rodents and human islet cells.

1.4.4.2 Manganese

When electrochemically stable, manganese ions (Mn^{2+}) are used as co-factor for the regulation of endogenous enzymes, such as mitochondrial superoxide dismutase and pyruvate carboxylase. Although manganese (Mn) is an essential metal for the life of our organism, high exposures to this metal have been shown leading to some idiopathic syndromes of Parkinson's disease (Calne et al., 1994), referred to as 'manganism' or 'manganese madness'.

Due to its paramagnetic properties, Mn^{2+} found renewed interest as an MR-contrast agent. The electron spins of its five unpaired valence electrons form a magnetic moment through the alignment of the electron spins with the external magnetic field. The magnetic moment of manganese can alter the T_1 of the ^1H nuclei and, thus, producing a positive enhancement of signal by acquiring T_1-weighted (T_1-w) images.

Recent studies using MRI and PET indicated that the intracellular uptake of paramagnetic manganese is associated to the activity of insulin-secreting cells. Because Mn^{2+} share a similar ionic radius to calcium ions (Ca^{2+}), they can be gated through the voltage-dependent channels into the intracellular space of excitable cells as myocytes, neurons and pancreatic islet β-cells (Silva et al.,

2004). Manganese-enhanced MRI (ME-MRI) emerged as an important tool to assess brain function and neuronal networks. Mn^{2+} can also cross the synapses and be monitored to investigate the anterograde axonal transport (Thuen et al., 2008).

The pre-carboxypeptidase has been shown to bind Mn at high affinity at the catalytical binding site in rats which have been treated with repeated administration of $MnCl_2$ (Kodama et al., 1991). In this respect, the ions of zinc (Zn^{2+}) which are normally used as co-factor by the enzyme can be replaced in presence of Mn^{2+} at high concentrations. Interestingly, disturbances in the absorption of Zn^{2+} have been already linked with a disruption of the energy homeostasis, which might trigger the onset of diabetes (Kinlaw et al., 1983). Due to its properties, fluorescent dyes responsive to zinc have been exploited to assess function in isolated islet cells (Zalewski et al., 1994).

Previous preclinical studies have shown that both radioactive ^{54}Mn and ^{65}Zn selectively accumulate at high concentrations in the pancreas (Fig. 1.4.10), the liver and the heart and in other endocrine organs, such as the thyroid, the adrenal cortex and the pituitary gland of the brain (Meschan et al., 1959, Lyden et al., 1983). The pharmacokinetics of those compounds showed a biphasic curve, with values decreasing within the first hours followed by a recover of uptake between 6 to 8 h and late retention until a few days after the administration of radioactive Mn.

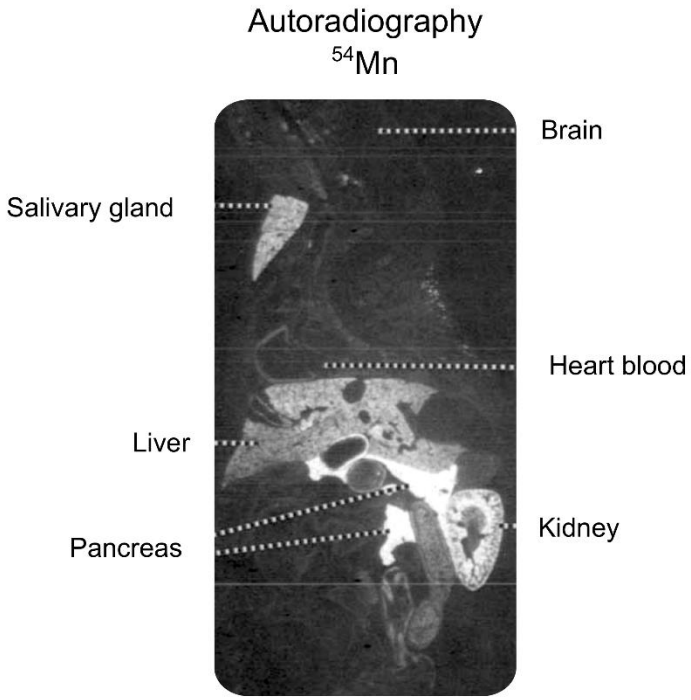

Fig. 1.4.10 Autoradiography of a mouse 24 h after $^{54}MnCl_2$ administration

The adapted figure (Meschan et al., 1959) shows the high accumulation of radioactive ^{54}Mn observed in specific region such as pancreas, liver, kidney and salivary gland.

A reduction in the accumulation of manganese has been previously shown in isolated pancreatic islets treated with different Ca^{2+}-blockers and pre-stimulated with high glucose concentrations (Gimi et al., 2006, Leoni et al., 2010). Since the opening of VDCC is promoted by the metabolism of glucose, which in turn is coupled with the secretion of insulin granules, ME-MRI measurements have been associated with β-cell function. Changes in the enhancement of signal and in the T_1 of the pancreas after $MnCl_2$ injection were observed *in vivo* in response to glucose stimulation and VDCC blockers (Lamprianou et al., 2011, Antkowiak et al., 2012, Antkowiak et al., 2013, Dhyani et al., 2013, Meyer et al., 2015) as well as in streptozotocin (STZ)-treated mice (Hernandez et al., 2017) and associated with the loss of islet mass. However, only little is known on the contribution of exocrine and endocrine pancreas, especially on the specificity of Mn uptake *in vivo* for the pancreatic islet cells. A major challenge consists in the discrimination of trace amounts of paramagnetic manganese between the exocrine and the endocrine pancreas (Leoni et al., 2011). In this regard, powerful analytical

technologies such as mass spectrometry imaging and x-ray fluorescence microscopy found new applications in the validation of MRI contrast agents. Recently, increased Mn accumulation in the sub-cellular compartments of stimulated β-cells has been demonstrated (Leoni et al., 2011).

Despite its potential neurotoxic effects, Mn^{2+} can be metabolized by the hepatocytes and excreted through the biliary system, therefore representing a valid alternative to other paramagnetic metals, such as Gd-based contrast agents (Napieczynska et al., 2017, Pan et al., 2011b). Mn^{2+}-dipyrodoxyl-diphosphate (MnDPDP), also known as Mangafodipir trisodium (TeslaScan®, Amersham Health), was the first manganese-based MR-contrast agent introduced in the clinical market for detection of lesions in the liver and the pancreas. The production of novel radioactive isotopes of manganese, such as ^{52}Mn and ^{51}Mn with short half-life holds the potential for clinical applications (Fonslet et al., 2017, Graves et al., 2017). In this regard, imaging of trace amounts of radioactive manganese with short half-life can potentially allow imaging of endocrine active cells while contemporary reducing the cellular toxicity induced in off-target tissues (Napieczynska et al., 2017).

2 Project Description

A non-invasive imaging method to monitor the loss of pancreatic β-cells represents a highly demanding tool to determine the progression of diabetic diseases. In this project, the main goal was to develop a multimodal and simultaneous PET/MRI protocol to provide measures of both BCM and function *in vivo*. As it is mentioned above, nowadays GLP-1R represents the most established and validated candidate for the measurements of BCM. On the other hand, only little is known on the specificity of Mn uptake for the endocrine pancreas. In this perspective, the validation and the optimization of accurate and quantitative ME-MRI measurements represented the main core of the research studies, which are here described.

To find the best trade-off between spatial resolution, time of acquisition and volume coverage, a VFA approach was considered an attractive solution for the measurements of Mn uptake in the pancreas. The main advantageous of this method relies on the rapid acquisition of large volumes. Indeed, high volume coverage was required due to the high heterogeneity of pancreas, in terms of anatomical localization and because of the heterogenous distribution of islets among the pancreatic lobes.

The first studies were carried out *in vitro* on phantoms and focused on the optimization of the number of FAs for the quantification of a large range of T_1 values. The purpose of the study was to determine the overall cost of increasing the number of FAs to improve the accuracy of T_1 maps. In this regard, different GRE protocols were assessed on Mn and Gd phantoms containing serial dilutions of the contrast agent. The following studies aimed to implement a simultaneous PET/MRI approach to measure both Mn and radiolabeled Ex4 in the pancreas.

The effect of Mn was measured by using VFA T_1 maps and a STIR image protocol, which was designed to suppress the signal of pancreas prior the

injection of the contrast agent. Further T_2 maps were acquired to determine their correlation with the T_1 maps.

Once the experimental workflow was established, differences between the pancreas of healthy and RIP1-Tag2 mice were assessed by PET and MRI measurements. Thus, group comparisons and analysis of the relationship between PET and MRI signal were performed. *In vivo* measurements were performed at high temporal and spatial resolution at early and late time points after the co-injection of radiolabeled Ex4 and $MnCl_2$. As it has been mentioned in the previous sections, in the past the validation of the specificity of Mn uptake was mainly limited by the poor resolution of non-invasive imaging techniques. To validate the specificity of Mn, *ex vivo* analysis, including laser-ablation inductively coupled plasma mass (LA-ICP-MS) imaging and autoradiography, were performed.

Since the internalization of Mn by isolated islet cells can be enhanced by glucose stimulation, *ex vivo* measurements were furtherly carried out on a separated group of mice that were not stimulated with glucose.

Further experiments were carried out to assess whether a single administration of contrast agent ($MnCl_2$) might affect the physiological insulin response to glucose. In this regard, the isolated islets were incubated at different glucose concentrations and the insulin content was assessed with a radioimmunoassay (RIA). Differences between the islets of healthy and RIP1-Tag2 mice were assessed at the respective time points, an early (1 h) or a late time point (24 h), after the administration of Mn-based contrast agent.

As part of the main project, further studies investigated the feasibility of a PET/MRI method to longitudinally monitor the engraftment of islet cells. This method has an expected impact on the development and the optimization of diabetes treatments, including the long-term administration of insulin in patients that are affected by T1D. The transplanted mouse model represents an attractive model for the validation of Mn uptake, especially due to the high signal-to-background of islet cells engrafted within the muscle of the calf of mice. As further

validation, the specificity of the PET tracer and Mn uptake was assessed in a group of mice treated with a specific inhibitor of VDCC.

Another promising approach to measure the functionality of the endocrine pancreas consists of the detection of radioactive isotopes of manganese with short half-life using nuclear imaging technologies (Graves et al., 2017, Hernandez et al., 2017). This approach relies on the detection of trace amount of metals, which might potentially lower the risk of high manganese exposure. PET imaging was performed to investigate on the pharmacokinetics of ^{52}Mn, which was systemically administered either as a free salt or radiolabeled with DPDP ligand. The tracer uptake was monitored until 72 h followed then by e*x vivo* biodistribution and autoradiography analysis of pancreas and brain sections aiming to validate the *in vivo* results.

Other experiments were carried out to investigate the properties of a quinoxaline-derivative binding to GLP-1R to enhance the specific uptake of radiolabeled Ex4. This method has promising applications in lowering the radioactive dose in off-target tissues. A blocking PET study was carried out on INS-1 xenograft mouse model to address the specificity of the PET tracer for the GLP-1R on the surface of INS1 tumors. Thus, different doses and injection times were examined to determine the effect of compound 2 (C2), a known quinoxaline-derivatives, through the quantification of PET scans acquired at early and late time points.

By using another approach, C2 was administered during the acquisition of dynamic PET scans by a continuous infusion of radioactive tracer. Furthermore, *in vivo* dynamic PET measurements aimed to monitor in real-time the effect of C2 on the receptors expressed from the engrafted and pancreatic islets.

3 Material and Methods

3.1 Establishment of *In vivo* PET/ME-MRI Protocols

This section describes the methods used in the *in vitro* and *in vivo* experiments, which focused on optimizing MR protocols and the characterization of the paramagnetic effect of Mn.

3.1.1 Phantom Preparation and MRI Assessment

1) A first phantom was prepared using 75 mm micro-hematocrit capillaries (Hirschmann Laborgeraete, Eberstadt, DE) with 1 mm of inner diameter filled with serial dilution of $MnCl_2$ tetrahydrate (0.10, 0.12, 0.15, 0.20, 0.25, 0.30, 0.35, 0.40, 0.50, 1.00 mM) in a solution with equimolar Bicine concentrations (Fig. 3.1.1a). The phantom was built on a 15 mL Falcon tube filled with tap water and directly measured on a 7T preclinical MRI scanner (ClinScan 70/30®, 290 mT/m, Bruker BioSpin MRI GmbH, Ettlingen, DE). The scanner was equipped with a volume RF-coil used as transmitter and receiver and 86 mm of inner diameter (Bruker BioSpin MRI GmbH).

   Reference values of T_1 were obtained by a series of inversion recovery sequence pulse (IRSE) pulse sequences which were acquired at increasing TI (TR/TE=10000/12ms, TI=50, 150, 300, 600, 1200, 2400, 5500, 9000 ms, slice thickness=1.5mm, NA=1, 128×128 matrix size, BW=25.6 kHz). The variable flip angle (VFA) T_1 maps were obtained through the acquisition of sequentially three-dimensional (3D) RF-spoiled GRE pulse sequences, whose flip angles were tuned to a series of expected T_1 values (TR/TE=10/1.5 ms, FoV=30×30×10 mm^3, slice thickness=0.5 mm, 128×128 matrix size, BW=86 kHz and NA= 2/20, $T_{1expected}$= 300, 500, 700, 100, 1200, 1500, 1800, 2500 ms; FAs=6°, 34°;

5°, 27°; 4°, 23°; 3°, 19°; 3°, 18°, 3°, 16°, 2°, 14°; 2°, 12°). The two ideal angles were calculated by using an algorithm already implemented in MapIt-Package (Syngo software, Siemens Healthineers).

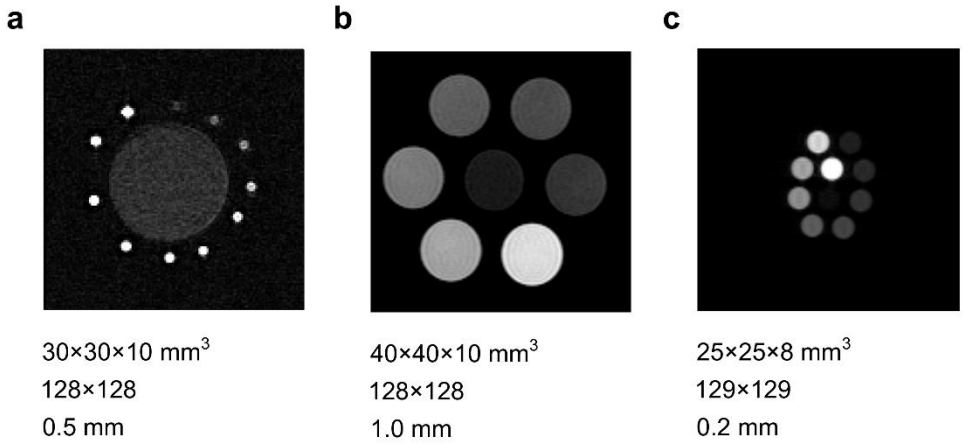

Fig. 3.1.1 Mn and Gd phantoms

In the figures are illustrated the representative axial 3D-GRE images (FA=27°) of the respective phantom experiments: (**a**) first (**b**) second and (**c**) third experiment.

2) Another Mn phantom was prepared using 2 mL self-standing cryogenic vials (Greiner Bio-One GmbH, Frickenhausen, DE), 1 cm of inner diameter. The vials were freshly prepared by filling them with increasing dilutions of $MnCl_2$:Bicine solution (0.05, 0.10, 0.15, 0.20, 0.30, 0.50) (Fig. 3.1.1b). The T_1 maps were calculated from the acquisition of an intra-gate and slab-selective (Sharpness=7) RF-spoiled 3D-GRE pulse sequences which were set to increasing FAs (TR/TE=10/1.5 ms, FoV=40×40×10 mm^3, slice thickness=1.0 mm, 128×128 matrix size, BW=89 kHz and NA=1, FAs=2°, 3°, 4°, 5°, 9°, 14°, 15°, 16°, 17°, 19°, 22°, 27°).
   MR images were acquired on an animal 7T BioSpec 70/30® scanner (Bruker BioSpin MRI GmbH, Ettlingen, DE), 300 mT/m of gradient strength, equipped with a mouse volume RF-coil and 40 mm of inner diameter (MT0205, Bruker BioSpin MRI GmbH, Ettlingen, DE).
3) A phantom containing NMR tubes with 5 mm of inner diameter was filled with a serial dilution of Gadovist® (Bayer Vital GmbH, Leverkusen, DE) solutions (0.08, 0.12, 0.18, 0.26, 0.40, 0.60, 0.89, 1.33, 2.00 mM). The phantom was examined on a 7T BioSpec 70/30® scanner (Bruker BioSpin

MRI GmbH, Ettlingen, DE) using a supporting Gradient Insert B-GA12S2 (MTBruker BioSpin MRI GmbH, Ettlingen, DE) and a mouse volume coil-40 mm of inner diameter (Fig. 3.1.1c) and 660 mT/m of gradient strength. MR images consist in a series of slab-selective (Sharpness=7) RF-spoiled 3D-GRE pulse sequences, which were acquired using different FAs and number of averages (TR/TE=10/1.3 ms, FoV=25×25×8 mm^3, slice thickness=0.2 mm, 129×129 matrix size, BW=75 kHz, FAs=2°, 3°, 4°, 5°, 9°, 14°, 15°, 16°, 17°, 19°, 22°, 27° and NA=2/6).

3.1.2 Radiolabeling of [^{64}Cu]NODAGA-^{40}Lys-Ex4

The production and the radiolabeling of radiolabeled Ex4 was performed by Gregory Bowden at the Department of Preclinical Imaging and Radiopharmancy (Tübingen, Germany) as follows. For the labeling of the exendin peptide, 100 MBq [^{64}Cu]$CuCl_2$ 0.01 M HCl was neutralized with ammonium acetate buffer pH=6, followed by the addition of 4 µg of NODAGA-^{40}Lys-Ex4 dissolved in 4 µL of deionized water and incubated at 42°C for 20 min. The labeling efficiency was determined by RadioTLC (Polygram Sil G/UV254) using citrate buffer (pH=5) as the mobile phase. The preparation of tracer solution was obtained by adding of 400 µL 0.1% Tween20 PBS buffer to the final reaction solution. High radioactive yield (230 GBq/µmol) and low dose peptide (1.3 nmol/kg) of PET tracer solution was prepared to avoid a systemic effect of the peptide.

3.1.3 Animal Preparation

All animals were kept under elevated hygiene conditions in isolated ventilated cages at approximately 22°C room temperature, 54% of relative humidity and 12 hours (h) light/dark cycle: food and water were provided ad libitum. The animals were previously fasted ~4 h before the measurements and, subsequently, transferred in a 17×17 cm^2 anesthesia induction box which was heated by a warming-pad. The mice were anesthetized with 1-2% isoflurane (CP Pharma, Burgdorf, DE) dissolved in 100% of O_2 by a Landmark Non-Rebreathing Veterinary System RTA-001 vaporizer. At the beginning of the imaging session, the anesthetized animals were transferred to a working place and allowed to breath the anesthesia mixture induced by a cone on the end of a tube connected

to the vaporizer. A single home-made tail vein catheter with an inner diameter of 0.28 mm connected to the end of a U40 insulin syringe filled with heparin in a 0.9% NaCl solution was placed in the lateral vein.

Subsequently, the unconscious mice were transferred on a dedicated MR-compatible mouse bed equipped with a water-based warming-pad. A continuous flow of anesthesia set to 1-2% isolflurane/O_2 was maintained over the entire acquisition time.

3.1.4 Experimental Workflow

3.1.4.1 Evaluation of Different MR Protocols to Assess Mn Uptake from the Abdominal Organs

A pilot study using 9-week-old control and RIP-Tag2 mice (n=1/1) with C3H/FeJ background was conducted. A STIR protocol was designed based on the quantification of T_1 of the pancreas tissue using an IRSE method.

The STIR images and VFA T_1 maps were simultaneously acquired with the recording of dynamic or static PET scans at different time points, before, at 1 h and 24 h after the injection of the radioactive tracer (Fig. 3.1.2). The administration of contrast agent solution and the PET tracer was performed through sequential i.v. bolus injections: 50 µL of [^{64}Cu]Ex4 solution (~0.12 MBq/g), 34 mM $MnCl_2$:Bicine solution (~75 µmol/kg) and glucose solution (1.5 g/kg) were injected and flushed via a single tail vein catheter. The content inside the catheter was flushed with another volume of 0.9% NaCl solution five minutes after the contrast agent injection. The acquisition of dynamic PET scans (0-1 h) started after the i.v. injection of radioactive tracer.

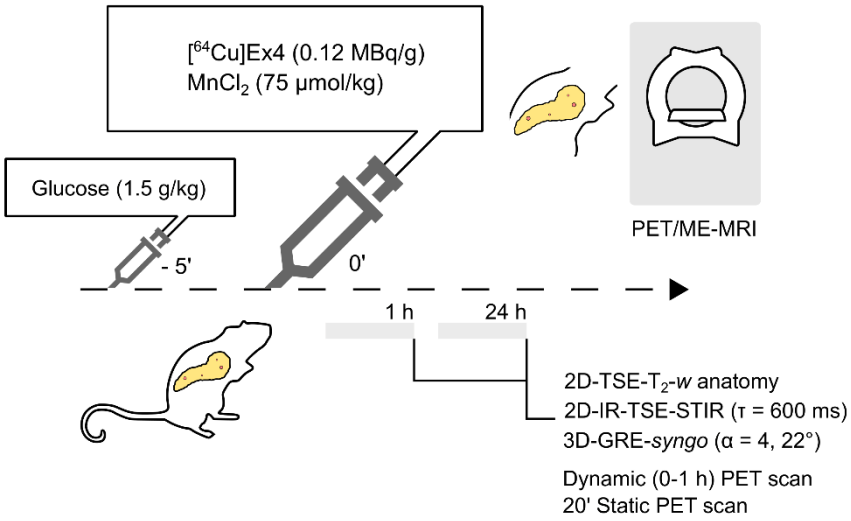

Fig. 3.1.2 Simultaneous PET/MR imaging workflow

Dynamic PET imaging was performed simultaneously with the acquisition of MR images between 0-1 h after the co-injection of radioactive Ex4 (~0.12 MBq/g) and Mn-based contrast agent (75 µmol/kg). A stimulatory i.v. injection with glucose at high dose (1.5 g/kg) was performed five minutes before the injection of the MR contrast agent through the catheter. Follow-up with simultaneous PET/MRI measurements is performed at 24 h post injection to monitor the retention of the PET tracer and the MR contrast agent.

A second group of 7-week-old control RIP1-Tag2 mice (n=8) was measured using a slightly different PET/MRI protocol. The mice were treated with an intraperitoneal injection of $MnCl_2$:Bicine solution (75 µmol/kg) and glucose (1.5 g/kg) one day before they received an intravenous bolus injection of the PET tracer solution (Fig. 3.1.3). *In vivo* measurements included the acquisition of T_2 maps, VFA T_1 maps and STIR images simultaneously with the acquisition of 20-min static PET scans 24 h and 48 h post injection.

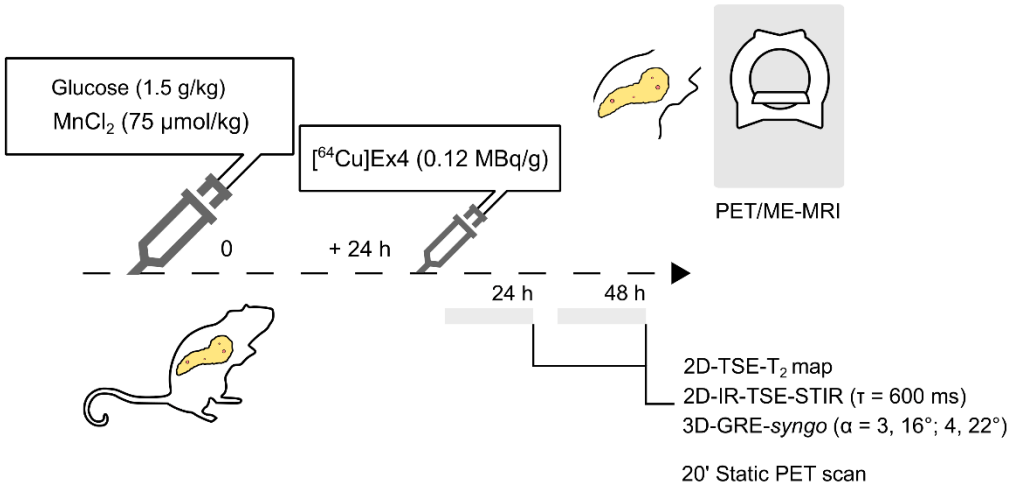

Fig. 3.1.3 PET and multiparametric MRI workflow with delayed Mn uptake

A group of 7-week-old RIP1-Tag2 mice was intraperitoneally injected with an analogue dose of $MnCl_2$:Bicine solution 24 h before the *in vivo* measurement. Static measurements with a simultaneous PET/MR imaging setup were performed at 1 h and 24 h after the injection of [^{64}Cu]Ex4 (~0.12 MBq/g).

3.1.5 MRI Acquisition

MR images were acquired on a preclinical scanner (Bruker BioSpin MRI GmbH, Ettlingen, DE). The scanner was equipped with a transmitter/receiver rat volume RF-coil with 86 mm of inner diameter (Bruker BioSpin MRI GmbH, Ettlingen, DE). Tuning and matching of the coil were performed after positioning of the animal inside the bore of the scanner.

3.1.5.1 TSE Whole Body Anatomical Images

After the acquisition of a rapid localizer pulse sequence, a TSE image was acquired with an isotropic resolution of 0.25 mm. Subsequently, a multi-slice TSE image (TR/TE=800/47 ms, FoV=30×30 mm^2, matrix size 128×128, NA=32, BW=102 kHz, RARE factor=16, in plane resolution of 0.23 mm and slice thickness 1.5 mm) aimed to center the pancreas.

3.1.5.2 T_1 Relaxometry of Pancreas

To quantify the T_1 of the pancreas, sequential TSE images set to different TI (TR/TE=5500/7.8 ms, FoV=30×30x1.5 mm^3, TI=50, 200, 400, 800, 1200, 1600, 2200, 3500, 5300 ms, NA=4, BW=100 kHz, matrix size 128×128, RARE

factor=16, slice thickness 1.5 mm) were acquired and centered to the abdominal region of the mice.

3.1.5.3 T_2 Maps

An axial two-dimensional T_2 map was measured through the acquisition of TSE pulse sequences TR=2000 ms, TE=141, 131, 121, 111, 101, 91, 81, 71, 61, 51, 40, 30, 20, 10 ms, FoV=30×30 mm^2, matrix size 128×128, BW=102 kHz, NA=1 and slice thickness 1.5 mm.

3.1.5.4 TSE Short Tau Inversion Recovery (STIR)

A two-dimensional TSE (TR/TE=5500/7.8 ms, FoV=30×30x1.5 mm^3, TI_{null}=600 ms, NA=4, BW=100 kHz, matrix size 128×128, RARE factor=16, slice thickness 1.5 mm) was acquired with a TI_{null} calculated using the equation below:

$$TI_{null} = T_{1\,pancreas} \cdot \ln 2 \qquad \text{eq. 13,}$$

where the $T_{1\,pancreas}$ is the longitudinal relaxation time of the pancreas prior the injection of the contrast agent.

3.1.5.5 VFA T_1 Maps

The VFA T_1 maps were obtained from the acquisition of sequential RF-spoiled 3D-GRE pulse sequences, which were set to different $T_{1expected}$=700, 1500 ms (TR/TE=10/1.5 ms, FoV=30×30×10 mm^3, matrix size 128×128, FAs=4°, 23°, NA=3, BW=85 kHz, slice thickness 1.5 mm).

3.1.6 PET Acquisition

Following anesthesia of mice, the animals were placed on the animal imaging bed, which in turn was delivered inside the center of the FoV of MRI. Dynamic and static PET scans were acquired on an MR-compatible and removable PET-insert (Department of Preclinical Imaging and Radiopharmancy, UKT in collaboration with Bruker BioSpin MRI GmbH, Ettlingen, DE) placed inside the MRI bore (Judenhofer et al., 2008) True coincidence events with an energy window set to 350-650 keV and a timing window of 2.81 ns were saved as list-mode file.

Dynamic (0-1 h) PET scans were set to measure ^{64}Cu over 3600 seconds. The PET imaging protocols started few seconds before a bolus i.v. injection of the radioactive tracer.

Static images of 20 min were acquired after 40-60 min of unconscious uptake time and at late time points (24 h) after the injection of the PET tracer.

3.1.7 Image Analysis

3.1.7.1 IRSE T_1 Quantification

The regions of interest (ROIs) were manually drawn on π.pmod (PMOD Technologies LLC, Zürich, CH) using as anatomical reference a TSE image at long TI. The ROIs were subsequently imported to the other images to measure the mean values of S.I. at different TI. The mean values were exported into a text file and used to calculate the T_1 values by fitting the data using the following equation:

$$M_z(t) = M_0 \cdot (1 - 2e^{-TI/T_1}) \qquad \text{eq. 14.}$$

3.1.7.2 T_1 Relaxometry

A linear regression analysis was performed to calculate the r_1 related to the paramagnetic effects of $MnCl_2$:Bicine and Gadovist on the longitudinal relaxation time. The slope of the linear equation explains the relationship between the R_1 and the respective concentrations of the Mn and Gd-based contrast agents.

3.1.7.3 Combinatorial Analysis of T_1

The regions of interest (ROIs) for each vial were manually defined on π.pmod (PMOD Technologies LLC). Subsequently, the ROIs were saved and imported on the GRE images acquired at different FAs to calculate the mean values and the standard deviation (SD) of the S.I. calculated from each phantom vial (Fig. 3.1.4a).

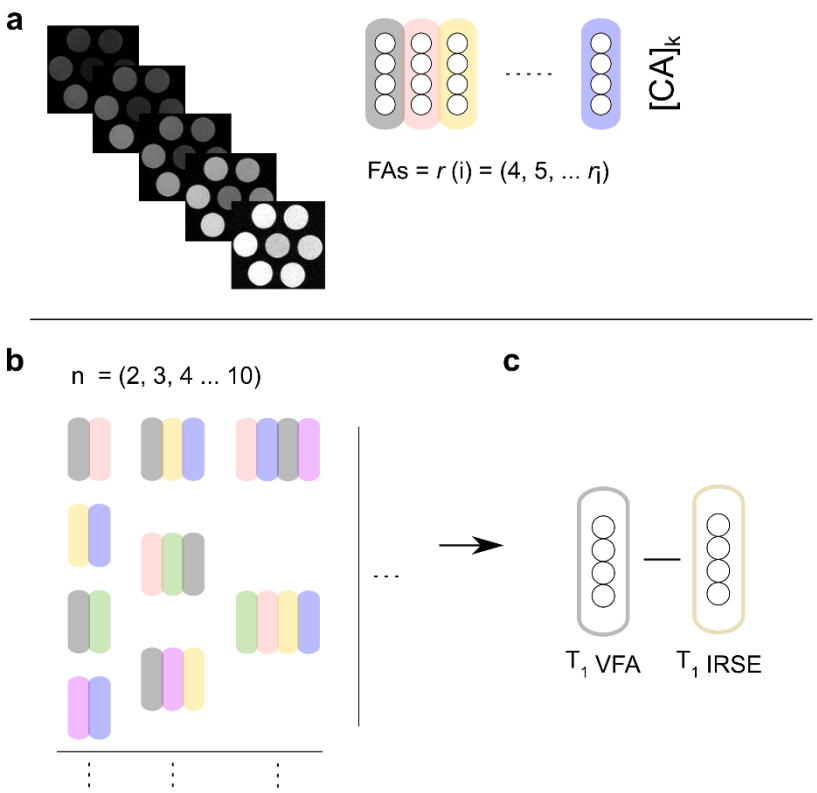

Fig. 3.1.4 Analysis of VFA T_1 by a combinatorial approach

(**a**) The ROI were manually drawn and subsequently imported on 3D-GRE images acquired at different FAs and color labeled in the figure. (**b**) The combinations of FAs were generated using increasing number of FAs (n=2, 3, 4, 6 and 10) following the calculation of VFA T_1 values. (**c**) The accuracy of different combinations of FAs was subsequently assessed by using the percentage of error (%) estimated between the VFA T_1 and the reference IRSE T_1 values.

The mean values were subsequently imported to MATLAB. All the possible combinations of flip angles were generated using the following equation:

$$C(n,r) = \frac{n!}{(n-r)!\,r!} \qquad \text{eq. 15,}$$

where *n* is the total number of flip angles and *r* is the number of angles used for the calculation of T_1 (*r*=2, 3, 4, 6, 10). The VFA T_1 values of each vial and combination were obtained through fitting of the mean values of S.I. accordingly to eq. 12. The accuracy in the quantification of T_1 values was estimated by calculating the percentage of error between the VFA T_1 and the IRSE T_1 values (Fig. 3.1.4b, c). For a given set of combination, only the 10^{th} percentile of the percentages of error were considered.

3.1.7.4 STIR Quantification

For the analysis of STIR images, the mean values ± SD of the S.I. were calculated from the images acquired before and after the injection of the contrast agent. Thereafter, the percentages of the signal enhancement (%S.E.) were calculated through the following equation:

$$\%S.E. = \frac{\left(S.I._{.post} - S.I._{.pre}\right)}{S.I._{.pre}} * 100 \qquad \text{eq. 16,}$$

After the VOIs were imported on the two-dimensional STIR images, the not a number (NaN) voxels lying outside the regions, as well as those with values equal to 0 or <0 were excluded from the analysis. Subsequently, the median values were calculated from the voxels of each VOI, followed by the calculation of the mean values ± SD of the VOIs for all the animals.

Due to the spatial mismatch between the images acquired before and 24 h after the contrast agent injection, the %S.E. was calculated using the median values of the VOIs acquired before and 24 h after the injection of the contrast agent.

3.1.7.5 VFA T_1 Quantification

The mean values ± SD of T_1 of VOIs were calculated from the T_1 maps. The maps of T_1 were automatically reconstructed on Syngo using two flip angles and optimized for a given T_1 value. For the calculation of T_1 maps using multiple flip angles, the mean values ± SD of T_1 was calculated from the information of VOIs. The values of S.I. of voxels and their spatial information were exported as text files and, subsequently, imported on MATLAB. Thus, the mean values ± SD of T_1 values were calculated at different flip angles based on eq. 12. Voxels with values below 100 ms and above 2500 ms were excluded, following the conversion of T_1 into R_1 values. The calculation of [Mn] was performed voxel-wise according to the following equation

$$[Mn] = \frac{\left(R_{1\,post} - R_{1\,pre}\right)}{r_{1\,MnCl2:Bicine}} \qquad \text{eq. 17,}$$

where r_1 is the relaxivity of $MnCl_2$:Bicine obtained from the studies *in vitro* described previously. The medians of VOIs were calculated, excluding the voxels containing values equal to 0, NaN or <0. The estimated values of [Mn] for the images acquired at 24 h were calculated by subtracting the mean values of the VOIs to those which were calculated before the injection of contrast agent. Therefore, the mean values ± SD were calculated for each VOI and among all the animals.

3.1.7.6 PET Quantification

The voxels of VOIs containing values of radioactive units (kBq/mL) were exported and imported on MATLAB. To calculate the percentage of injected dose (%ID/mL), the values were normalized for the injected activity (IA) and the decay of ^{64}Cu ($T_{1/2}$=12.7 h) between the time between the injection and the image acquisition. The medians of each VOIs were obtained following the calculation of the mean values ± SD among the group of mice.

3.1.7.7 PET Scan Reconstruction

The dynamic and static PET data were normalized using a cylinder-source component method and reconstructed by using an in-house OSEM2D algorithm, matrix size 256×256×89, subsets=16, iteration=4 and voxel size 0.326×0.326×0.796 mm^3. Data were decay corrected ($T_{1/2}$=12.7 h) and normalized using the branching factor for ^{64}Cu (branching ratio=0.174).

3.1.7.8 PET/MRI Co-registration and ROIs Definition

The PET images were overlaid with the MR images on Inveon Research Workplace (Siemens Preclinical Solutions). The anatomical landmarks of the kidneys of the animals were used as reference for the manual co-registration of the images. The volumes of interest (VOIs) of the pancreas, spleen and renal cortex were revealed by using the anatomical information from 3D-GRE images. The mean values, the voxel values and the spatial information of VOIs were saved and imported to the respective two-dimensional STIR images and T_2 maps. Subsequently, data were exported as a text file and imported into MATLAB (Mathworks, Natick, MA, USA) for further analysis.

3.1.8 Statistical Analysis

The mean ± SD as well as the median of each VOI were calculated using the built-in functions implemented in Statistics and Machine Learning Toolbox on MATLAB (Mathworks, Natick, MA, USA).

3.1.8.1 PET/MRI Correlation Analysis

The Pearson's correlation coefficients (*r*) were produced on MATLAB (Mathworks, Natick, MA, USA) using the median values calculated from the quantification of co-registered PET/MR images. The correlation analysis was performed between the R_1, signal intensity (STIR) and %ID/mL measured from the spleen, kidneys and pancreata at 1 h after the co-injection of the PET tracer and contrast agent.

The correlation coefficients between the R_1, R_2 and signal intensity (STIR) were computed from the PET/MR images acquired 24 h after the injection of the contrast agent.

3.2 Simultaneous PET/MRI Measures BCM and Function

The following studies were conducted after optimizing the MR and PET protocols described in the previous section. This section focusses on the assessment of the specific uptake of Mn and [^{64}Cu]Ex4 in the pancreas of control and RIP1-Tag2 mice.

3.2.1 RIP1-Tag2 Mouse Model

The breeding and the selection of mice carrying the positive expression of large T antigen (Tag2) under the control of Rat Insulin promotor 1 (RIP1) were carried out by Barbara Schoerg at the Department of Preclinical Imaging and Radiopharmancy (Tübingen, Germany). The RIP1-Tag2 mice develop β-cell derived insulinomas at high reproducibility starting from hyperplasia at 5 weeks of age until the formation of solid tumors occurring at week 14 with symptomatic blood glucose levels (Bergers et al., 1999). The measurements of blood glucose levels were performed on cohorts on in-house bred transgenic RIP1-Tag2 mice and age-matched littermate control mice with a C3H/FeJ background. Evaluation of hypoglycemia in mice was monitored over the period of rapid progression of pancreatic insulinomas, occurring typically between 8 and 13 weeks of age (Bergers et al., 1999).

3.2.2 Radiolabeling of [^{64}Cu]Ex4

The production and the synthesis of radioactive [^{64}Cu]Ex4 was carried out in agreement with the study previously described (see 3.1.2).

3.2.3 Animal Preparation

Prior to the *in vivo* measurements, the induction of anesthesia was performed as described in the previous subsections (see 3.1.3). To stimulate the metabolic uptake of Mn by the pancreatic islets, all mice then received an i.v. injection of glucose solution (1.5 g/kg) 5 min after the administration of $MnCl_2$ (Fig. 3.2.1a).

3.2.4 Experimental Workflow

3.2.4.1 Evaluation of Mn and Radiolabeled Ex4 at Early Time Points by Simultaneous PET/MRI and Ex vivo Analysis

- *Group 1*

Groups of 13-week-old control and transgenic RIP1-Tag2 mice (n=3/3) with established insulinomas were measured on a 7T ClinScan 70/30® (Bruker BioSpin MRI GmbH, Ettlingen, DE) using a mouse volume RF-coil with 40 mm of diameter. An MR-compatible and removable PET-insert detector was installed inside the bore to enable the simultaneous acquisition of multimodal images.

The setting included the acquisition of dynamic 0-1 h PET and VFA T_1 maps, which were previously centered in the abdominal region of mice, 1 h after the injection of the PET tracer and T_1-positive contrast agent (Fig. 3.2.1a). After the last imaging session, the isolation of tissues was followed by *ex vivo* autoradiography of the pancreas cryosections. Subsequently, the pancreas sections were measured with LA-ICP-MS imaging protocol (Fig. 3.2.1b).

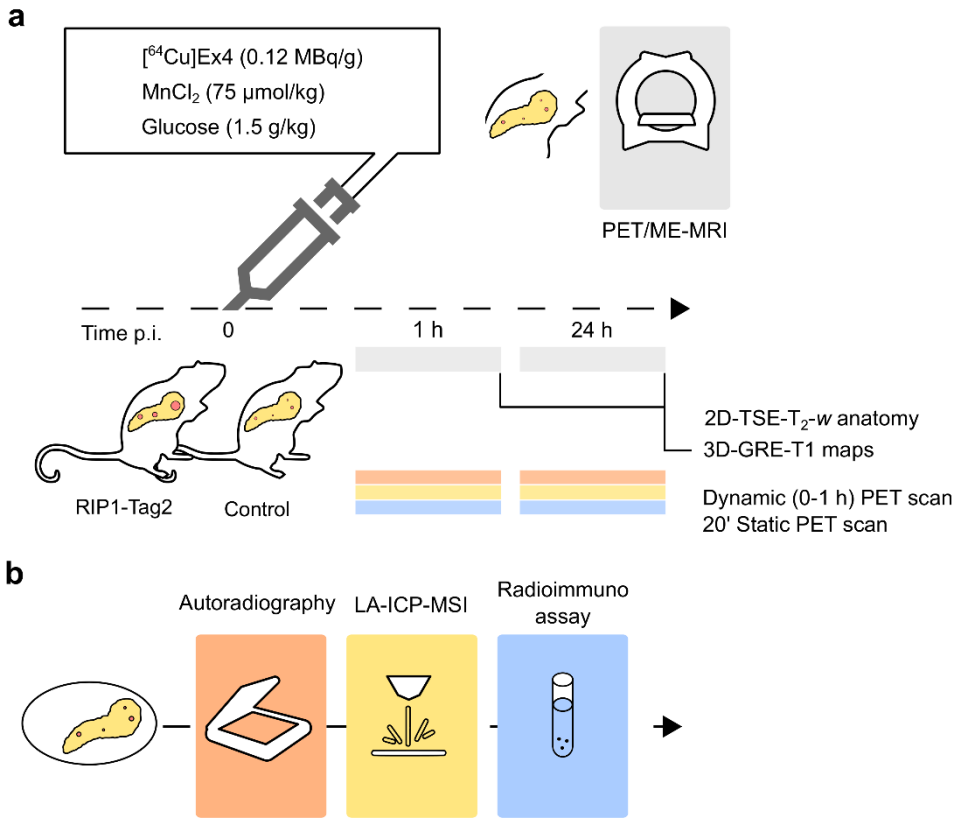

Fig. 3.2.1 Experimental *in vivo* imaging workflow and *ex vivo* validation studies

(**a**) *In vivo* PET/MRI aimed to simultaneously quantify BCM and function: the PET/MR images were acquired simultaneously or consecutively 1 h and 24 h after the co-injection of radioactive Ex4 and Mn-based contrast agent. (**b**) *Ex vivo* analysis of pancreas, and analysis of the insulin secretion response was evaluated at the respective time points. The figures were modified and adapted from the research article (Michelotti et al., 2020).

3.2.4.2 Assessment of Mn and Radiolabeled Ex4 Uptake at Late Time Points

- *Group 2*

Another group of control and RIP1-Tag2 mice (n=4/4) was measured on a small animal 7T BioSpec 70/30® scanner (Bruker BioSpin MRI GmbH, Ettlingen, DE), which was equipped with a RF-coil with an inner diameter of 40 mm. MRI measurements were followed by the acquisition of PET scans on a stand-alone small animal PET scanner (dedicated Inveon PET, Siemens Healthineers, Knoxville, TN, USA). Images were longitudinally acquired at 10 and 13 weeks of age to monitor the progression of pancreatic insulinomas. The *in vivo* measurements consisted of 20-min static PET scans and VFA T_1 maps, which were acquired at 24 h after the sequential bolus injections of the PET tracer and

MRI contrast agent. After the last imaging time point, *ex vivo* analysis, including autoradiography followed by LA-ICP-MS imaging of the pancreas cryosections, were carried out to determine the late distribution of imaging probes throughout the entire sections.

3.2.4.3 Follow-up of Mn and Radiolabeled Ex4 at both Early and Late Time Points by Combined PET/MRI

- *Group 3*

Further image acquisitions at early (n=3/8) and late time points (n=6/13) were provided through the measurements of separated cohorts of control and RIP1-Tag2 mice (n=4/9) with age ranging between 10 and 15 weeks. The 20-min static PET scans were acquired on a stand-alone PET scanner followed by the acquisition of the anatomical images and T_1 maps on a 7T BioSpec 70/30® scanner (Bruker BioSpin MRI GmbH, Ettlingen, DE). Monitoring of blood glucose levels was performed between 9 and 13 weeks of age in control and aged-matched RIP1-Tag2 mice (n=4/4) to determine the severity of hypoglycemia.

3.2.4.4 Determining the Effect of Glucose Stimulation on the Retention of Mn and Radiolabeled Ex4

- *Group 4*

Further *ex vivo* experiments were performed on additional groups of control and RIP1-Tag2 mice. A group of mice was examined with *ex vivo* autoradiography and LA-ICP-MS imaging at 1 h (n=3/3) and 24 h (n=2/1) after the co-injection of the PET tracer and contrast agent. In accordance with the previous study, mice were treated with sequential bolus injections of the PET tracer and contrast agent, however without further stimulation with glucose solution.

3.2.4.5 Evaluation of Insulin Secretion Capacity by In Vitro Assessment of Insulin Secretion in Response to Glucose

- *Group 4*

The secretion of insulin from isolated islets of 8-week-old control and RIP1-Tag2 mice was assessed *in vitro* at different time points, 1 h (n=3/3) and 24 h (n=3/3),

respectively, after the systemic administration of $MnCl_2$:Bicine solution (75 µmol/kg).

Analysis of islet function was carried on another group of control and aged-matched 13-week-old RIP1-Tag2 mice (n=3/3) with advanced tumor progression.

3.2.5 MRI Acquisition

3.2.5.1 TSE Whole Body Anatomical Images

The localization of the pancreatic region within the abdominal region of mice was performed as described in the previous studies (see 3.1.5.1).

3.2.5.2 VFA T_1 Maps

- *Group 1*

The VFA T_1 maps were obtained by acquiring two sequential 3D-GRE images acquired at different flip angles (TR/TE=10/1.9 ms, FoV=34×34×17 mm^3, matrix size 128×128, NA=2, BW=75 kHz, FAs=4°, 22°, slice thickness 0.5 mm). Reconstruction of maps were performed using an in-house algorithm and developed on MATLAB. Measurements were carried on a 7T ClinScan 70/30® scanner (Bruker BioSpin MRI GmbH, Ettlingen, DE) equipped with a mouse volume RF-coil, 40 mm of inner diameter (MT0205, Bruker).

- *Group 2*

Another VFA T_1 mapping protocol running on a 7T BioSpec 70/30® scanner (Bruker BioSpin MRI GmbH, Ettlingen, DE) was implemented to longitudinally monitor the progression of pancreatic insulinomas. Maps of T_1 were generated from the signal intensity of RF-spoiled 3D-GRE images, which were set to different flip angles (TR/TE=10/1.9 ms, FoV=34×34×17 mm^3, matrix size 128×128, NA=2, BW=75 kHz, FAs=4°, 22°, isotropic resolution 0.3 mm).

- *Group 3*

A third protocol running on a 7T BioSpec 70/30® scanner (Bruker BioSpin MRI GmbH, Ettlingen, DE) relied on the acquisition of three 3D-GRE images set to

different flip angles (TR/TE=10/1.9 ms, FoV=34×34×17 mm^3, matrix size 128×128, NA=2, BW=75 kHz, FAs=4°, 14°,27°, isotropic resolution 0.3 mm).

3.2.6 PET Acquisition

- *Group 1*

The dynamic (0-1 h) PET scans acquired on the PET-insert detector (Tuebingen PET/MR in collaboration with Bruker BioSpin MRI GmbH, Ettlingen, DE) were set as described in the previous section (see 3.1.6). Static PET image of 20 min were acquired between 40-60 min after the tracer injection.

- *Group 2-3*

Following the induction of anesthesia, mice were placed on transferable animal imaging bed docked on a carbon-fiber holder of the scanner, positioned by using the alignment laser function to center the abdominal region and remotely shuttled in the center of the FoV through the Motion Control panel on Inveon Acquisition Workplace (Siemens Preclinical Solutions). The acquisition of PET on Inveon dedicated PET scanner (Siemens Healthineers, Knoxville, TN, USA) was performed consecutively to the acquisition of MR images. The PET scanner was set to record true coincidence events with energy in the range between 350 and 650 keV and 3.43 ns of time resolution. The acquisitions of 20-min static PET scans were performed at early (1 h) and late points (24 h) after the injection of the PET tracer.

3.2.7 Cryotome and Autoradiography

Following the last imaging session, mice were kept under deep anesthesia and were sacrificed through cervical dislocation and the intact pancreas was excised, placed under -20°C and embedded in optimum cutting temperature gel (Sakura, Zoeterwonde, NL) and frozen. Subsequently, serial cryosections with 20 µm of thickness were obtained from the entire pancreas with a Cryostat (Leica 1850, Leica Microsysistems, Wetzlar, DE) and subsequently exposed to a 35×43 cm phosphor imaging plate (445SI, Molecular Dynamics, Sunnyvale, CA, USA). After being exposed for 24 h at room temperature, the plates were scanned on a Storm 840 scanner (Amersham Biosciences, Amersham, UK) with a spatial resolution

of 50 µm. The autoradiography slides were then analyzed using ImageJ software (US NIH, Bethesda, Maryland, USA).

3.2.8 LA-ICP-MS Imaging

The acquisition of mass spectrum data was performed by Astrid Zimmerman at the Research Center Juelich. The cryosections were scanned using an NWR 213 laser ablation system (New Wave Research, Fremont, CA, USA) at high spatial resolution (60 µm of spot size). The ablated tissue was vacuumed via argon gas flow and transported to an Agilent 7900 ICP-MS (Agilent Technologies, JP) for continuous data acquisition regarding the isotopes ^{44}Ca, ^{65}Cu, ^{64}Zn, ^{55}Mn and ^{13}C. Image reconstruction was performed using an in-house software package IMAGENA (Osterholt et al., 2011).

3.2.9 Insulin Secretion Assay

The isolation of pancreatic islets and the insulin secretion assays were carried out by Dr. Jonas Maczewsky at the Pharmaceutical Institute of the University of Tuebingen. The mice were anesthetized with 1-2% isoflurane/O_2 gas mixture (Vetland, Louisville, KY, USA), injected with a $MnCl_2$:Bicine (75 µmol/kg) solution and allowed one hour of unconscious uptake. Subsequently, the animals were sacrificed by cervical dislocation and the pancreas was exposed to inject 3-5 mL of a 1 mg/mL Collagenese P, *Clostridium histolyticum*, 1.8 U/mg lyo. (Roche Diagnostics, Indianapolis, IN, USA) in a Krebs-Ringer (KRH)-4-(2-hydroxyethyl)-1-piperazineethanesulfonic acid (HEPES) solution, 120 mM NaCl, 4.7 mM KCl, 1.1mM $MgCl_2$, 2.5 $CaCl_2$, 10 mM HEPES, via the duodenal duct. The intact pancreata were collected in 15 mL Falcon tubes, incubated at 37° C for 6-8 min in a TW20 water bath (Julabo GmbH, Seelbach, DE). The blocking of the enzymatic reaction was achieved by filling up the tubes until 12 mL of volume with 0.5% bovine serum albumin (BSA) Krebs-Ringer Bicarbonate (KRB) buffer solution. After centrifugation for 1 min at 1000 revolutions per minute (RPM), the pellet was re-suspended twice in 12 mL of blocking solution. A part of the volume was transferred into a black colored petri dish to facilitate the hand-picking of the islets under the optical lens of a microscope.

The insulin secretion assay started with the incubation of triplicates of batches of five islets (n=5) prepared for each glucose condition (3, 6, 8, 10, 15 and 30 mM) in 0.5% BSA, KRB solution at basal glucose concentration (3 mM) at room temperature. Therefore, the islets were transferred in polystyrene cylindrical tubes and incubated for 1 h at 37° C. The content of insulin in the supernatant was collected and stored at -80° C and subsequently determined by radioimmunoassay using standards Millipore 8013-K (Merck, Darmstadt, DE). The percentage enhancement between basal (3 mM) and stimulated condition (15 mM) was calculated to determine the physiological insulin response to glucose.

3.2.10 Image Analysis

3.2.10.1 PET Scan Reconstruction

Static PET data saved as list-mode files on Inveon Acquisition Workplace (Siemens Heathineers) were subsequently normalized by a cylinder-source component method. Image reconstruction was performed by a 3D ordered-subsets-expectation-maximization algorithm (OSEM3D-fastMAP) with the following parameters: MAP-subsets=16, MAP-iteration=18, OSEM3D-iteration=2, 256×256×159 of matrix size and voxel size 0.388×0.388×0.796 mm^3.

The datasets obtained from the PET-insert scanner were reconstructed by using an in-house script and keeping the general acquisition parameters set as described in the previous section (see 3.1.7.7).

3.2.10.2 PET/MRI Co-registration and VOIs Definition

The PET and MR images were loaded and overlaid on Inveon Research Workplace (Siemens Heathineers) using the kidney as anatomical landmarks or the manual co-registration of the images. In addition to the VOIs drawn on the entire pancreas, further VOIs were manually drawn to measure the pancreatic insulinomas of RIP1-Tag2 mice.

3.2.10.3 VFA T_1 Quantification

The VFA T_1 maps were reconstructed voxel-wise by using an in-house script, which was kindly provided by Dr. Jonathan Disselhorst and implemented on MATLAB. Once the voxels and the spatial information of the VOIs were save as text files, data were quantified on MATLAB using the methods described in the previous section (see 3.1.7.5).

3.2.10.4 PET Quantification

The quantification and the normalization of the voxels of VOIs saved from the static and dynamic PET scans were performed exactly as previously described (see 3.1.7.6).

3.2.10.5 Phosphor Image Analysis

The quantification of the signal of autoradiography was performed on ImageJ software (US NIH, Bethesda, Maryland, USA). The mean values ± SD of the signal intensity as well as the diameter of the spot dimensions were measured. The signal was subsequently normalized for the background and the tissue areas of the same section.

3.2.10.6 Post-processing of LA-ICP-MS Data

The continuous LA-ICP-MS data were saved as text file and subsequently imported to MATLAB for the reconstruction of 2D-images. Subsequently, the elemental 8-bit images of ^{44}Ca (red channel), ^{64}Zn (green channel) and ^{55}Mn (blue channel) levels were merged by additive color model (values of 0-255).

3.2.11 Statistical Analysis

The mean ± SD and the Pearson' *r* coefficients were calculated on MATLAB (Mathworks, Natick, MA, USA) using the built-in functions implemented on Statistics and Machine Learning Toolbox.

3.2.11.1 Group Comparison

Differences in the $\log_{10}$(%ID/mL) and $\log_{10}(R_1)$ were calculated between the Pancreas^{Control} and Pancreas$^{RIP1\text{-}Tag2}$ on JMP Software (13.0.0, SAS Institute Inc.) by using a two-sample Student's *t*-test assuming unequal variance and Alpha level 0.05. For the comparison of blood glucose levels, significance between the groups of mice was calculated using a nonparametric Rank Sum Wilcoxon's test.

3.2.11.2 PET/MRI Correlation Analysis

The co-variance between the PET and MRI measurements was computed by calculating the Pearson's *r* coefficients of the mean values of $\log_{10}$(%ID/mL) and $\log_{10}(R_1)$ from the VOIs of both control and RIP1-Tag2 mice, Pancreas^{Control} and Pancreas$^{RIP1\text{-}Tag2}$, respectively. A voxel-wise correlation analysis between multimodal images was computed using the values of the voxels of each individual VOI.

3.3 Monitor of Islet Cell Engraftment by PET/MRI

The following sections describe the methods and the experimental setting used to monitor the engraftment of islet cells in a transplanted mouse model.

3.3.1 Transplanted Mouse Model

For each separated study, littermate 6 to 7-week-old C3H mice were ordered (Charles River, Sulzfeld, DE), divided in the respective donor and recipient cohorts (n=30/10) and allowed to acclimatize before the surgery for one week. Dr. Weal Eter (Radbound University Nijmegen) carried out the experiments for the isolation and transplantation of islets.

Before the surgery, a series of 50 mL Falcon tubes filled with Roswel Park Memorial Institute (RPMI) 1640 medium and 0.9 mg/mL collagenase-V solution (Sigma Aldrich, St Louis, MO, USA) were prepared and kept in ice. After sacrification of mice by cervical dislocation, a volume of 2-3 mL of collagenase solution was injected through the bile duct. Subsequently, the pancreata were isolated and transferred into the 50 mL Falcon tubes, with a maximum of five pancreata per tube. After the incubation of Falcon tubes at 37°C in a TW20 water bath (Julabo GmbH, Seelbach, DE) for ~10-12 min, the digestion of pancreata was blocked by filling the volume of tubes with a cold RPMI 1640 medium (10% FCS, 100 penicillin units/mL, streptomycin 100 µL/mL). After centrifugation, the pellet was collected from the Falcon tubes, washed twice with fresh medium and filtered with a 500 µm mesh. The resulting content was transferred into another 50 mL Falcon tubes filled with fresh medium. After centrifugation, the remaining pellet was separated by gently adding 15 mL of each Ficoll solution (Cellgro by Mediatech Inc., Manassas, VA, USA) in the order 1.118, 1.096 and 1.037 g/mL and centrifuged at 1900 RPM for 16 min without brake. Therefore, the separated islets were hand-picked between the first and the second Ficoll layer with a micropipette and transferred to a 15 mL Falcon tube. After centrifugation at 600 RPM for 2 min, the islets were re-suspended at 1 islets/1 µL and counted in a 96-well plate by taking a volume of 40 µL mixed with 40 µL of trypan blue.

For the inoculation of islets into the calf of mice, ~600 islets per mouse were hand-picked and counted in a petri-dish under a bright field microscope. A volume

of ~30 µL was inoculated into the calf of recipient mice by using a 1 mL Hamilton syringe and needles with a 0.8 mm diameter.

3.3.2 Radiolabeling of [^{64}Cu]Ex4

The production and the synthesis of radioactive [^{64}Cu]Ex4 was performed in agreement with the methods previously described (see 3.1.2).

3.3.3 Animal Preparation

For the preparation of *in vivo* measurements, the induction of anesthesia as well as the placement of catheters into the tail vein of mice was performed as described in the previous section (see 3.1.3).

3.3.4 Experimental Workflow

3.3.4.1 Longitudinal Monitoring of Islet Engraftment by Combined PET/MRI

A group of C3H mice (n=3), which was previously transplanted with ~600 islet cells per mouse, was monitored with a PET/MRI protocol until 4 weeks after the inoculation (Fig. 3.3.1a).

Following the induction of anesthesia, mice were treated with a stimulating glucose doses (1.5 g/kg) through the i.v. injection of 50 µL of glucose solution. Serial bolus injections of 50 µL [^{64}Cu]Ex4 (~0.12 MBq/g) and $MnCl_2$:Bicine (~75 µmol/kg) were administered five minutes after glucose stimulation.

The measurements consisted of a 20-min static PET scans on a stand-alone small animal PET scanner (dedicated Inveon PET, Siemens Healthineers, Knoxville, TN, USA). The animals were allowed 1 h of unconscious tracer uptake before the PET acquisition. Subsequently, the animal bed, holding the position of the mice, was transferred to an animal 7T BioSpec 70/30® scanner (Bruker BioSpin MRI GmbH, Ettlingen, DE). For MR imaging, the calf of the leg of mice was centered through a localizer pulse sequence, followed by the acquisition of a rapid VFA T_1 map.

After the last imaging point, the radioactivity of the muscle of transplanted and contralateral legs were measured by *ex vivo γ*-counter (Fig. 3.3.1b).

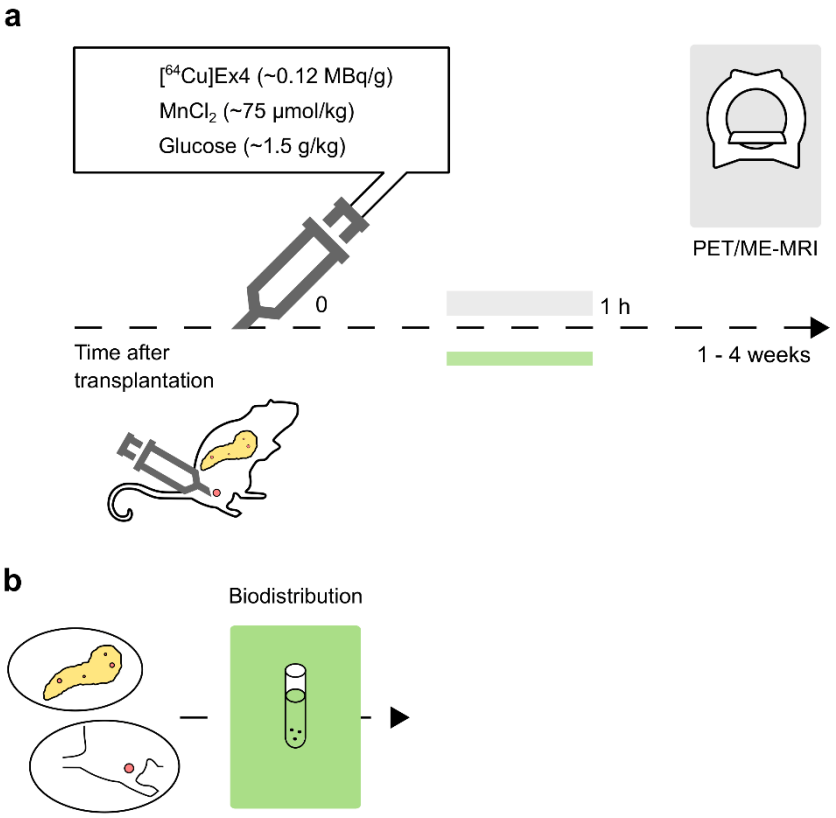

Fig. 3.3.1 Longitudinal evaluation of islet engraftment and follow-up of PET tracer retention by biodistribution

(**a**) Isolated and purified islets were measured longitudinally with PET/MRI between 1 and 4 weeks after transplantation. Combined PET/MRI acquisition was performed by injecting $MnCl_2$:Bicine (75 µmol/kg) contrast agent, and the PET tracer solutions (~0.12 MBq/g) 5 min after glucose solution (1.5 g/kg) administration. (**b**) *Ex vivo* biodistribution of tissues of interest, including the transplanted and contralateral muscle of the calf, was performed after the last imaging session.

3.3.4.2 Blocking of the VDCC Activity in Engrafted Islets by PET/MRI and Ex Vivo Analysis

Two separate cohorts of littermates, age-matched control C3H mice (n=4/4) were transplanted with ~600 previously isolated islets and assessed with an analog combined PET/MRI protocol five weeks after the inoculation of islets.

The mice were pre-treated with a volume of 50 µL of diazoxide solution (23 mg/kg) as a Ca^{2+} blocker dissolved in 0.1 M NaOH, or with the same volume of vehicle solution. After seven minutes, volumes of 50 µL of [^{64}Cu]Ex4 (~0.12 MBq/g) and $MnCl_2$:Bicine solution (~75 µmol/kg) were injected through the same tail vein catheter. To avoid an excess of injected volume, the stimulation with

glucose (1.5 g/kg) was performed 30 min after the injection of the contrast agent and PET tracer (Fig. 3.3.2a).

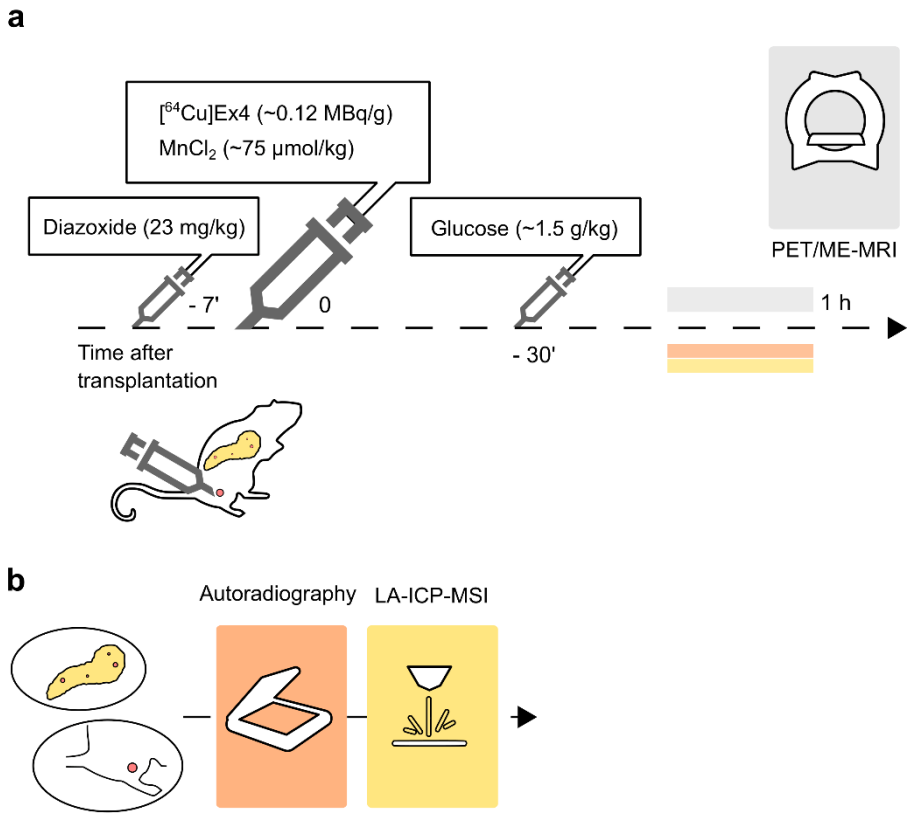

Fig. 3.3.2 *In vivo* inhibition of VDCC and *ex vivo* analysis of native and transplanted islet cells

(**a**) Transplanted animals (n=4/4) were measured with PET/MRI around 5 weeks after transplantation. A blocking dose of diazoxide (23 mg/kg) was administered i.v. 7 min before the co-injection of $MnCl_2$:Bicine (75 µmol/kg) contrast agent and the PET tracer solution (~0.12 MBq/g). A stimulation dose of glucose (1.5 g/kg) was administered 30 min after the PET tracer injection. (**b**) After the *in vivo* imaging experiment, *ex vivo* autoradiography followed by MS imaging of biometals were performed for the calf and pancreas sections.

After the isolation of the pancreas and muscle of the calf, their sections were measured by *ex vivo* autoradiography and LA-ICP-MS imaging (Fig. 3.3.2b).

3.3.5 MRI Acquisition

The calf of the leg of mice was centered in the FoV, followed by the acquisition of two consecutive 3D-GRE pulse sequences at different flip angles (TR/TE=10/1.9 ms, FoV=34×34×17 mm^3, matrix size 128×128, NA=2, BW=75 kHz, FAs=4°, 22°, isotropic resolution 0.3 mm). *In vivo* measurements were

carried out on a 7T BioSpec 70/30® scanner (Bruker BioSpin MRI GmbH, Ettlingen, DE) equipped with a RF-coil, 40 mm of inner diameter.

3.3.6 PET Acquisition

Static PET scans of 20 min were centered at the calf of the leg and acquired on an Inveon dedicated PET scanner (Siemens Healthineers, Knoxville, TN, USA) at 1 h after the PET tracer injection. The PET scanner was set as described in the previous section (see 3.2.6).

3.3.7 Γ-counter and Biodistribution

After the *in vivo* measurements, the transplanted and contralateral muscle of the calf, as well as the other tissues of interest, such as pancreas, liver, spleen, kidneys, the muscle as well as the intestine, were collected and measured using dedicated γ-counter tubes (Sardstdt AG & Co., Nümbrecht, DE). A set of standard vials were measured as reference to quantify the radioactivity in the organs. The vials were weighted before and after the transfer of the tissues using a precision scale (Sartorius, Göttingen, DE).

The counts were measured using a Wallac 1480 WIZARD 3” γ-counter (Perkin Elmer, Waltham, MA, USA) and the radioactivity decay corrected for ^{64}Cu ($T_{1/2}$=12.7 h). The signal was normalized for the injected activity (IA) and the tissue weights to calculate the %ID/g of the PET tracer.

3.3.8 Cryotome and Autoradiography

The preparation of transplanted calf and pancreas sections as well as the autoradiography were performed as described in the previous section (see 3.2.7).

3.3.9 LA-ICP-MS Imaging

Air-dried fresh frozen 20 µm thin sections of calf and pancreas were scanned with LA-ICP-MS imaging following the methods described in the previous section (see 3.2.8).

3.3.10 Image Analysis

3.3.10.1 PET Scan Reconstruction

Static PET data saved as list files were reconstructed on Inveon Acquisition Workplace (Siemens Heathineers) as described in the previous section (see 3.2.10.1).

3.3.10.2 PET/MRI Co-registration and VOIs Definition

The PET images were loaded on Inveon Research Workplace (Siemens Heathineers) and aligned to the MR images by using the leg of mice as anatomical reference. The VOIs were manually drawn for the engrafted islets and subsequently saved and imported to MATLAB for further analysis.

3.3.10.3 VFA T_1 Maps Quantification

The mean values ± SD of the VOIs measured from the VFA T_1 maps were analyzed as reported in the previous section (see 3.2.10.3).

3.3.10.4 PET Quantification

The processing and the quantification of the exported VOIs were performed as described in the previous section (see 3.1.7.6).

3.3.10.5 Phosphor Image Analysis

The autoradiography of pancreas sections was performed in accordance to the previous subsection (see 3.2.10.5). The mean values ± SD of the intensity and the spot diameter were measured throughout the muscle and pancreas. Subsequently, the signal was normalized for background and the surrounding tissue of each slice.

3.3.10.6 Post-processing of LA-ICP-MS Data

The elemental images of Ca, Mn and Zn for the calf and the pancreas sections of mice were reconstructed as described in the previous study (see 3.2.10.6).

3.3.11 Statistical Analysis

The mean ± SD calculated for each VOI were produced on MATLAB (Mathworks, Natick, MA, USA).

Differences in the PET/MRI measurements between 1 and 3 weeks were calculated by one-sample Student's *t*-test. The same test was applied to determine the significant differences in the quantification of tracer uptake between the contralateral and the transplanted muscle of the calf. The comparison between the mice pre-treated with diazoxide and control was performed through a two-sample Student's *t*-test.

3.4 Radioactive ^{52}Mn as Potential Dual PET/MRI Agent to Measure the Endocrine Pancreas

This section describes the methods and the study design used to investigate the biodistribution of ^{52}Mn as the free salt compared to ^{52}Mn complexed with DPDP, a weak chelator of divalent ions.

3.4.1 Animal Preparation

The anesthesia and the preparation of mice for the *in vivo* dynamic PET measurements was performed as described in the previous study (see 3.1.3).

3.4.2 Experimental Workflow

3.4.2.1 Dynamic PET to Monitor the Early Kinetic of Chelated ^{52}MnDPDP and $^{52}MnCl_2$

Two cohorts of 6 to 7-week-old C3H mice (n=3/3) were measured with a dynamic (0-1 h) PET protocol. The abdominal region was centered in the field of view of the scanner (Inveon dedicated PET scanner, Siemens Healthineers, Knoxville, TN, USA). The administration of bolus injection of ^{52}MnDPDP (~0.12 MBq/g) or the same dose of not chelated $^{52}MnCl_2$ was administered through the tail vein of mice few seconds after the beginning of the PET measurements.

3.4.2.2 Evaluation of the Early Kinetic of ^{52}Mn After Blocking of VDCC Activity Using Diazoxide as Ca^{2+} Inhibitor

Another group of C3H mice (n=2) was pre-treated with a volume of 50 µL of diazoxide solution (17 mg/kg) two minutes before the administration of radiolabeled ^{52}MnDPDP (Fig. 3.4.1) and measured using an analogue dynamic (0-1 h) PET protocol.

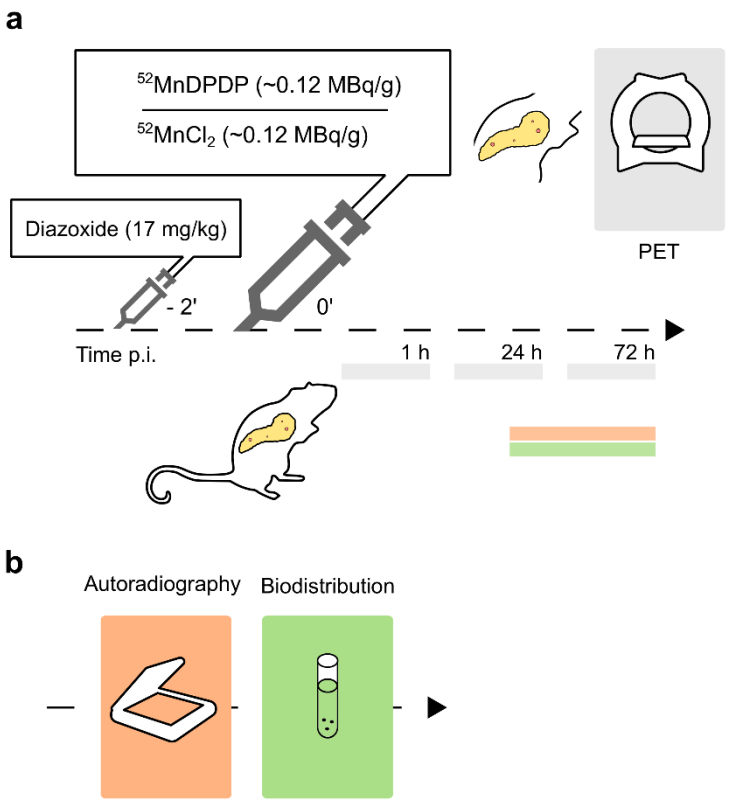

Fig. 3.4.1 Experimental ^{52}Mn PET workflow, *in vivo* blocking studies inhibiting VDCC activity and follow-up *ex vivo* by autoradiography and biodistribution

(**a**) Groups of healthy 6 to 7-week-old C3H mice were measured with dynamic (0-1 h) PET after the i.v. injection of $^{52}MnCl_2$ or ^{52}MnDPDP (n=3/3) at the same radioactive dose (~0.12 MBq). A high dose of diazoxide (17 mg/kg) was injected (n=2) few minutes before the administration of radioactive ^{52}MnDPDP in a separated control group. Static PET scans were acquired to monitor the in vivo the biodistribution of tracers at 24 h and 72 h post injection. (**b**) *Ex vivo* quantification of the accumulation of ^{52}Mn in the pancreas and brain sections were performed 72 h after the tracer injection by autoradiography of ^{52}Mn in both groups. *Ex vivo* experiments performed after the last imaging session consisted of the quantification of ^{52}Mn in the heart, the brain and the other tissues of interest by autoradiography and γ-counter.

3.4.2.3 Follow-up of the Late Accumulation of ^{52}Mn by PET and Biodistribution

In vivo follow-up measurements of ^{52}Mn distribution was performed at 24 h and 72 h after the systemic administration of tracer and by the acquisition of 30-min static PET scans. The late distribution of tracers within the tissues of interest was assessed by *ex vivo* autoradiography of the pancreas and brain sections and biodistribution of the tissues of interest after the last imaging session.

3.4.3 MRI Acquisition

Whole-body anatomical MR images were acquired after the PET acquisition on on a small animal 7T BioSpec 70/30® scanner (Bruker BioSpin MRI GmbH, Ettlingen, DE), which was equipped with a RF-coil 40 mm of inner diameter. For the acquisition of images, a protocol analogue to the one described in 3.1.5.1 was applied.

3.4.4 PET Acquisition

PET scans were performed on an Inveon dedicated PET scanner (Siemens Healthineers, Knoxville, TN, USA). The acquisition of both dynamic (0-1 h) and 30-min static PET scans at late time points (24 h and 72 h post injection) were set with a dedicated protocol for decay correction of ^{52}Mn. The other parameters were set as described in the previous study (see 3.2.6).

3.4.5 ^{52}Mn Production

The radioactive ^{52}Mn was prepared and provided by Dr. Jesper Fonslet at the Technical University of Denmark according to the published procedure (Fonslet et al., 2017). In brief, ^{52}Mn was produced via the ^{nat}Cr(p,n)^{52}Mn reaction, by 16 MeV proton irradiation of natural chromium. Separation of the ^{52}Mn from the chromium target material was performed by four sequential solid phase anion exchange purifications, trapping anionic $^{52}MnCl_x$ complexes out of ethanol-HCl mixtures.

3.4.6 DPDP Chelator Synthesis

The *N*,*N*'-dipyridoxylethylenediamine-*N*,*N*'-diacetic acid 5, 5'-bis(phosphate) (DPDP) ligand was prepared and provided by Dr. Gregory Bowden at the Department of Preclinical Imaging and Radiopharmancy (Tübingen, Germany) according to a modified version of the published procedure (Rocklage et al., 1989).

3.4.7 Radiolabeling of DPDP with ^{52}Mn

The radiolabeling of DPDP ligand was carried out by Gregory Bowden at the Department of Preclinical Imaging and Radiopharmancy (Tübingen, Germany)

facility as follows. $^{52}MnCl_2$ (15 MBq, 80 µl) was buffered with 1.5X volume of 0.5 M ammonium acetate buffer and, to this solution, was added 500 µg of DPDP in 10 µL of distilled water. The resulting solution was incubated at room temperature for 30 min. After radioTLC analysis (Cell 300, cellulose Polygram), MeOH/H_2O (7:3) showed the radiochemical conversion of the reaction to be 85%. The ^{52}MnDPDP solution (5% free $^{52}MnCl_2$) was diluted with saline for injection (NaCl 0.9%) to a final volume of 300 µL.

3.4.8 Γ-counter and Biodistribution

The isolation and the *ex vivo* quantification of the pancreas, brain, and other tissues of interest, which were isolated after the last imaging session, were performed in a way analogue to the previous study (see 3.3.7). The measured counts were decay corrected using the half-life time of radioactive ^{52}Mn ($T_{1/2}$=5.6 d).

3.4.9 Cryotome and Autoradiography

The isolation and preparation of pancreas and brain sections was performed 72 h after the injection of the PET tracer. The scanning and the quantification of the phosphor imaging plate were carried out as described in the previous section (see 3.2.7).

3.4.10 Image Analysis

3.4.10.1 PET Scans Reconstruction

The image list-mode files produced after the acquisition of dynamic and static PET scans were reconstructed using to the protocol described in 3.2.10.1, which was already implemented on Inveon Acquisition Workspace (Siemens Heathineers).

3.4.10.2 PET/MRI Co-registration and VOIs Definition

The PET images were loaded and overlaid to the anatomical whole-body MR images on Inveon Research Workplace (Siemens Heathineers). The images were co-registered by taking the anatomical landmark of the kidneys as

reference. The VOIs were manually drawn for the pancreas, liver, renal cortex, heart and the hot-spots in the brain. The mean values ± SD of VOIs were calculated, saved as text files and subsequently imported to MATLAB for further analysis.

3.4.10.3 PET Quantification

The mean values ± SD among the group of mice injected with either $^{52}MnCl_2$ or ^{52}MnDPDP were calculated and decay corrected for the decay time of ^{52}Mn ($T_{1/2}$=5.6 d) between the injection and the acquisition of the images.

3.4.10.4 Phosphor Image Analysis

The signal of hot-spots identified throughout the pancreas sections was quantified as described in the previous study (see 3.2.10.5). The mean values ± SD of the signal intensity were calculated for the entire brain sections and compared between the groups.

3.4.11 Statistical Analysis

The mean ± SD calculated of VOIs were calculated on MATLAB (Mathworks, Natick, MA, USA).

The comparison of *in vivo* PET measurements ($^{52}MnCl_2$, ^{52}MnDPDP and ^{52}MnDPDP + diazoxide) was calculated among the groups by using a pairwise comparison Tukey's HSD test followed by *post-hoc* correction with Bonferroni, 0.05 of Alpha level. The significance of ratio values, which were measured at early (24 h) and at late time points (72 h), were calculated by a two-sample Student's *t*-test.

3.5 PET Imaging to Investigate the Effect of a Quinoxaline Derivative

This section describes the methods and the study design used to assess the effect of a quinoxaline-derivate, namely C2, on the uptake of [^{64}Cu]Ex4 by the GLP-1R expressing tissue cells in different animal models.

3.5.1 INS-1 Xenograft Mouse Model

INS-1 cells were kindly provided by Prof. Dr. Martin Gotthardt at the Department of Nuclear Medicine at the Radboud University Nijmegen. Frozen aliquots of 2-5×10^6 cells in phosphate buffer solution (PBS), 10% dimethyl sulfoxide (DMSO) were stored at -80°C until needed. Approximatively 0.5-1×10^6 INS-1 cells were plated in 175 cm^2 cell culture flasks with a red cap filter in 15 mL of RPMI 1640 medium, 10% FCS, 10 mM HEPES, 1 mM sodiumpyruvate, 50 µM β-mercaptoethanol, penicillin (100 units/mL) and streptomycin (100 µg/mL) and kept at 37° C in a Heracell 150i cell incubator (Thermo Scientific, Karlsruhe, DE) at 5% CO_2.

Plated cells with less than twenty passages were split once a week by removing the medium, adding 2 mL of 0.05% trypsin/ 0.02% ethylenediaminetetraacetic acid (EDTA) and incubated for 2-3 min at 37°C until cells are detached from the flask. After three washes in PBS, the cells were centrifuged at 1200 RPM for 5 min, re-suspended in fresh medium and plated in flasks. For the inoculation, cells were centrifuged, re-suspended in 10 mL PBS and counted by using Neubauer improved cell counter chamber (Assistant, Sondheim, DE) by pipetting 10 µL of cell suspension mixed with 90 µL of trypan blue. The cells were centrifuged again, re-suspended in PBS at a concentration of 5×10^7/0.2 mL. Therefore, 1×10^6 cells were subcutaneously inoculated into the upper shoulder of 6 to 8-weeks-old female BALB/c NUDE mice (Charles River, Sulzfeld, DE).

PET imaging of mice carrying the INS-1 cells-derived tumors was performed between 4 to 5 weeks after the inoculation of the cells, when the tumors reached a diameter ranging between 2 and 5 mm. The blood glucose levels and the tumor growth were respectively monitored with a blood glucose analyzer (HemoCue Hb 201+, HCE, UK) and a caliper to avoid severe hypoglycemia (<30 mg/dL).

3.5.2 Transplanted Mouse Model

Cohorts of littermate and age-matched C3H mice (Charles River, Sulzfeld, DE) were ordered, divided among the donor and recipient groups (n=30/10) and maintained one week before the surgery and the inoculation of islets into the muscle of the calf of mice. The materials and procedure of surgery is described in the previous section (see 3.3.3).

3.5.3 Quinoxaline Synthesis

The synthesis of quinoxaline derivative *N*-(*tert*-butyl)-6, 7-dichloro-3-(methylsulfonyl) quinoxalin-2-amine, referred as compound 2 (C2), was carried out by Gregory Bowden at the Department of Preclinical Imaging and Radiopharmancy (Tübingen, Germany). The synthesis was performed in four steps according the procedure published by Teng et al. (Teng et al., 2007) from 2, 3, 6, 7-tetrachloroquinoxaline with an overall yield of 68%. The structure and purity of the compound were confirmed by ^{1}H and ^{13}C NMR spectroscopy and HPLC-MS.

3.5.4 Radiolabeling of [^{64}Cu]Ex4

The labelling of peptide with ^{64}Cu was carried out as described in the previous section (see 3.1.2).

3.5.5 Animal Preparation

The anesthesia and the preparation of the tail catheters was performed as previously described (see 3.1.3).

3.5.6 Experimental Workflow

3.5.6.1 Blocking Study of GLP-1R in an INS-1 Xenograft Mouse Model

A control group of INS-1 tumor-bearing NUDE BALB/c mice (n=3) received only the PET tracer injection. Another group was treated with C2 (7 mg/kg, n=2 or 14 mg/kg, n=2) 15 min before the administration of the PET tracer. A blocking dose of non-radioactive Ex4 peptide (30 mg/kg, n=1) was injected 3 min before the PET tracer injection (~0.12 MBq/g). To determine the potential effects of the two

compounds on the PET tracer uptake, one of the two animals treated with C2 (7 mg/kg) received non-radioactive Ex4 (30 mg/kg) 3 min before the PET tracer administration.

After a period of unconscious uptake time of tracer (~1 h post injection), the mice were positioned on a dedicated animal bed and placed in the FoV of an Inveon dedicated PET scanner (Siemens Healthineers, Knoxville, TN, USA) and measured with a 10-min static PET imaging protocol (Fig. 3.5.1).

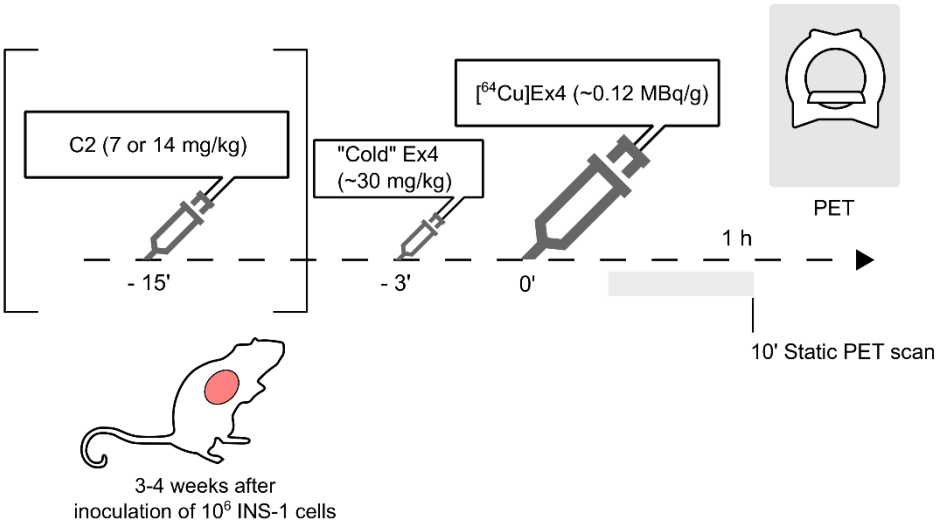

Fig. 3.5.1 Blocking of GLP-1R in an INS-1 xenograft mouse model

NUDE BALB/c mice were measured between 4 and 5 weeks after the subcutaneous inoculation of $1*10^6$ INS-1 cells behind the right shoulder. Mice were treated with C2 (7 or 14 mg/kg) or with non-radioactive ("cold") Ex4 (30 mg/kg) at 15 and 3 min, respectively, before the intravenous injection of [^{64}Cu]Ex4 solution (~0.12 MBq/g). Static PET scans of 10 min were acquired 1 h after the PET tracer injection.

3.5.6.2 Evaluation of Different Doses of Quinoxaline in an INS-1 Xenograft Mouse Model

In another experiment, different cohorts of littermate age-matched INS-1 xenograft NUDE BALB/c mice (n/group=4) were treated with 75 µL of C2 (15, 25 and 35 mg/kg) or a vehicle solution. The solution containing the quinoxaline compound was administered 15 min or 30 min before or co-injected together with 25 µL of PET tracer solution (~0.04 MBq/g) through the same tail vein catheter. Dynamic (0-1 h) PET scans were performed on the groups of mice treated either with C2 or vehicle solution (n=2/2) 15 min before the tracer administration. *In vivo*

measurements consisted of the acquisition of 10-min static PET scans centered on the tumors of mice, which were previously allowed 1 h of unconscious uptake. Follow-up measurements with static PET scans were performed 24 h post injection. After the last session (48 h post injection), the INS-1 tumors were excised and measured with a γ-counter (Fig. 3.5.2b).

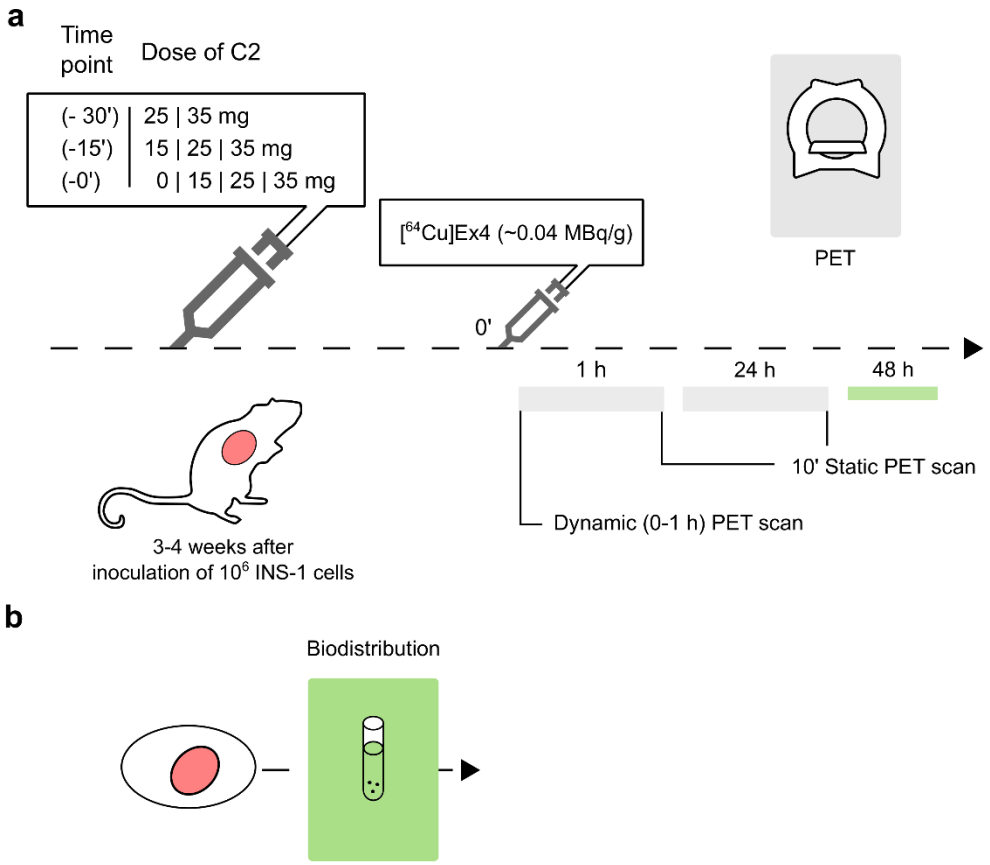

Fig. 3.5.2 Study design to determine the allosteric modulation of C2 on GLP-1R

Groups of NUDE BALB/c mice were measured with a (**a**) static 10-min and dynamic (0-1 h) PET scans at 1 h after the injection of [^{64}Cu]Ex4 (~0.04 MBq/g). *In vivo* follow-up of tracer uptake was performed at 24 h by acquiring a 10-min static PET scan. The graph shows the different conditions of groups (n/group=4), including the C2 doses (15, 25 and 35 mg/kg) and injection time points (15, 30 and 0 min) before the administration of the radiotracer. (**b**) *Ex vivo* biodistribution of INS-1 tumors was performed at 48 h.

3.5.6.3 Assessment of Quinoxaline Challenge on the Tracer Uptake by the Engrafted Islets

A cohort of transplanted C3H mice (n=10) underwent dynamic (0-1 h) PET measurements four weeks after inoculation with ~650 islets. After the animals were positioned on the bed, the leg containing the transplanted islets was

stretched, taped away from the main body and centered in the field of view of a dedicated small animal PET scanner.

Mice with engrafted islets (n=6 out of 10) were further assessed using a dynamic (0-1 h) PET protocol six weeks after the transplantation. The PET tracer was continuously infused (0-50 min; 120 µL/h; 0.24 MBq/g) using a dedicated infusion pump (Harvard Apparatus, March-Hugstetten, DE) through the tail vein of mice. As is illustrated in Fig. 3.5.3, 25 µL of C2 solution (2 or 5 mg/kg) was administered as a bolus through the contralateral tail vein 20 min after the beginning of the infusion.

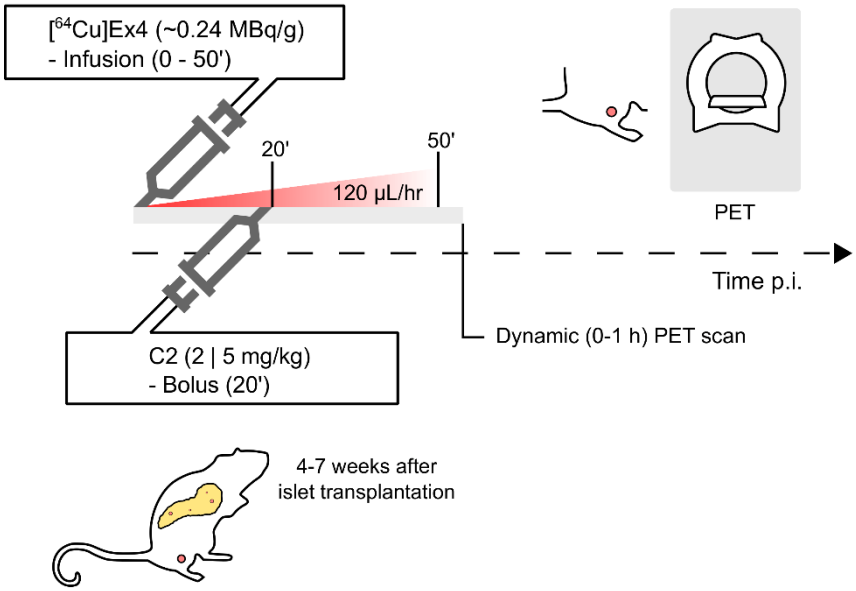

Fig. 3.5.3 An infusion dynamic PET imaging protocol to monitor the effect of C2 in the engrafted islets

Groups of mice were treated with 2 or 5 mg of C2 (n=2/2) injected as a single bolus during the acquisition of dynamic (0-1 h) PET scans and the infusion of [^{64}Cu]Ex4 between 0-50 min (~0.24 MBq, 120 µL/h).

3.5.6.4 Evaluation of a Bolus-Infusion Protocol to Monitor the Effect of Quinoxaline in the Pancreas

In another experiment, a bolus-infusion protocol was examined on a small group of healthy C3H mice (n=3/3). Therefore, mice were treated via single tail catheter with a solution of the PET tracer mixed with C2 solution (33 µL; 100 µL/min; 1.7 mg/kg; ~0.08 MBq/g), following the infusion of the remaining volume (67 µL; 80 µL/h; 3.3 mg/kg; ~0.16 MBq/g) until 50 min post injection (Fig. 3.5.4a). *In vivo*

measurements were performed through the acquisition of dynamic (0-1 h) PET scans.

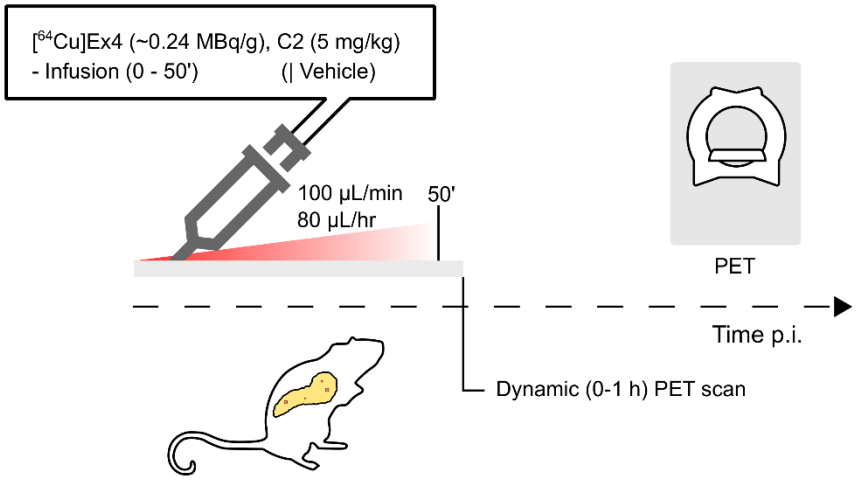

Fig. 3.5.4 Bolus-Infusion to monitor the effect of C2 in the pancreas

A cohort of littermate C3H mice was monitored dynamic (0-1 h) with PET scans during a bolus-infusion (100 µL-min-80 µL/h) of [^{64}Cu]Ex4 (~0.24 MBq), C2 (5 mg/kg) solution or radioactive tracer solution with vehicle solution (n=3/3) between 0-50 min.

3.5.7 PET Acquisition

PET images were acquired on Inveon dedicated PET scanner (Siemens Healthineers, Knoxville, TN, USA). The setting of dynamic (0-1 h) and 10-min static PET scans were set as previously described (see 3.2.6).

3.5.8 Γ-counter and Biodistribution

The INS-1 tumors and the other tissues of interest were isolated 48 h after the injection of the tracer and measured according to the procedure described in the previous section (see 3.3.7).

3.5.9 Image Analysis

3.5.9.1 PET Scan Reconstruction

Dynamic and static PET list data measured on an Inveon dedicated PET scanner (Siemens Healthineers, Knoxville, TN, USA) were subsequently reconstructed according to the previous section (see 3.2.10.1).

3.5.9.2 VOIs Definition

The PET images were loaded on Inveon Research Workspace (Siemens Heathineers) and the signals were thresholded for the IA of each animal. The VOIs were manually drawn for the INS-1 tumors or the engrafted islets to calculate the mean values ± SD of the areas. The mean values of VOIs were saved and exported as text files and subsequently imported to MATLAB for further quantification.

3.5.9.3 PET Quantification

The text files of VOIs were imported on MATLAB and quantified in accordance with the previous section (see 3.1.7.6).

3.5.10 Statistical Analysis

The mean ± SD calculated of VOIs were calculated on MATLAB (Mathworks, Natick, MA, USA).

Differences in the tracer uptake (%ID/mL) between the control group and the groups treated with non-radioactive Ex4 were calculated by using a two-sample Student's *t*-test assuming unequal variance and Alpha level 0.05.

Multiple comparison control Steel's test was performed to determine the significance of the ratio values between the mice treated with different doses of C2 (doses and time points) and the control group.

All animal experiments have been approved by the Regierungspräsidium Tübingen under the file numbers R 3/18, R 5/15, R 7/15.

4 Results

4.1 Establishment of *In Vivo* PET/ME-MRI Protocols

4.1.1 A Combinatorial Analysis to determine the Accuracy of Limited and Multiple FAs in the quantification of VFA T_1

The T_1 value of phantoms were calculated by an IRSE method and used as reference values to determine the accuracy of VFA T_1 mapping protocols. As shown in the graphs, increasing concentrations of paramagnetic contrast agent resulted in a respective reduction of the measured T_1 (Fig. 4.1.1a). The linear regression analysis of the R_1 ($1/T_1$) measured in each vial produced positive slope coefficients, equal to 6.96 and 4.36, for the phantom studies containing serial dilution of Mn and Gd-based contrast agents, respectively (Fig. 4.1.1b). In Fig. 4.1.1c are plotted the R_1 values obtained from the acquisition of a two-angle VFA T_1 mapping method (4, 23°) using, respectively, 2 or 20 NA, against the reference R_1 values calculated by an IRSE method.

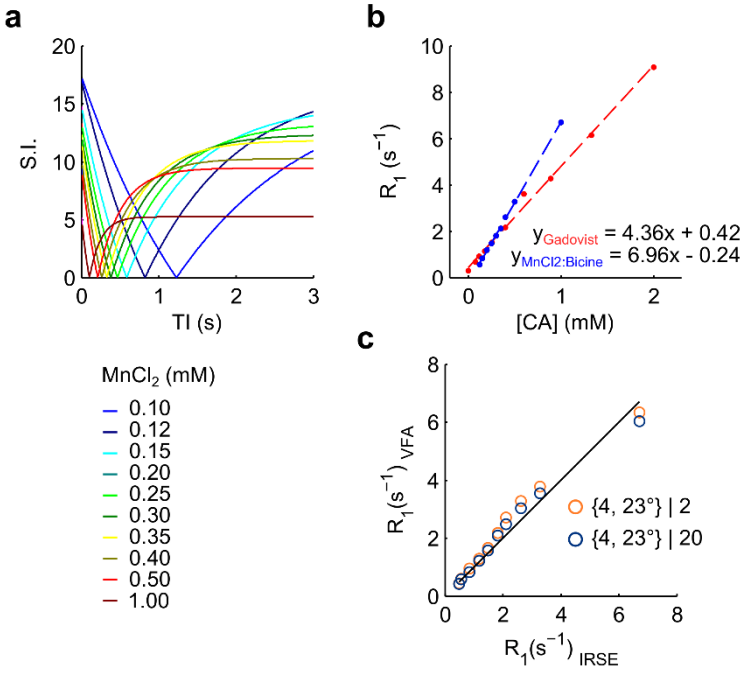

Fig. 4.1.1 Relaxometry of Mn and Gd contrast agents

(**a**) The curves describe the fitted signal intensity measured by the acquisition of IRSE images at different time of inversion (TI) of a phantom containing increasing concentrations of $MnCl_2$:Bicine solution (0.10-1.00 mM). (**b**) The R_1 values for Mn (blue dots) and Gd solutions (red dots) are plotted against the respective concentrations and fitted by linear regression. The linear equations are displayed for the Mn and Gd phantoms, respectively. (**c**) The VFA R_1 values calculated using two ideal FAs (4°, 23°) and number of acquisitions 2 (dark orange) or 20 (dark blue), are plotted against the linearly fitted IRSE R_1 values (black line). The graphs were adapted from the research article (Michelotti et al., 2020).

In the following studies, the accuracy of VFA T_1 by using additional FAs for the estimation of T_1 was evaluated. In this regard, the estimated percentages of error were produced for combinations of two, three, four, six, and ten FAs. As the number of flip angles increases, the estimated error decreases suggesting a respective increase in the T_1 accuracy. The errors calculated for three and four FAs were 1.3 and 1.6 times, respectively, lower compared to a two-angle method (Fig. 4.1.2a, b and Table 4.1.1). A slighter improvement in the T_1 accuracy was also observed for the images that were acquired using a higher number of acquisitions (NA=20) (Fig. 4.1.2c, d and Table 4.1.1) for two and three FAs, respectively.

Table 4.1.1 Mean values ± SD of the percentage of error (%) estimated for different combinations of FAs

Estimated error (%) in the estimation of T_1

Phantom experiment	(1)		(2)	(3)	
Number of Acquisitions	2	20	1	2	6
2FAs	12.8±1.2	10.2±0.6	5.2±0.4	2.6±0.2	8.5±1.6
3FAs	10.2±1.4	9.6±0.6	5.1±0.2	2.3±0.1	9.4±1.0
4FAs	7.8±0.9	9.2±0.5	5.0±0.1	2.0±0.1	9.8±0.6
6FAs	6.8±0.4	9.2±0.3	4.9±0.1	2.0±0.1	10.2±0.3
10FAs	8.3±0.2	12.3±1.6	5.0±0.1	1.9±0.1	12.0±0.5

Compared to those results, the estimated T_1 values calculated using ten FAs produced error values higher than four and six FAs (Table 4.1.1). This tendency

was also stronger for the images acquired at higher number of acquisitions (NA=20).

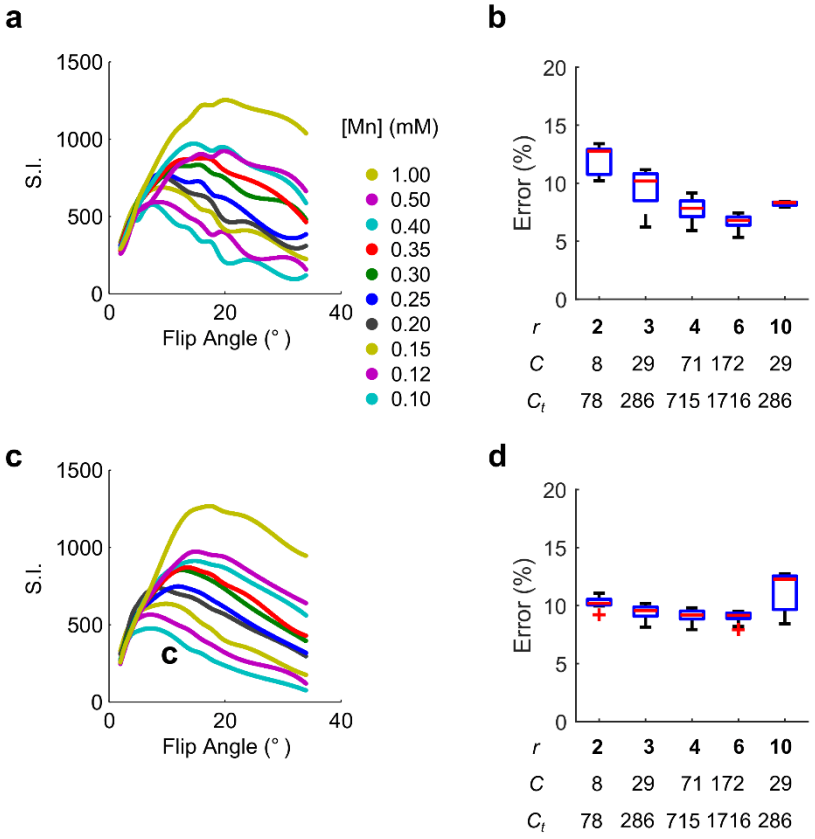

Fig. 4.1.2 Estimated errors for GRE images acquired at 2 and 20 NA

The fitted spline lines describe the signal intensity of 3D-GRE images acquired at different flip angles (2-34°) of each phantom capillary filled with $MnCl_2$:Bicine (0.10-1.00 mM) using (**a**) 2 or (**c**) 20 number of acquisitions. The boxes show the interquartile range and the mean values (red line) of the percentage of error. Outliners (red cross) are displayed in the graphs and represents the values 1.5 times higher and below 1st and 3rd quartile. The estimated errors were produced for each possible combination of FAs using increasing numbers of flip angles (*r*=2, 3, 4, 6, 10) for the images acquired at (**b**) 2 or (**d**) 20 number of acquisitions. The plotted error values (*C*) reflect the 10th percentile of the entire datasets (C_t).

In the second phantom experiment, the T_1 measurements were performed through the acquisition of slab-selective RF-spoiled GRE pulse sequences at different flip angles. Despite each vial at increasing concentrations of $MnCl_2$:Bicine solution displayed stable signal curves for increasing FAs (Fig. 4.1.3a), the percentages errors showed only a slight improvement of the T_1 accuracy (Fig. 4.1.3b and Table 4.1.1).

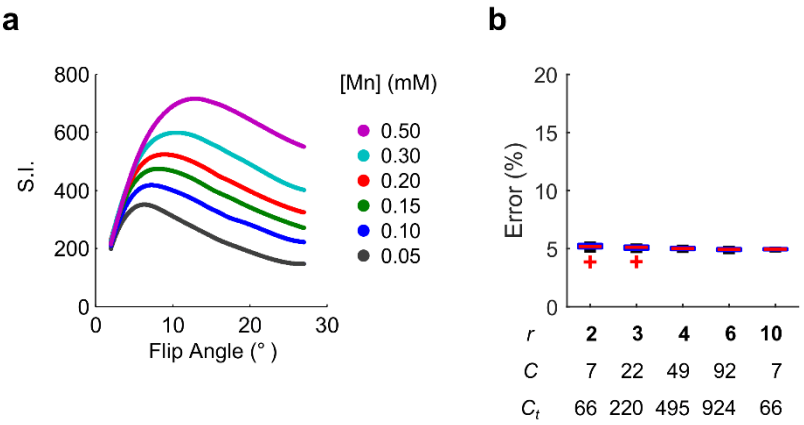

Fig. 4.1.3 Estimated T_1 accuracy using different combinations of FAs

(**a**) The plotted lines show the signal intensity fitted with a spline function for each cryovial filled with serial dilutions of $MnCl_2$:Bicine (0.05-0.50 mM) on a 7T BioSpec 70/30® scanner (300 mT/m). (**b**) The boxes show the interquartile range and the mean values (red line) of the percentage of error. Outliners (red cross) are displayed in the graphs and represents the values 1.5 times higher and below 1st and 3rd quartile. The estimated errors were produced for each possible combination of FAs using increasing numbers of flip angles (r=2, 3, 4, 6, 10). The plotted error values (C) reflect the 10th percentile of the entire datasets (C_t).

In the last experiment, a slab-selective RF-spoiled GRE protocol was examined on the same MRI scanner, which was equipped with an insert gradient coil enabling the acquisition of images at higher gradient strength (660 mT/m). As observed in the first experiment, a decrease of the estimated errors was observed for those combinations using more than two data points. In this regard, the accuracy increases for the T_1 values that were calculated using three and four FAs, which displayed errors equal to 1.1 and 1.3 times lower than those calculated using two FAs (Fig. 4.1.4a, b and Table 4.1.1).

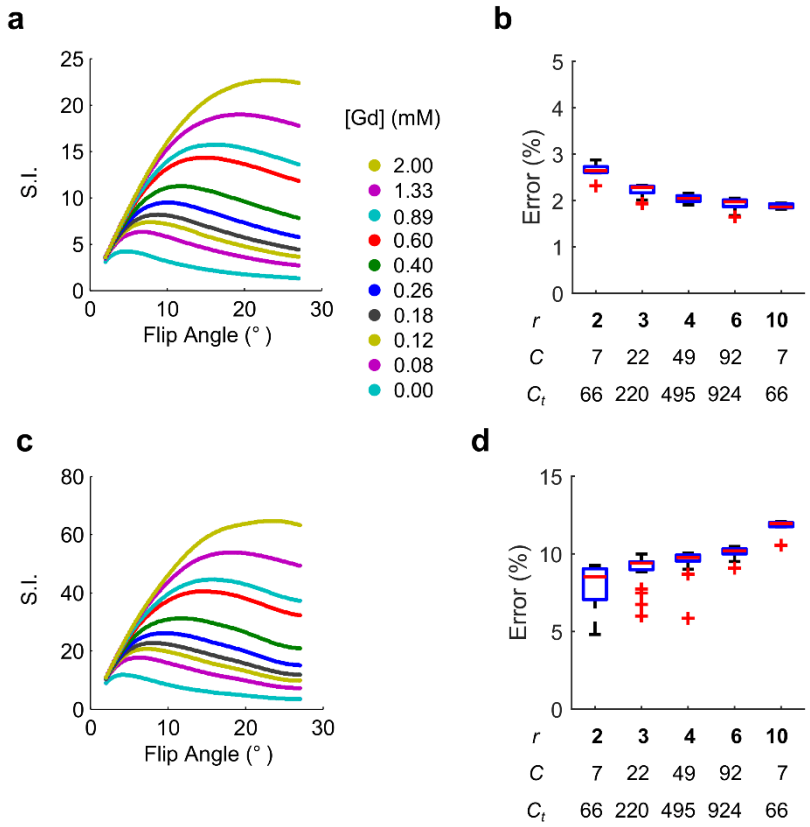

Fig. 4.1.4 Estimated error at higher gradient strength using high or low number of acquisitions.

The plotted lines show the signal intensity fitted with a spline function for each cryovials filled with serial dilution of NMR tube phantom filled serial dilution of Gadovist (0.08-2.00 mM) measured with (**a**) 2 or (**c**) 6 of number of acquisition at higher gradient strength (660 mT/m). The boxes show the interquartile range and the mean values (red line) of the percentage of error. Outliners (red cross) are displayed in the graphs and represents the values 1.5 times higher and below 1st and 3rd quartile. The estimated errors were produced for each possible combination of FAs using increasing numbers of flip angles (*r*=2, 3, 4, 6, 10) for the images acquired at low (**b**) (2) and (**d**) high (6) number of acquisitions. The plotted error values (*C*) reflect the 10th percentile of the entire datasets (C_t).

As it has been observed in the previous experiment, the analysis of images acquired at higher number of acquisitions (NA=6) resulted in the production of higher error compared to those at lower number of acquisitions (NA=2) (Fig. 4.1.4c, d and Table 4.1.1).

4.1.2 A VFA T_1 and a STIR Protocol to Monitor the Accumulation of Mn in the Pancreas

Based on the quantification of T_1 of the pancreas (840 ms) by using an IRSE method (Fig. 4.1.5a), a STIR protocol (TI=600 ms) was designed to monitor the

tissue uptake of Mn-based contrast agent. Statistical description of signals was performed by grouping 9-week-old control and RIP1-Tag2 mice (n=1/1). The measures obtained from the analysis of the pancreas showed mean values ± SD of signal enhancement equal to 366.2±345.3 to 41.7±6.3, suggesting a progressive wash-out of the contrast agent between 1 h and 24 h after the injection (Fig. 4.1.5b). In agreement with those results, the quantification of VFA T_1 using a two-angle method revealed [Mn] values decreasing from 1.6±0.9 to 0.5±0.0 mM×10^{-1}, respectively. Moreover, a marked wash-out of contrast agent was monitored in the renal cortex, which showed [Mn] values decreasing from 3.9±0.2 to 0.6±0.1 mM×10^{-1} (Fig. 4.1.5c and Table 4.1.2). In Fig. 4.1.5 is illustrated the representative the T_2-w and PET images, and the corresponding STIR images, which were acquired before and after the injection.

Table 4.1.2 PET/MRI quantification of Mn and [^{64}Cu]Ex4 between 1 h and 24 h post injection

T_1 maps, STIR and PET quantification overtime

	MRI						PET	
	R_1 (s^{-1})		[mM] (mM×10^{-1})		SE (%)		%ID/mL	
Time point	1 h	24 h	1 h	24 h	1 h	24 h	1 h	24 h
Pancreas	1.8±0.6	1.0±0.0	1.6±0.9	0.5±0.0	366.2±345.3	41.7±6.3	7.6±0.5	9.2±2.1
Renal	3.5±1.3	1.1±0.1	3.9±0.2	0.6±0.1	437.4±100.0	76.8±30.2	29.8±7.0	32.3±4.5
Spleen	0.8±0.2	0.7±0.0	0.5±0.2	0.3±0.1	95.0±2.6	NaN	4.5±1.2	4.5±0.4

The dynamic (0-1 h) PET scans were recorded simultaneously with the acquisition of MRI to follow-up the accumulation of [^{64}Cu]Ex4 and Mn in the pancreas. A steady accumulation of PET tracer was observed in the renal cortex between 0-1 h, with values reaching 29.8±7.0 %ID/mL (Fig. 4.1.5d). A strong retention was also observed at late time points (24 h) in both renal cortex and pancreas displaying values equal to 32.3±4.5 and 9.2±2.1 %ID/mL, respectively (Fig. 4.1.5e, Table 4.1.2).

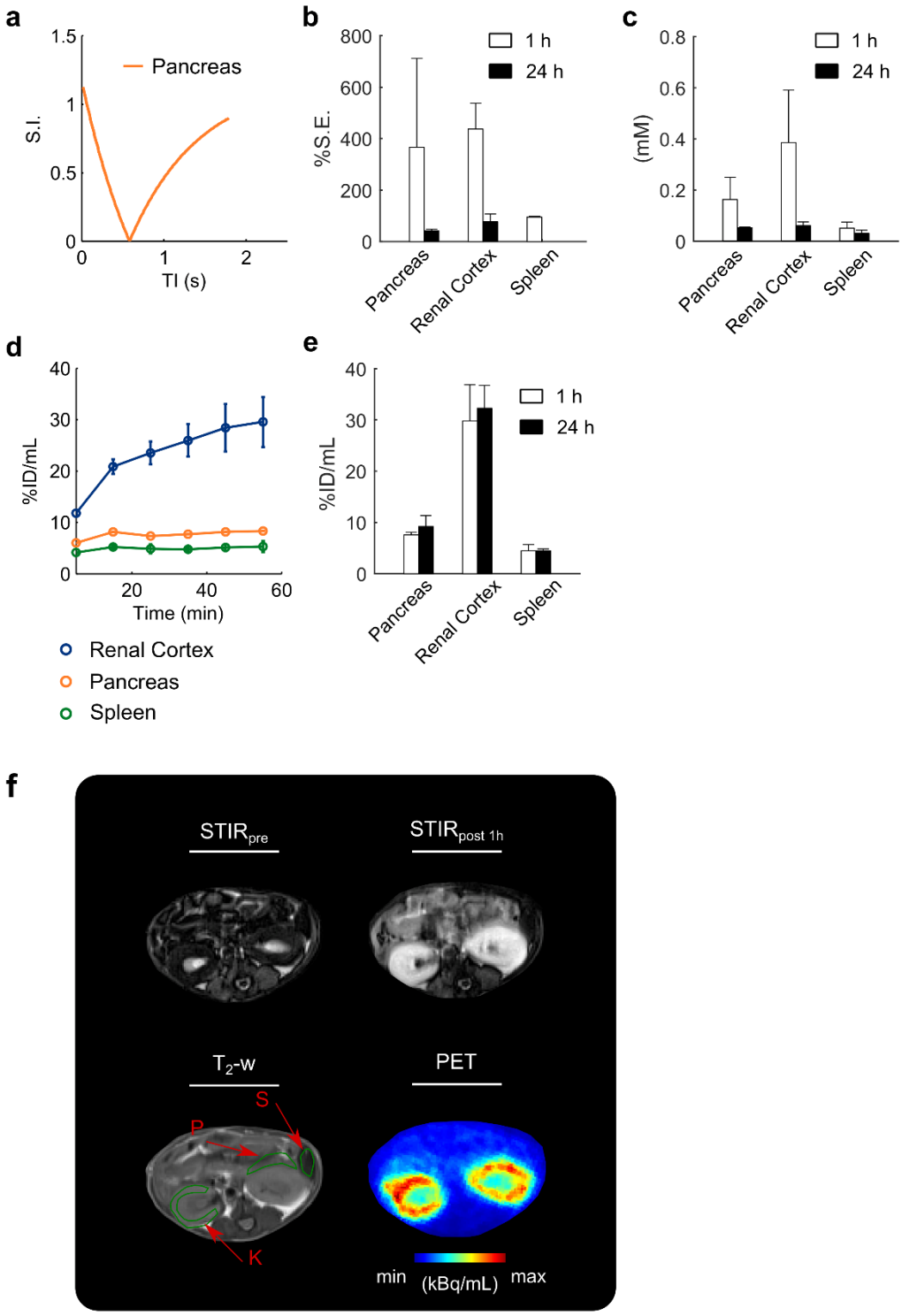

Fig. 4.1.5 *In vivo* follow-up of Mn and radiolabeled Ex4 in pancreas, renal cortex and spleen

(**a**) The fitted curve of the signal intensity of the pancreas was obtained by the acquisition of IRSE images at increasing time of inversion (TI). The bar plots represent the mean values ± SD of (**b**) the percentage of signal enhancement (%S.E.) and (**c**) the concentrations of Mn ([mM]) estimated by the ΔR_1 values at 1 h and 24 h. (**d**) The dynamic (0-1 h) PET curves show the mean values ± SD of the %ID/mL of radiolabeled Ex4 measured in the tissues of interest. (**e**) The bar chart shows the mean values ± SD of the %ID/mL from

20-min static PET measured at 1 h and 24 h after the tracer injection. (**f**) PET/MR images acquired simultaneously from a single representative animal are shown. The region of interest (green contours), including the pancreas (P), the spleen (S) and the renal cortex (R) are indicated with red arrows. STIR images show the enhancement of signal before and 1 h after the injection of contrast agent.

A group of 7-week-old control RIP1-Tag2 mice (n=8) was monitored using an analogue PET/MR imaging setup. The acquisition of PET/MR images was performed one day after the intraperitoneal bolus injection of Mn-based contrast agent and glucose solutions. The analysis of PET revealed a progressive wash-out of the PET tracer with values decreasing from 103.2±6.6 to 67.7±8.8, and 14.6±5.1 to 9.9±5.0 %ID/mL between 1 h and 24 h in the renal cortex and the pancreas, respectively (Fig. 4.1.6a and Table 4.1.3).

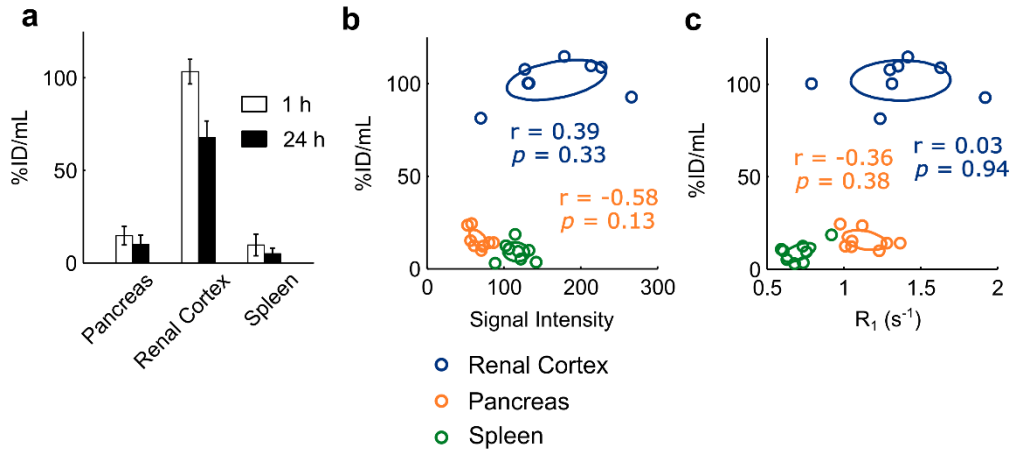

Fig. 4.1.6 PET/MRI correlation analysis

The bar plots represent the mean values ± SD of (**a**) the %ID/mL measured at 1 h and 24 h after the injection of the PET tracer. The calculated mean uptake values (%ID/mL) of each region of interest are plotted against (**b**) the co-registered MR signal of STIR images and (**c**) the R_1 values calculated by two-angle VFA T_1 maps. The Pearson *r* coefficients are displayed for the renal cortex (dark blue circles) and the pancreas (dark orange circle) assessing the correlation measured 1 h after the co-injection of PET tracer and Mn-based contrast agent. The ellipses reflect the variance in the PET/MRI measurements for all the tissues of interest.

The correlation analysis of the MR and PET images acquired at 1 h produced weak to moderate negative correlation coefficients in the pancreas (r=-0.58, *p*=0.13) (Fig. 4.1.6b, c).

Despite differences were not detected from the analysis of R_2 values (Fig. 4.1.7a), decreases between 24 h and 48 h were observed by evaluating the R_1 values and the S.I., with values decreasing from 1.1±0.1 to 0.7±0.1 s^{-1} and 67.9±11.5 to 46.4±13.8 in the pancreata, respectively (Fig. 4.1.7b, c and Table 4.1.3).

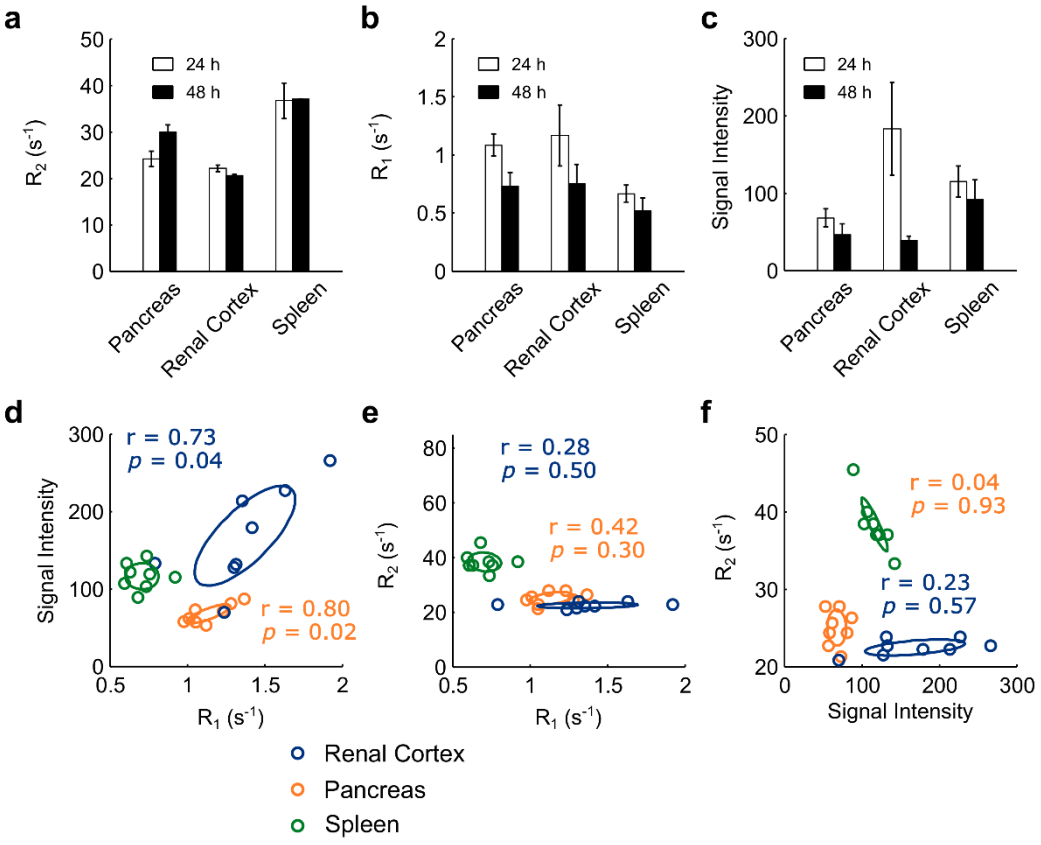

Fig. 4.1.7 Quantification and correlation analysis of MRI measurements

The plots show the mean values ± the SD of (**a**) the R_2, (**b**) the R_1 and (**c**) the S.I. measured at 24 h and 48 h for the abdominal regions of mice, including pancreas, renal cortex and the spleen. The Pearson's *r* coefficients show (**d**) the relation between the MR signal of STIR images with the R_1 as well as the relation of R_2 values (**e**) with R_1 and (**f**) STIR images for the pancreas (dark orange circle) and the renal cortex (dark blue circle) measured at 24 h. The ellipses show the SD of MRI measurements for all the tissues of interest.

The resulting correlation analysis indicated a moderate and positive correlation between the T_1 values and the S.I. measured in the pancreas (r=0.80, p=0.02) and renal cortex (r=0.73, p=0.04) (Fig. 4.1.7d). By contrast, the analysis of T_2 values showed only weak coefficients when they were correlated with the other MRI measurements (Fig. 4.1.7e-f).

Table 4.1.3 MRI and PET at 24 h and 48 h after the intraperitoneal injection of Mn contrast agent

MRI and PET quantification overtime of pancreas, renal cortex and spleen

	MRI						PET	
	R_1 (s^{-1})		R_2 (s^{-1})		STIR (a.u.)		%ID/mL	
Time point	1 h	24 h	1 h	24 h	1 h	24 h	1 h	24 h
Pancreas	1.1±0.1	0.7±0.1	24.2±1.7	29.9±1.5	67.9±11.5	46.4±13.8	14.6±5.1	9.9±5.0
Renal Cortex	1.2±0.3	0.8±0.2	22.1±0.7	20.6±0.2	183.1±60.0	39.1±5.0	103.2±6.6	67.7±8.8
Spleen	0.7±0.1	0.5±0.1	36.9±3.8	37.0±0.0	114.9±19.8	91.6±25.7	9.6±5.8	5.0±3.1

4.2 Simultaneous PET/MRI Measures BCM and Function

4.2.1 Mn uptake Negatively Correlated with Radiolabeled Ex4

The analysis of dynamic (0-1 h) PET scans indicate that the PET tracer was retained in the pancreas of healthy and RIP1-Tag2 mice between 20 min and until 1 h (Fig. 4.2.1a). The images of the abdominal region of healthy and transgenic mice show the overlaid PET and T_1 values measured with a simultaneous PET/MR imaging setup (Fig. 4.2.1b).

The PET signal registered between 40 and 60 min of the dynamic PET measurements was evaluated. The values quantified from the detected pancreatic insulinomas of transgenic mice are reported as reference. PET tracer uptake was significantly higher in the pancreas of 13-week-old RIP1-Tag2 mice ($t(3.67)=4.32$, $*p=0.01$) (Fig. 4.2.1c) compared to the healthy mice. By contrast, analysis of T_1 suggested a greater accumulation of Mn in the pancreas of control mice compared to the transgenic animals ($t(3.18)=-2.75$, $p=0.06$) (Fig. 4.2.1d).

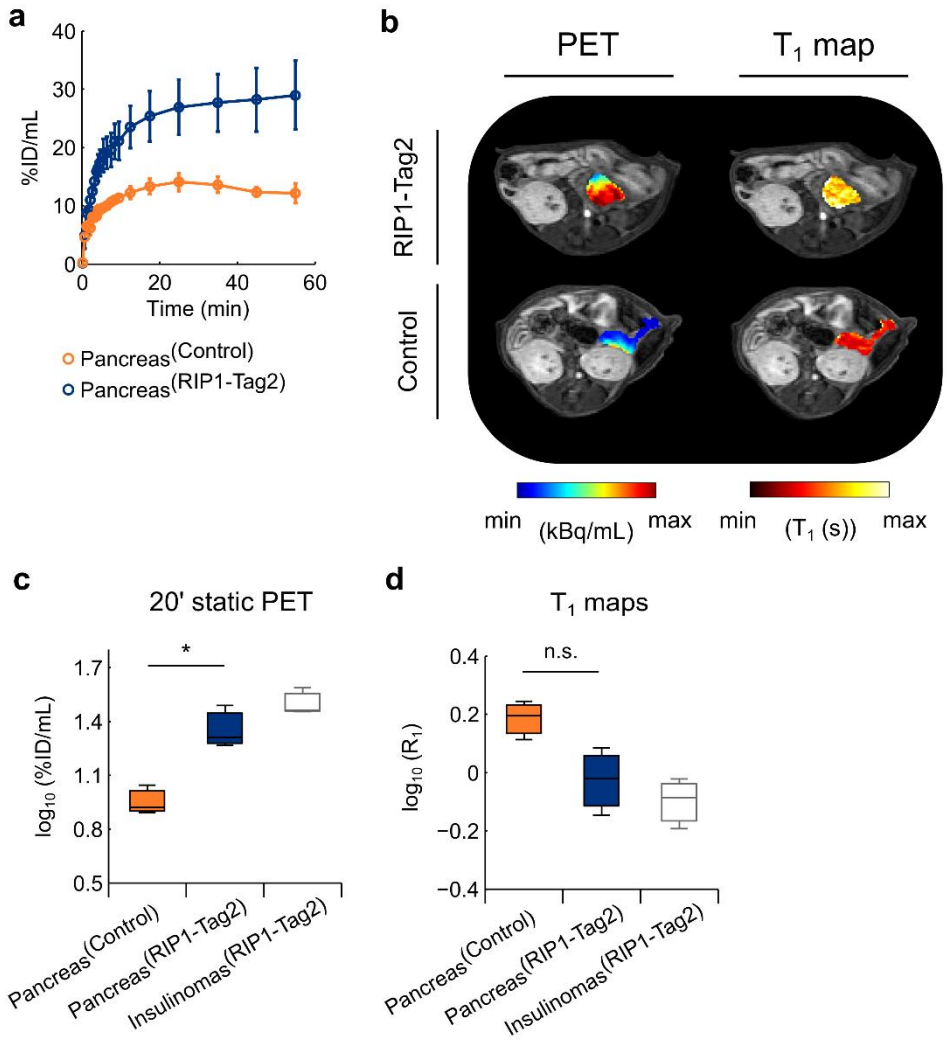

Fig. 4.2.1 PET/MRI indicate low accumulation of Mn at early time point (1 h) in the pancreas of transgenic mice.

(**a**) Dynamic (0-1 h) uptake curves display the mean values ± SD calculated from the entire VOIs of pancreata from the control (dark orange) and transgenic RIP1-Tag2 mice (dark blue). Next is illustrated the (**b**) representative images acquired *in vivo* at 1 h for healthy and transgenic mice with the respective scaled values of PET (kBq/mL) and T_1 maps (s) co-registered to the reference anatomical MR image. The boxplots show the (**c**) $\log_{10}$(%ID/mL) and (**d**) $\log_{10}(R_1)$ calculated from the processing of voxels of VOIs of healthy ($Pancreas^{Control}$) and transgenic ($Pancreas^{RIP1\text{-}Tag2}$) pancreata. The quantification of pancreatic insulinomas ($Insulinomas^{RIP1\text{-}Tag2}$) is shown as further reference. The length of whiskers is equal to 1.5 times the interquartile range of the 1st and 3rd quartile. Group comparison for PET ($t(3.67)=4.32$, $^*p=0.01$) and ME-MRI ($t(3.18)=-2.75$, $p=0.06$) was performed using a two-sample Student *t*-test assuming unequal variance between the groups. The graphs and the images were adapted from the research article (Michelotti et al., 2020).

The analysis of signal acquired with PET and MRI produced strong negative correlation coefficients in both control (r=-0.85, p=0.35) and RIP1-Tag2 mice (r=-0.98, p=0.13) (Fig. 4.2.2a). In agreement with this outcome, the analysis of voxels

of produced negative coefficients for the pancreas of RIP1-Tag2 mice (*r*=-0.31) (Fig. 4.2.2b, c).

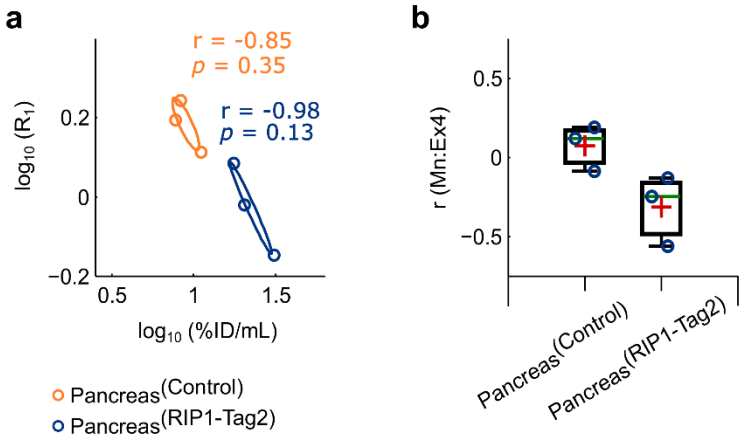

Fig. 4.2.2 Correlation analysis between PET and MRI measurements

(**a**) In the graph the medians of $\log_{10}$(%ID/mL) and $\log_{10}(R_1)$ are scattered to determine correlation between PET and MRI data. For the analysis, the Pearson's correlation coefficients (*r*) are displayed for the control (*r*=-0.85, *p*=0.35, dark orange) and transgenic RIP1-Tag2 mice (*r*=-0.98, *p*=0.13, dark blue). The ellipses reflect the respective variance of PET and MRI measurement. (**b**) The boxes show the interquartile range, the mean (red crosses) and median values (green line) of the *r* coefficients computed voxel-wise for the VOIs of control and RIP1-Tag2 mice. The length of whiskers is equal to 1.5 times the interquartile range of the 1st and the 3rd quartile. (**c**) Below are shown the voxels of the VOIs of RIP1-Tag2 mice scattered in the three dimensions and displaying the distribution of values for PET ($\log_{10}$(%ID/mL)) and MRI ($\log_{10}(R_1)$). The figures were adapted from the research article (Michelotti et al., 2020).

To support the data obtained from the *in vivo* measurements, the spatial distribution of the PET tracer and the contrast agent was investigated by *ex vivo* analysis of the entire pancreas sections, in both the groups of control and transgenic mice. From the autoradiography analysis, several hot-spots were identified throughout the pancreas sections as they showed high tissue contrast compared to the surrounding tissue in both the groups (Fig. 4.2.3a). The elemental images obtained through LA-ICP-MS imaging of the same autoradiography slides revealed the presence of high endogenous levels of ^{64}Zn and ^{44}Ca. Interestingly the high levels of metals were in excellent agreement with the distribution of the PET tracer targeting GLP-1R. By contrast, other reference metals, such as ^{13}C and ^{65}Cu, were homogenously distributed and did not merge with the accumulation of the PET tracer or the other metals (Fig. 4.2.3a).

Linear regression analysis revealed a positive linear relationship between the [^{64}Cu]Ex4 intensities and the spot dimensions calculated in control (R^2=0.86) and RIP1-Tag2 mice (R_2=0.45) (Fig. 4.2.3b, c). In comparison with the distribution of the PET tracer and the endogenous levels of ^{44}Ca and ^{64}Zn, the levels of ^{55}Mn were higher for the surrounding exocrine pancreas.

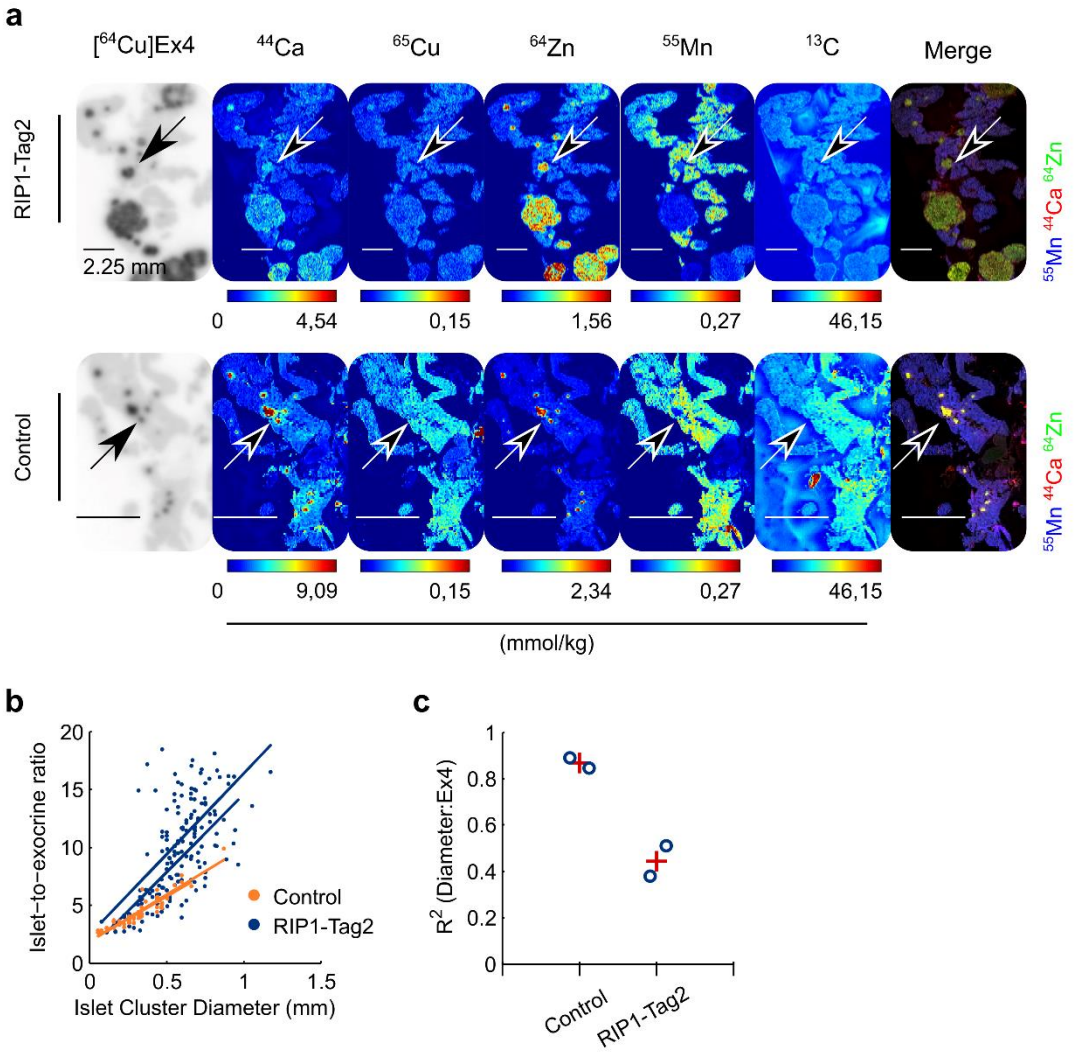

Fig. 4.2.3 Merged elemental imaging and autoradiography at an early time point (1 h)

(**a**) In the figure are shown the autoradiography of [^{64}Cu]Ex4 next to the elemental images of ^{44}Ca, ^{65}Cu, ^{64}Zn, ^{55}Mn and ^{13}C isotopes measured by LA-ICP-MS using the same slide. The black arrows indicate the identified spot-like pattern, which reflects the distribution of islet cell cluster and insulinomas throughout the pancreas section of control and RIP1-Tag2 mice, respectively. Merged elemental images of ^{55}Mn (blue channel), ^{44}Ca (red channel) and ^{64}Zn (green channel) indicate the low specific uptake of exogenous ^{55}Mn due to the high concentration found in the surrounding exocrine pancreas. Scale bars are set to 2.25 mm. (**b**) Linear regression analysis between the islet cell cluster diameter and [^{64}Cu]Ex4 uptake. (**c**) The calculated values of R^2 obtained from the linear fit as well as the mean values (red crosses) for each group are plotted. Images and graphs were adapted from the article (Michelotti et al., 2020).

4.2.2 Late Retention of Mn in Healthy Pancreatic Islet cells and Insulinomas

A group of control and RIP1-Tag2 mice were longitudinally measured with PET/MRI at 24 h post injection at an early (10 weeks) and a late tumor progression stage (13 weeks). Analysis of PET and MRI signal indicated slight differences between the groups (Fig. 4.2.4a, b). This outcome agreed with the correlation analysis of voxels and the mean values of VOIs, as it produced weak and not significant correlation coefficients (Fig. 4.2.4c, d).

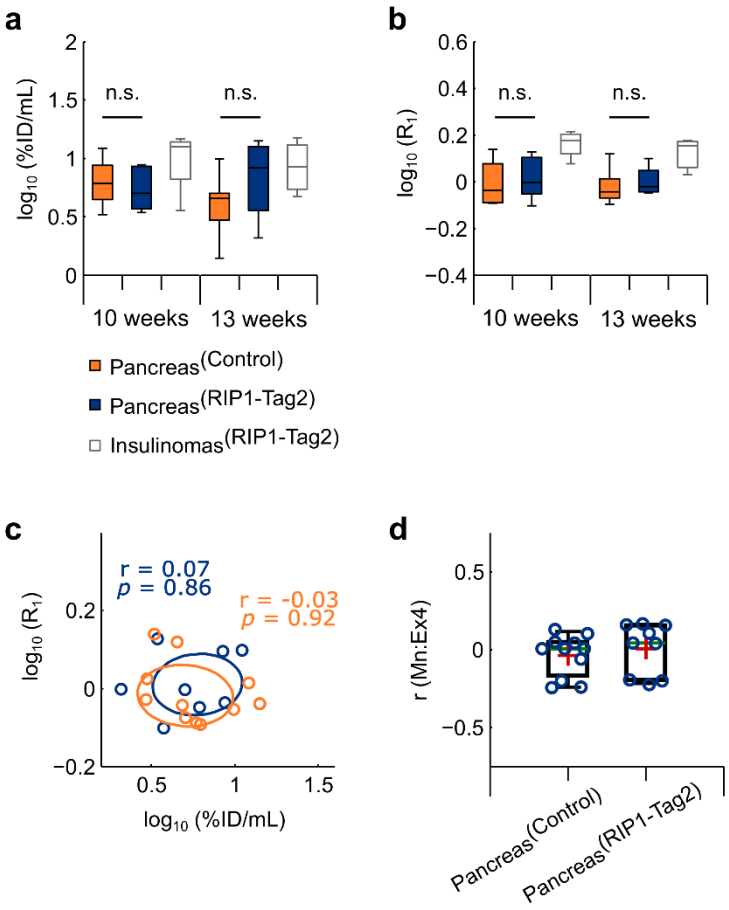

Fig. 4.2.4 Longitudinal PET/MRI acquired late time points

The boxes show the interquartile of (**a**) PET (log_{10}(%ID/mL)) and (**b**) MRI data ($log_{10}(R_1)$) acquired respectively at 10 and 13 weeks of age for the pancreas of control and RIP1-Tag2 mice. As reference are displayed the values calculated for the detected insulinomas of RIP1-Tag2 mice. The Pearson's correlation coefficients (*r*) are displayed for the mean values of the VOIs in control (dark orange) and transgenic RIP1-Tag2 mice (dark blue). The ellipses contour the variance of PET and MRI measures. The boxes depict the interquartile range of the *r* coefficients computed using the voxels of individual VOIs of pancreas in control and RIP1-Tag2 mice. The length of whiskers is equal to 1.5 times the interquartile range of the 1st and 3rd quartile. Differences between the control (Pancreas^{Control}) and transgenic mice (Pancreas$^{RIP1\text{-}Tag2}$) were

calculated by a two-sample Student's *t*-test and assuming unequal variance between the groups. The graphs were adapted from the research article (Michelotti et al., 2020).

At the last imaging session, *ex vivo* analysis was performed to determine the specific distribution of PET tracer and contrast agent. Therefore, autoradiography and ICP-MS measurements were performed for both groups. The autoradiography showed a spot-like pattern distribution of tracer throughout each pancreas section, suggesting that the radiopeptide was specifically internalized by the pancreatic islets. The regression analysis indicated a positive relationship between the spot dimensions and the quantified signal in both the group of control (R^2=0.7) and RIP1-Tag2 mice (R^2=0.4) (Fig. 4.2.5a-c).

In comparison with the first group of mice measured at earlier time points (1 h), several hot-spots at high levels of ^{55}Mn were localized throughout the pancreas sections, which also merged with the levels of endogenous ^{44}Ca and ^{64}Zn as well as with distribution of the PET tracer (Fig. 4.2.5a).

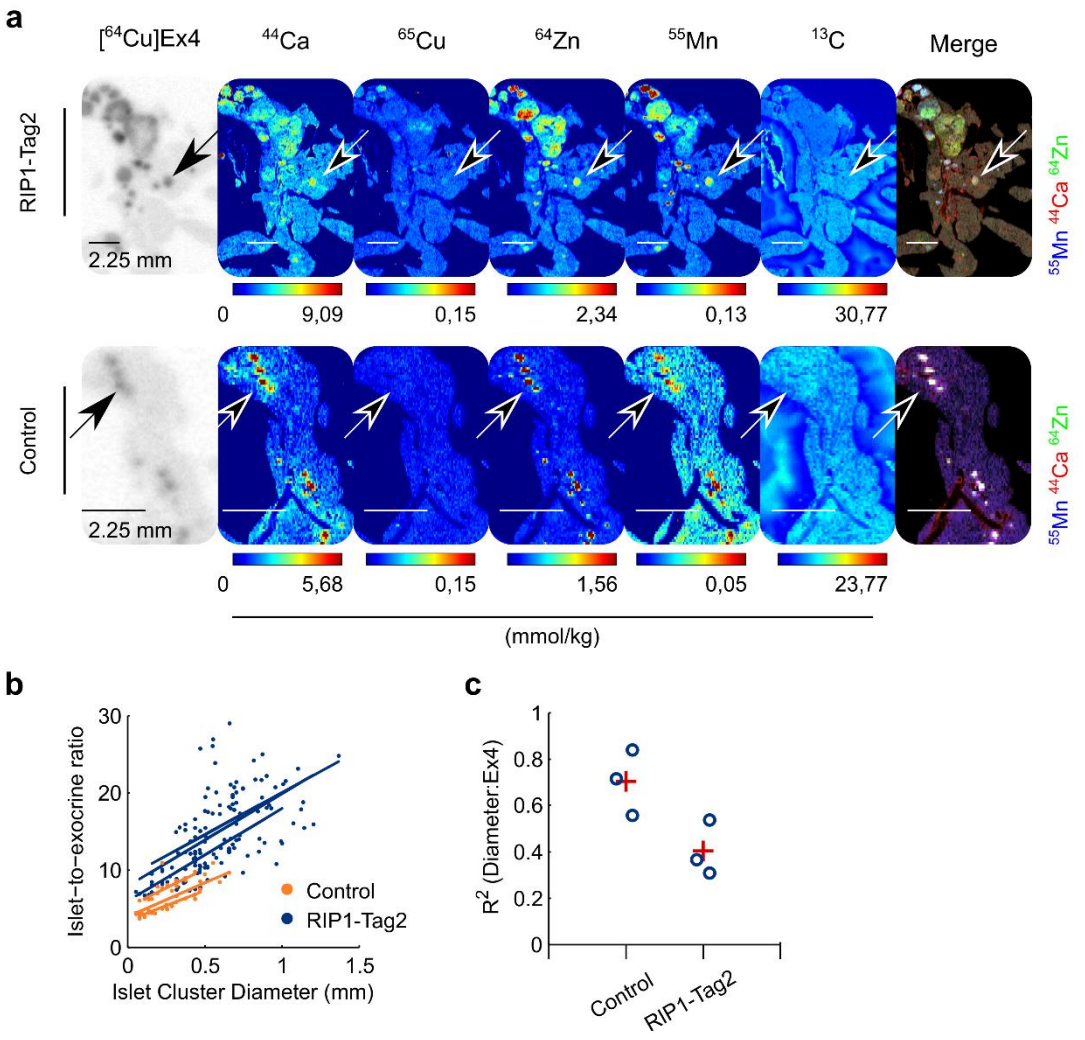

Fig. 4.2.5 The specificity of the late retention of Mn was confirmed by autoradiography of radiolabeled Ex4 and the distribution of endogenous biometals

(**a**) As described in Fig. 4.2.3, the figure depicts the distribution of radiolabeled Ex4, next to the elemental images of ^{44}Ca, ^{65}Cu, ^{64}Zn, ^{55}Mn and ^{13}C obtained from the same slide of pancreata of control and RIP1-Tag2 mice. Scale bar are set to 2.25 mm. The spotted areas at high tracer uptake and biometals levels are indicated with black arrows. (**b**) The values of spot dimension and tracer uptake (islet-to-exocrine ratio) are plotted and linear fit is shown for each analyzed mouse. (**c**) The single R^2 values and the respective mean values (red crosses) are plotted for each group. The figures and the graphs were adapted from the research article (Michelotti et al., 2020).

4.2.3 *In Vivo* Follow-up of Mn and Radiolabeled Ex4 uptake by Repeated PET/MRI measurements at Early and Late Time Points

As Mn has been specifically localized in the endocrine pancreas when the pancreata were analyzed *ex vivo* 24 h after Mn injection, a third group of mice were measured with PET/MRI at both early (1 h) and late time points (24 h) after

the co-injection of the PET tracer and contrast agent. As is shown in Fig. 4.2.6a, a higher PET tracer uptake was observed in transgenic mice that were measured at 1 h (t(9.94)=2.66, *p=0.02) and 24 h after the tracer injection (t(16.26)=5.89, p<0.001). By contrast, the R_1 values were significantly higher in the control group compared to the pancreata of transgenic mice (t(9.63)=-3.44, p<0.01 and Table 4.2.1). The analysis of the variance between PET and MRI produced negative correlation coefficients for the pancreata of control (r=-0.73, p=0.27) and transgenic RIP1-Tag2 mice (r=-0.71, p=0.05) (Fig. 4.2.6c). Only slight differences were observed between the groups measured at late time points (t(6.89)=-0.78, p=0.47).

However, the correlation analysis produced moderated positive coefficients in healthy and transgenic mice, with Pearson's r values equal to 0.69 and 0.50, respectively (Fig. 4.2.6d). In Fig. 4.2.6e, representative PET/MR images show the distribution of PET and T_1 values in the pancreas of RIP1-Tag2 mice measured at late time points (24 h).

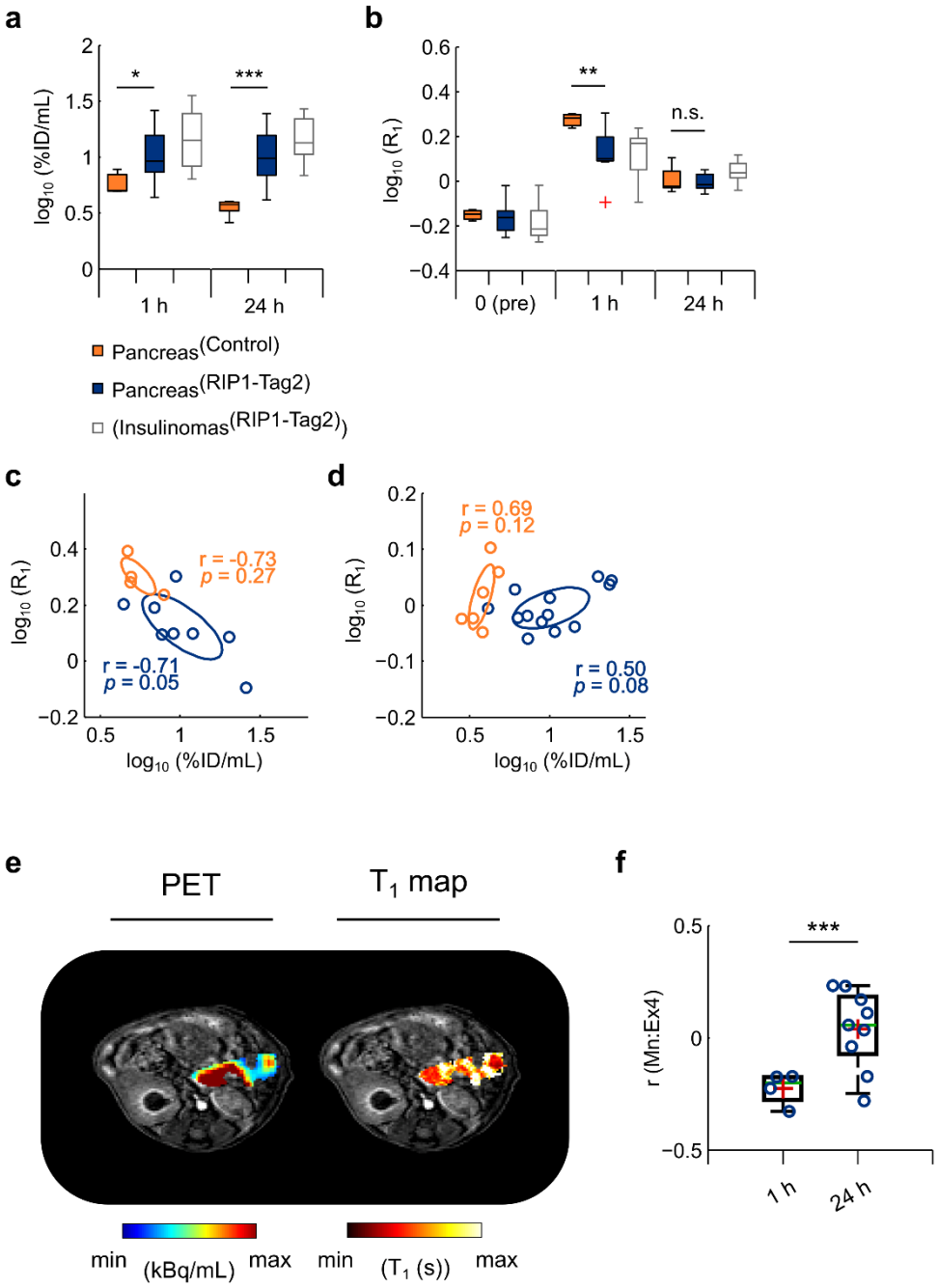

Fig. 4.2.6 Shift in correlation coefficients of PET/MRI between early and late time points

The boxes show the interquartile range distribution of (**a**) PET (log_{10}(%ID/mL)) and (**b**) MRI data ($log_{10}(R_1)$) of mice measured at 1 h and 24 h; the outliers are indicated with the red crosses and consists of values higher than 1.5 times the interquartile range above and below the 1st and the 3rd quartile and delimited by the whiskers. (**c**) Mean values of PET and MRI data acquired at 1 h are plotted and the Pearson's correlation coefficients (*r*) displayed for control (*r*=-0.73, *p*=0.27) and RIP1-Tag2 mice (*r*=-0.71, *p*=0.05). (**d**) Correlation analysis of mean values measured at 24 h are displayed for the control (*r*=0.69, *p*=0.12) and RIP1-Tag2 group (*r*=0.50, *p*=0.08). (**e**) Representative PET and T_1 maps are overlaid on the anatomical MR image centered in the pancreas of RIP1-Tag2 mice. Differences between the group of 10 to 15-week-old control ($Pancreas^{Control}$) and aged-matched RIP1-Tag2 mice ($Pancreas^{RIP1\text{-}Tag2}$) were calculated using a two-sample Student's *t*-test. (**f**) The boxes show the interquartile range, the mean and the median values of Pearson *r*

coefficients between PET/MR images of the pancreas of RIP1-Tag2 mice acquired at 1 h and 24 h. The length of whiskers is equal to 1.5 times the interquartile range of the 1st and 3rd quartile. Differences in the coefficients was computed by a two-sample Student's *t*-test ($t(11.0)=4.55$, ***$p<0.001$). The graphs were adapted from the research article (Michelotti et al., 2020).

Interestingly, significant differences were found between the correlation coefficients of mice measured either at early or late time points ($t(11.0)=4.55$, $p<0.001$) (Fig. 4.2.7f).

Table 4.2.1 PET/MRI quantification of pancreas at 1 h and 24 h post injection

Longitudinal quantification of healthy pancreas and insulinomas

	PET		MRI		
	$\log_{10}$ (%ID/mL)		$\log_{10}$ (R_1)×10^1		
VOIs	1 h	24 h	Pre	1 h	24 h
$Pancreas^{Control}$	0.7±0.1	0.6±0.1	-1.5±0.3	3.0±0.7	0.1±0.6
$Pancreas^{10\text{-}15week\text{-}old}$	1.0±0.3	1.0±0.2	-1.6±0.7	1.2±1.1	-0.1±0.4
$Insulinomas^{10\text{-}15\text{-}week\text{-}old}$	1.2±0.3	1.2±0.2	-1.8±0.9	1.2±1.2	0.4±0.5

4.2.4 *Ex Vivo* Distribution of Mn and radiolabeled Ex4 within the Pancreas of Mice at Basal Glucose Condition

To validate the specificity of Mn for the pancreatic islets, further investigations were performed to evaluate whether glucose stimulation might influence the distribution of the PET tracer and the contrast agent between the exocrine and the endocrine pancreas. In this regard, separated cohorts of control and RIP1-Tag2 mice were injected with the PET tracer and $MnCl_2$ without the following stimulation with glucose.

The distribution of PET tracer was comparable with the other group of mice which have been treated with glucose. The analysis of elemental images indicated that the levels of ^{55}Mn were higher in the surrounding exocrine pancreas than in the hot-spots areas, which were characterized by increased levels of radiolabeled Ex4 and ^{64}Zn (Fig. 4.2.7). As observed in the previous experiments, where the mice that were treated with glucose and assessed at later time points, the levels of ^{55}Mn showed hot-spot pattern throughout the entire pancreas sections,

reflecting the distribution of the endocrine pancreas. Furthermore, the analysis show high levels of [^{64}Cu]Ex4 and ^{64}Zn suggesting the presence of islet cells with high levels of insulin-zinc complexes and GLP-1R expression. Altogether those results suggested that the early and late distribution of Mn was not affected by the initial treatment of mice with glucose.

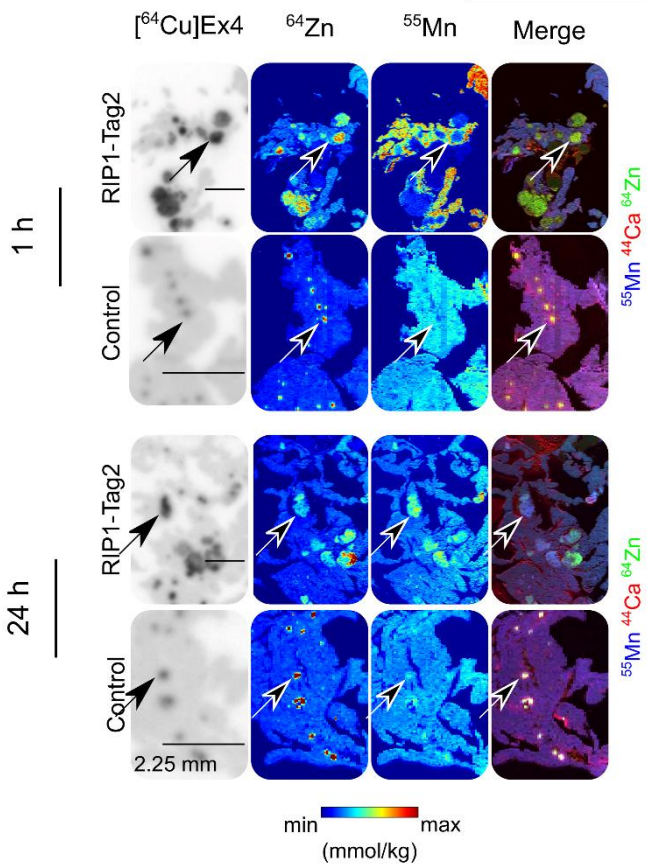

Fig. 4.2.7 Differences in the early and late distribution of ^{55}Mn without the stimulation with high glucose concentrations

The figure depicts the autoradiography of [^{64}Cu]Ex4 of sections obtained from the pancreas of control and RIP1-Tag2 mice. Next to the autoradiography are displayed the elemental images of ^{64}Zn and ^{55}Mn isotopes and the merged elemental images of ^{44}Ca (red channel), ^{64}Zn (green channel) and ^{55}Mn (blue channel) measured using the same slide. The black arrows indicate the diffuse hot-spot identified throughout the section with increased accumulation of PET tracer and the high endogenous levels of ^{64}Zn. The figures were adapted from the research article (Michelotti et al., 2020).

4.2.5 Glucose-dependent Insulin Secretion Response

The blood glucose levels monitored in control and RIP1-Tag2 mice (n=4/4) showed a ~60% decrease between 9 and 13 weeks of age with percentages significantly lower compared to the healthy mice (Z=2.16, **p*=0.03).

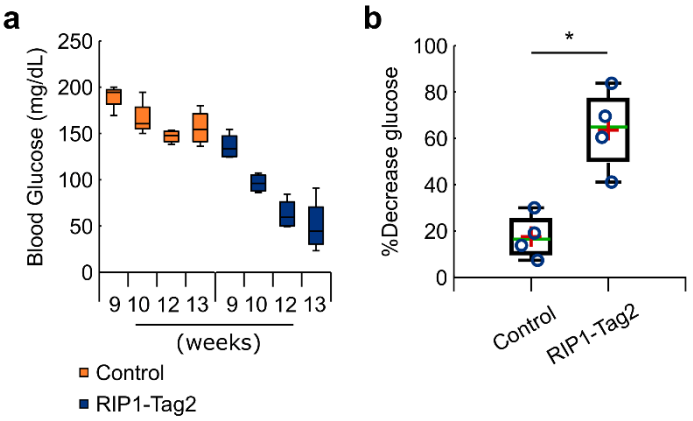

Fig. 4.2.8 Progressive decrease of blood glucose levels of transgenic RIP1-Tag2 mice

The figure adapted from the research article (Michelotti et al., 2020) show (**a**) the boxes show the interquartile range of blood glucose levels (mg/dL) measured overtime during the progression of insulinomas between 9 and 13 weeks of age. (**b**) The boxplots show the interquartile range, the mean values (red crosses) and the medians (green line) of the percentage decrease in the blood glucose concentration between 9 and 13 weeks in aged-matched control and RIP1-Tag2 mice (Z=2.16, **p*=0.03). Differences between the groups are calculated by a nonparametric Rank Sum Wilcoxon's test.

Due to the potential toxic effect of Mn on the viability of cells, the physiological capacity of isolated islet cells to secrete insulin was tested at 1 h and 24 h, respectively, after the injection of Mn-based contrast agent. The analysis of islet cells of 8-week-old mice showed increased levels of insulin at stimulating glucose concentration condition in both the groups, with values that were 10 to 20 times higher than when they were incubated at basal glucose concentration (Fig. 4.2.9a-c).

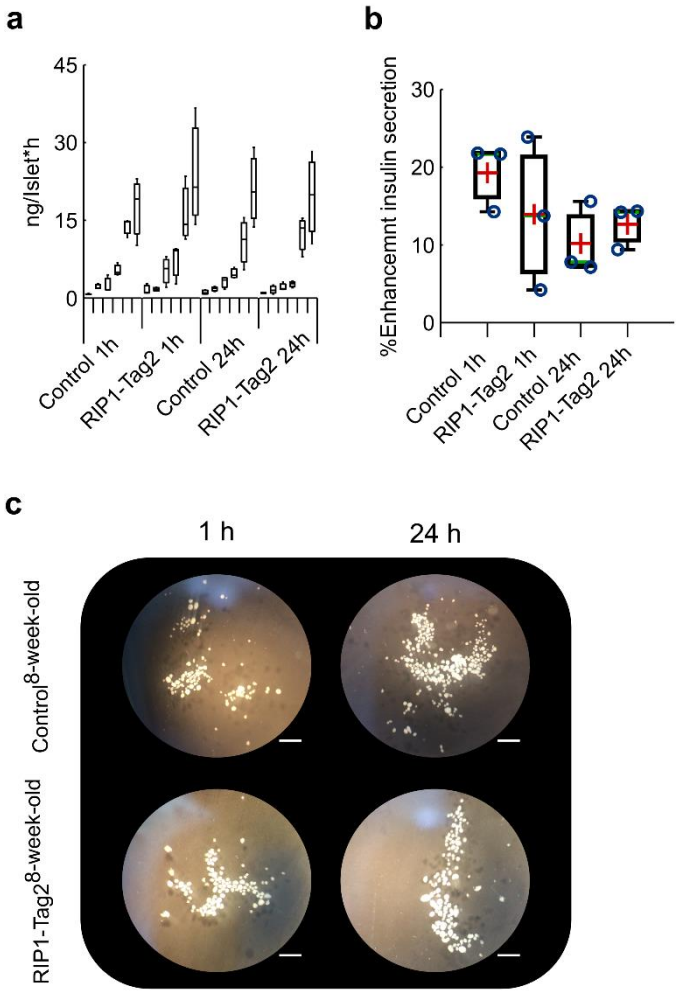

Fig. 4.2.9 Insulin secretion response at 1 h and 24 h post injection

(**a**) The boxes depict the interquartile range of insulin concentration (ng/Islet*h) measured at different glucose conditions (3, 6, 8, 10, 15 and 30 mM). (**b**) The boxes show the interquartile range, the mean (red crosses) and the median values (green line) of the percentage of the enhancement of insulin secretion calculated between basal (3 mM) and the stimulating glucose conditions (15 mM). In the figure are displayed islets isolated from (**c**) the groups of 8-week-old control and RIP1-Tag2 mice observed under the optical microscope with lens magnification 40x. Scale bars are set to 2.25 mm.

However only slight differences were measured between the insulin response to glucose of islets isolated at 1 h and 24 h, suggesting that the presence of high levels of Mn at 1 h did not affected the physiology of islets to secrete insulin. Instead, a lower enhancement of insulin response was monitored from the islets isolated from 13-week-old RIP1-Tag2 mice, which is related the high levels of insulin measured at low glucose concentrations (Fig. 4.2.10a-c).

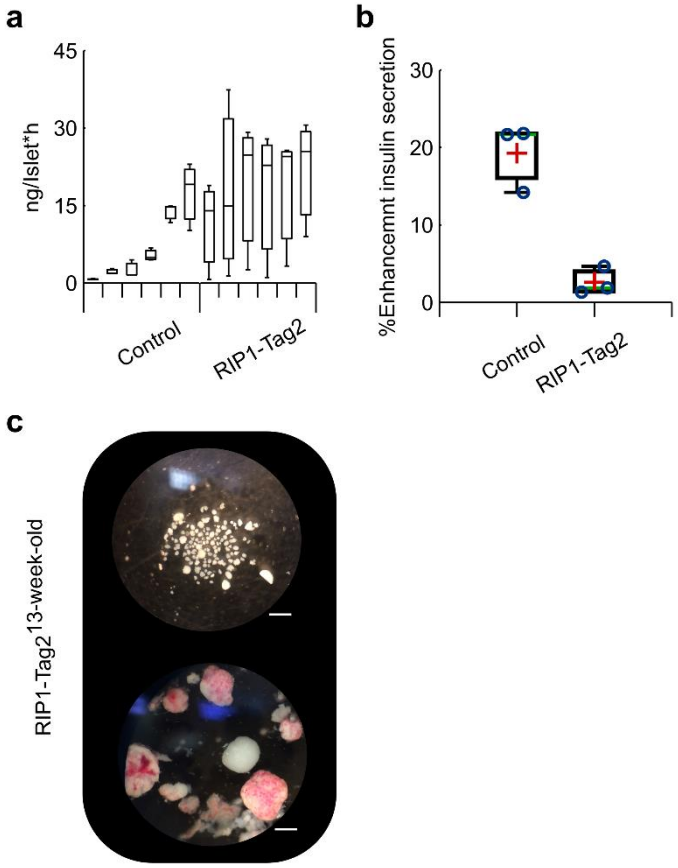

Fig. 4.2.10 Impaired insulin secretion response at late tumor progression

(**a**) Glucose-dependent insulin secretion assay and (**b**) quantification of the enhancement of insulin secretion of islets isolated from 13-week-old control and RIP1-Tag2 mice 1 h after the injection of contrast agent. (**c**) The figure depicts the distribution of assayed islet cells and the solid large tumors excluded from the analysis of 13-week old RIP1-Tag2 mice under the optical microscope with lens magnification 40x. Scale bars are set to 2.25 mm.

4.3 Monitoring of Islet Cell Engraftment by PET/MRI

4.3.1 Longitudinal Evaluation of the Islet Cell Engraftment

In a first pilot group, monitoring of islet cells was performed longitudinally at 1, 3 and 4 weeks after the inoculation of cells into the calf of the leg of recipient C3H mice. The analysis of co-registered PET/MR showed a slight increase in the uptake of tracer ($t(2.0)=0.61$, $p=0.60$) and the R_1 values ($t(2.0)=4.02$, $p=0.06$) calculated between one and three weeks after transplantation (Fig. 4.3.1a, b). PET using radiolabeled Ex4 could detect the hot-spots areas within the calf of the transplanted leg (Fig. 4.3.1c).

At the same time, combined ME-MR images at high contrast and anatomical resolution enabled the visualization of the anatomical contours between the transplanted islets and the surrounding tissues, such as muscle and bone.

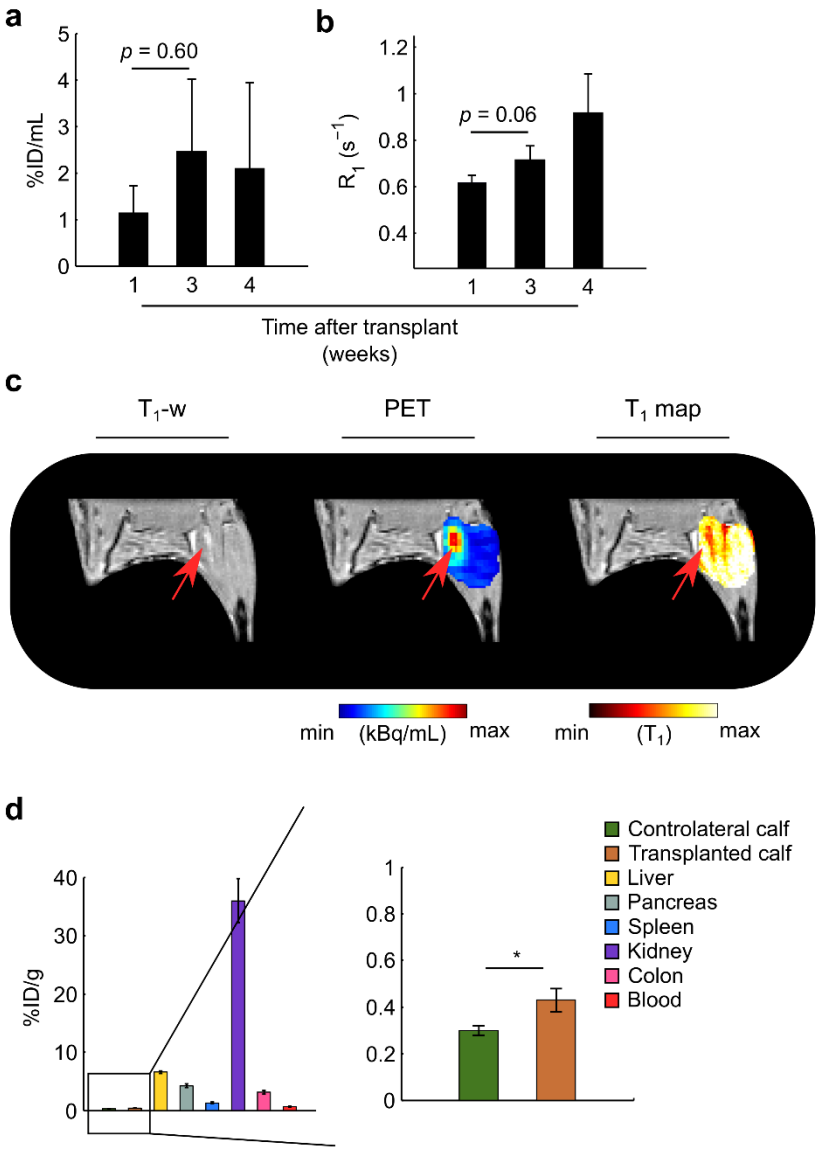

Fig. 4.3.1 Longitudinal PET/MR between 1 and 3 weeks after transplantation

The bar plots show the mean values ± SD of (**a**) %ID/mL and the (**b**) R_1, reflecting [^{64}Cu]Ex4 and Mn uptake, respectively. Differences overtime of each individual mouse were calculated between 1 and 3 weeks by one-sample Student's *t*-test. (**c**) Co-registered PET/MR images are representative of the specific accumulation of radiolabeled Ex4 in the transplanted islets. T_1-w images and the overlaid T_1 values show anatomical burden of islet transplant. (**d**) *Ex vivo* biodistribution and comparison of the PET tracer uptake between the contralateral and transplanted leg was tested for statistical significance by one-sample Student's *t*-test.

The analysis of the *ex vivo* biodistribution confirmed the *in vivo* measurements since the analysis of PET resulted in the quantification of uptake values significantly higher for the transplanted calf compared to the contralateral leg of the mice ($t(2.0)=7.83$, $^*p=0.02$) (Fig. 4.3.1d).

4.3.2 Blocking of VDCC Activity of Islet Transplant

In order to investigate whether the uptake of Mn was specific for the VDCC activity of engrafted islets, a group of transplanted mice was treated with a Ca^{2+}-blocker seven minutes before the injection of the tracer and contrast agent.

The analysis of the PET images indicated slight differences in the %ID/mL between the control group and the mice pre-treated with diazoxide (23 mg/kg) ($t(3.9)=0.3$, $p=0.75$). Similarly, the R_1 values measured from the islet cells localized in the calf pre-treated mice were only slightly lower compared to the control group ($t(-1.0)=3.1$, $p=0.39$) (Fig. 4.3.2a, b).

Ex vivo analysis of the calf and the pancreata of mice, including autoradiography and LA-ICP-MS imaging, were performed after the imaging session to corroborate the *in vivo* results. From the analysis of ^{44}Ca and ^{64}Zn, a clear hot-spot was detected within the muscle sections of the transplanted legs. By contrast, the distributions of ^{13}C and ^{65}Cu levels were homogeneous throughout each section and in both the groups of mice. Altogether, those results suggested that the engrafted islet cells were viable due to the high levels of endogenous divalent cations and GLP-1R expression. Furthermore, the same tissues areas analyzed by autoradiography showed ratio values equal to 62.6±35.7 and 21.6±0.9 times higher than the surrounding muscle tissue in control and treated mice, respectively (Fig. 4.3.2c). Linear regression analysis indicated a positive linear relationship ($R^2=0.83$) between the islet size and the calculated ratios (Fig. 4.3.2d).

In principle, the group of mice treated with a Ca^{2+}-blocker were expected to show lower levels of ^{55}Mn and ^{44}Ca. However the accumulation of Mn was similar in

both groups of mice, suggesting that the effect of a single dose of Ca^{2+} did not affect the diffusion of Mn into the intracellular space of engrafted islet cells.

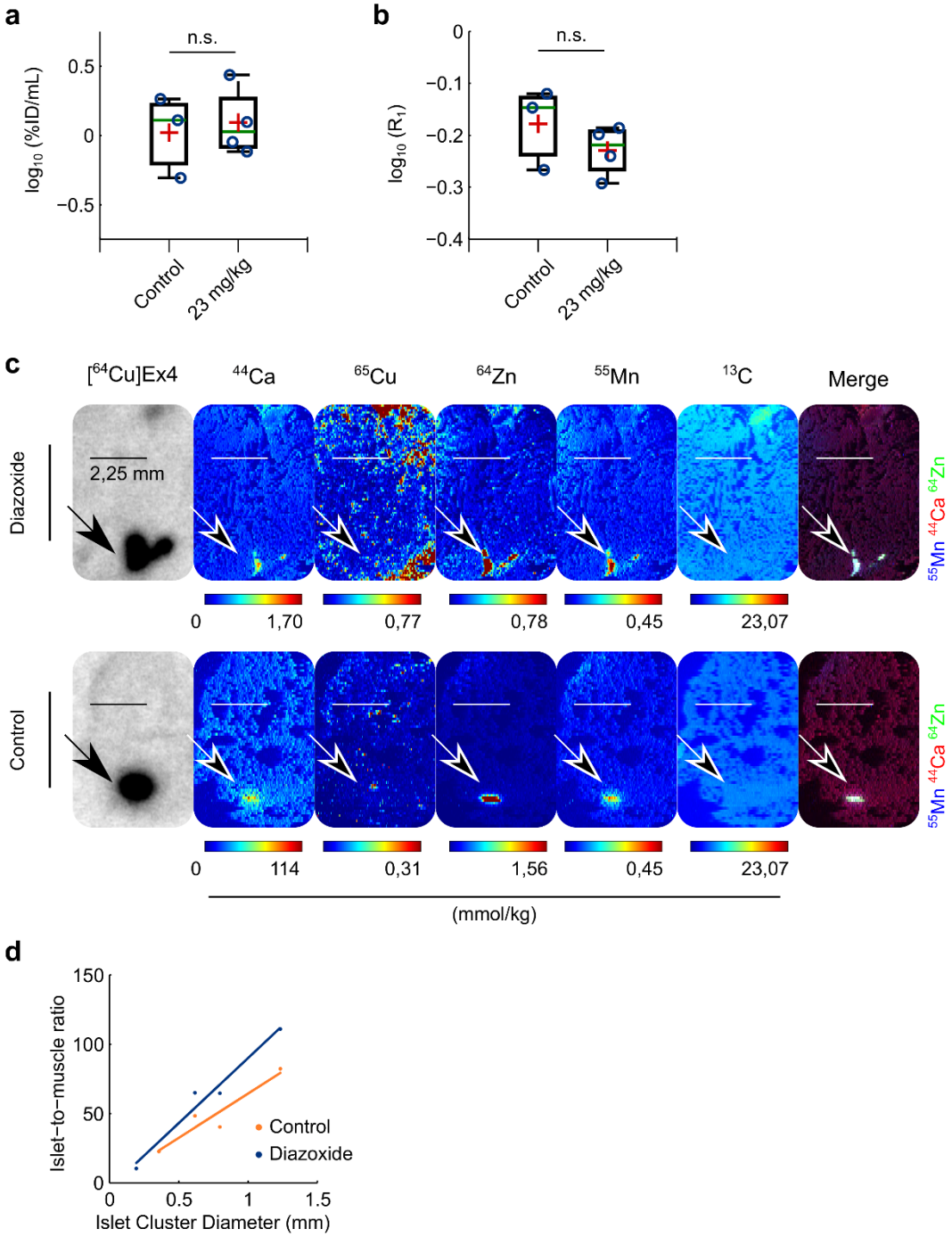

Fig. 4.3.2 PET/MRI quantification and *ex vivo* analysis revealed accumulation of probes in the transplanted calf

The boxes show the 1st, 2nd (green line) and the 3rd quartile and the mean values (red crosses) of (**a**) the medians log_{10}(%ID/mL) and (**b**) $log_{10}(R_1)$ calculated from the islets localized in the calf of control and diazoxide group. Differences in PET (t(3.9)=0.3, p=0.75) and quantitative maps of T_1 (t(-1.0)=3.1, p=0.39) between control and the treated group are calculated by a two-sample Student's t-test. (**c**) The black arrows

indicate the single-spots at high signal-to-background localized in the calf sections (dark spot) and with high levels of ^{44}Ca and ^{64}Zn compared to ^{13}C and ^{65}Cu, which were homogenous throughout the calf sections. Scale bar are set to 2.25 mm. Merged elemental images show the co-localization of endogenous metals and exogenous ^{55}Mn (white spot) in both control and treated mice. (**d**) Linear regression analysis tested the relationship between the diameter of islet implants and the [^{64}Cu]Ex4 uptake quantified by autoradiography.

Further investigations were performed on the pancreas sections to determine whether the accumulation of the PET tracer and Mn-based contrast agent was affected by the treatment with diazoxide. In agreement with the autoradiography of muscle sections several hot-spots were identified heterogeneously diffused throughout the pancreas sections (Fig. 4.3.3a). The spotted areas showed ratio values equal to 3.5±0.8 and 2.5±0.3 times higher than the surrounding exocrine pancreas in control and diazoxide-treated mice, respectively. The ratio values were strongly and positively related with the spot-size, with R^2 values equal to 0.8±0.1 and 0.7±0.2 for control and treated mice, respectively (Fig. 4.3.3b).

In contrast with the analysis of the muscle, the elemental images of ^{55}Mn revealed levels of ^{55}Mn that were higher in the surrounding exocrine pancreas compared to the endogenous levels of ^{44}Ca and ^{64}Zn (Fig. 4.3.3a). As observed from the analysis *in vivo*, there were no clear differences in the distribution of ^{55}Mn between the groups.

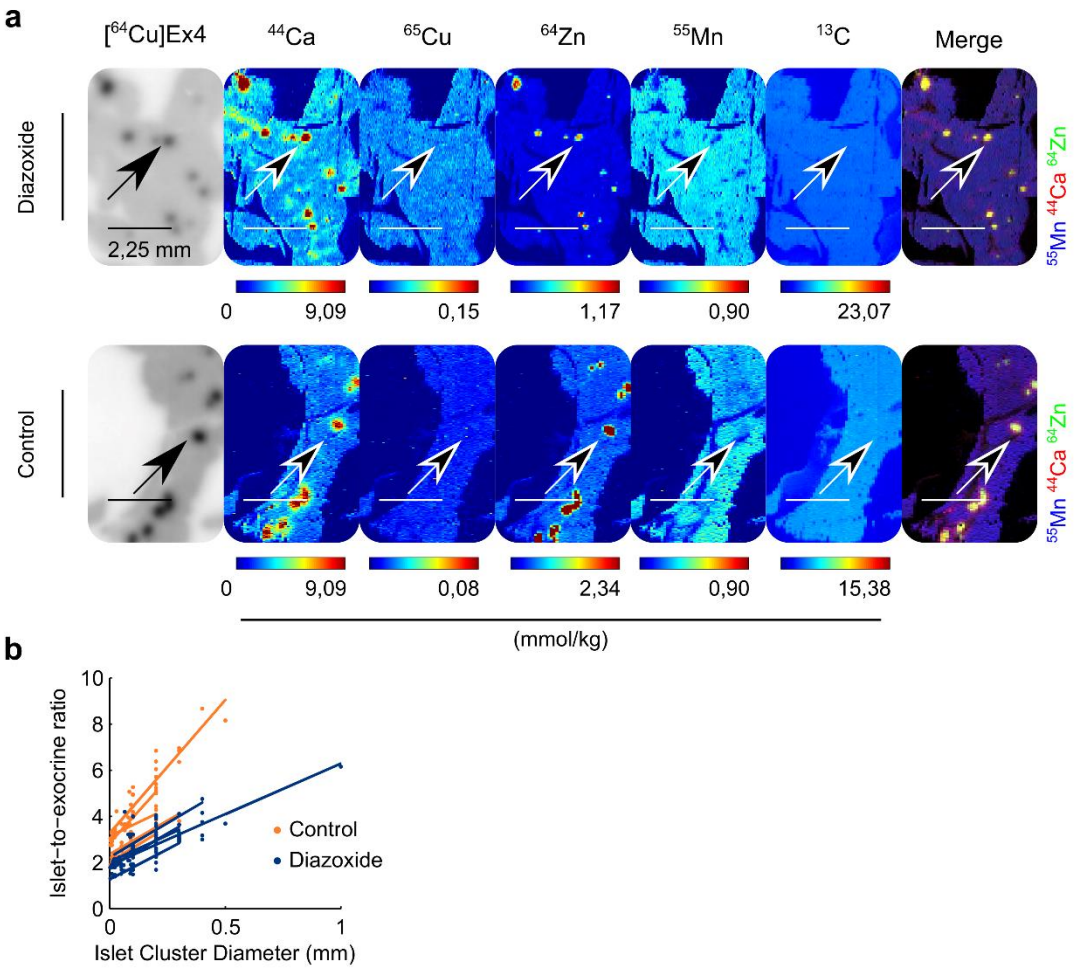

Fig. 4.3.3 *Ex vivo* analysis of pancreas revealed unspecific accumulation of exogenous ^{55}Mn in the exocrine pancreas

(**a**) The black arrows indicate the diffuse hot-spots at high levels of ^{44}Ca and ^{64}Zn and the accumulation of PET tracer (dark spots) throughout the pancreas sections of control and mice pre-treated with diazoxide. Scale bar are set to 2.25 mm. Merged elemental images show the specific co-localization of ^{44}Ca and ^{64}Zn (yellow spots), compared to the high accumulation of ^{55}Mn in the surrounding exocrine areas throughout the pancreas sections. (**b**) Regression analysis show the positive relationship between the [^{64}Cu]Ex4 uptake quantified by autoradiography and the diameter of pancreatic islets localized in each pancreas section.

4.4 Radioactive ^{52}Mn as Potential Dual PET/MRI Agent to Measure the Endocrine Pancreas

Differences in the early kinetic of tracers were assessed through the acquisition of dynamic (0-1 h) PET scans of mice treated either with $^{52}MnCl_2$ or ^{52}MnDPDP. A separated group of mice was pre-treated with a Ca^{2+}-blocker 2 min before the bolus i.v. injection of ^{52}MnDPDP.

4.4.1 Dynamic ^{52}Mn PET using either ^{52}MnDPDP or $^{52}MnCl_2$

The early uptake curves showed a stable accumulation of radioactive ^{52}Mn in the pancreas already after few minutes and until 1 h after the bolus injections. The comparison analysis of the tracer in the liver, pancreas and renal cortex showed only slight differences between the groups (Fig. 4.4.2a-d).

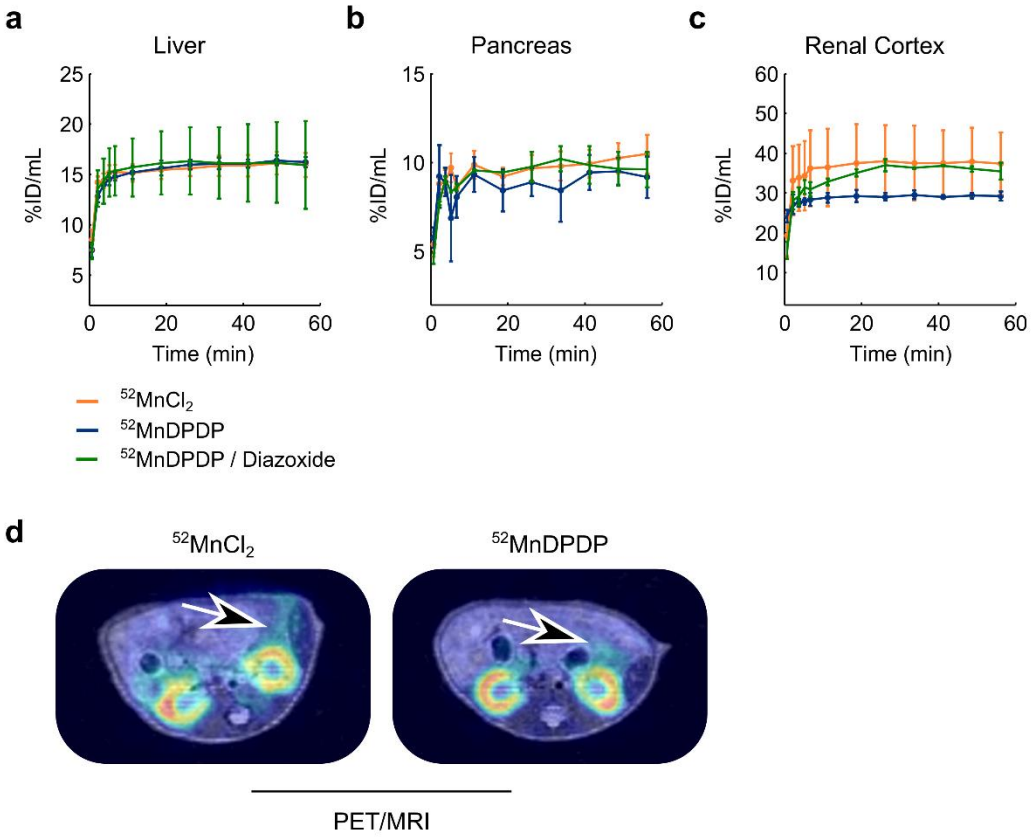

Fig. 4.4.1 Quantification of dynamic (0-1 h) ^{52}Mn PET in the abdomen

The dynamic PET tracer uptake curves show the mean values ± SD (%ID/mL) reflecting the accumulation of $^{52}MnCl_2$ or ^{52}MnDPDP in the following tissues of interest: (**a**) liver, (**b**) pancreas, (**c**) renal cortex. Differences in the %ID/mL were calculated between the groups of mice treated with $^{52}MnCl_2$, ^{52}MnDPDP or diazoxide before the administration of ^{52}MnDPDP by using a pairwise comparison Tukey's *HSD* test. (**d**) In

the figure is shown a representative axial PET images that was co-registered with the anatomical MR images. The black arrows indicate the accumulation of radioactive ^{52}Mn in the pancreas.

On the other hand, the accumulation of ^{52}Mn in the heart (***p<0.01) and in other regions in the brain, such as the pituitary gland (*p=0.02) and the olfactory bulbs (*p=0.04), was significantly lower in the group of mice that were injected with ^{52}MnDPDP compared to the same radioactive dose of $^{52}MnCl_2$ (~3.7 MBq) (Fig. 4.4.2a-d).

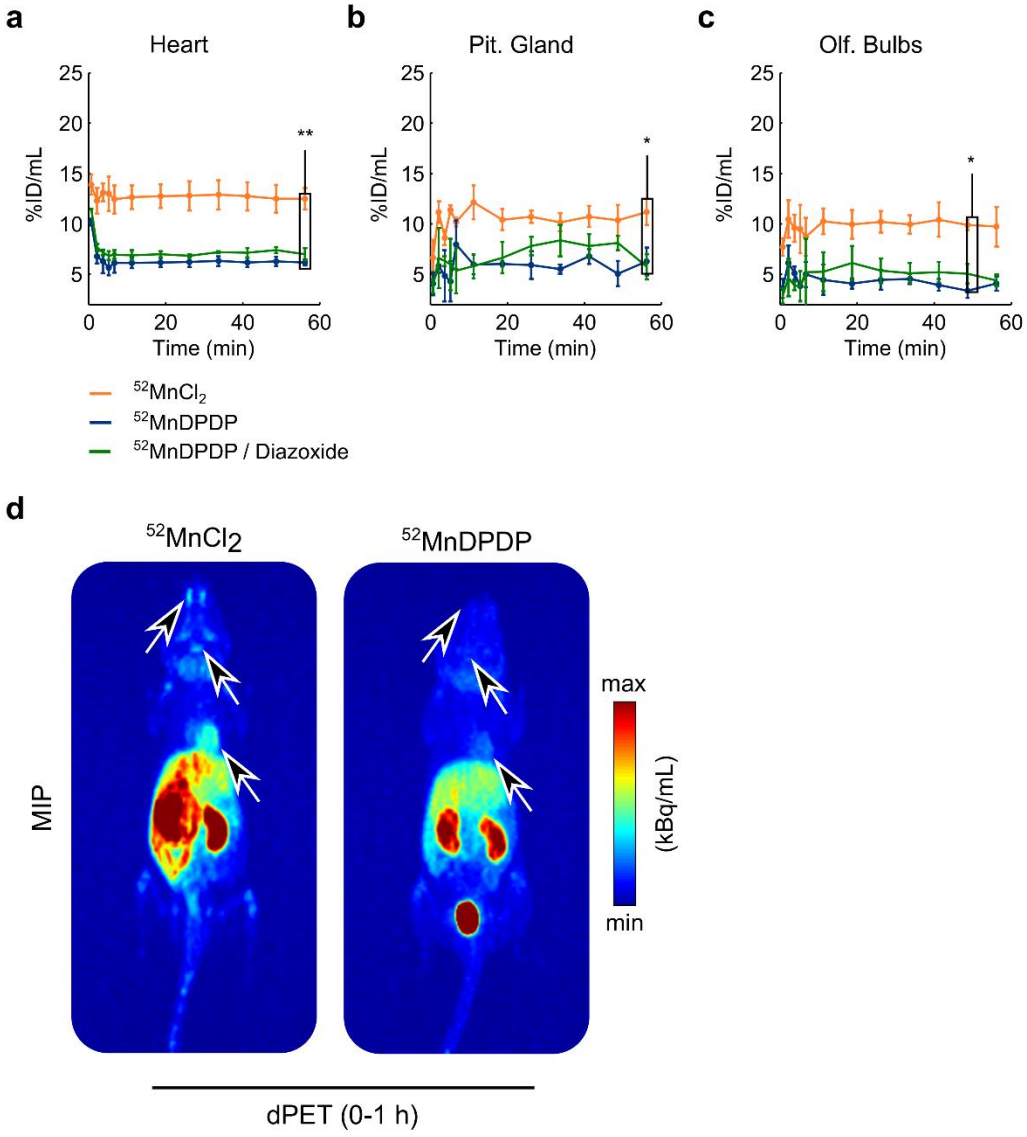

Fig. 4.4.2 ^{52}Mn PET in brain and heart

The tracer uptake curves show the mean values ± SD (%ID/mL) reflecting the accumulation of $^{52}MnCl_2$ or ^{52}MnDPDP in (**a**) heart and specific hotspots in the brain region such as the (**b**) pituitary gland and (**c**) the olfactory bulbs. Differences in the %ID/mL were calculated using a pairwise comparison Tukey's *HSD* test.

(**d**) The representative maximum intensity projections (MIP) show the difference in the signal measured in heart and brain (black arrows).

A lower accumulation of ^{52}Mn was also found in the heart and the brain regions of mice which were treated with the Ca^{2+}-blocker a few minutes prior to the administration of ^{52}MnDPDP. However, only statistical non-significant differences were observed with the group that was solely injected with ^{52}MnDPDP.

As is shown in Fig. 4.4.1, the maximal intensity projections of PET images showed a lower accumulation of radioactive ^{52}Mn in heart, brain and bladder in the group of mice injected with ^{52}MnDPDP.

4.4.2 Follow-up of ^{52}Mn Retention at Late Time Points

By monitoring of the PET tracers until later time points (72 h), it has been shown an overtime decrease of the signal, which is probably due to the wash-out of ^{52}Mn from the tissues of interest. In this regard, strong reduced signals were observed in the liver, renal cortex and heart (Fig. 4.4.3a, c and d and Table 4.4.1) in comparison with the other tissues, including the pancreas and the brain, where we observed an overall retention of the tracer in both the groups of mice until 72 h.

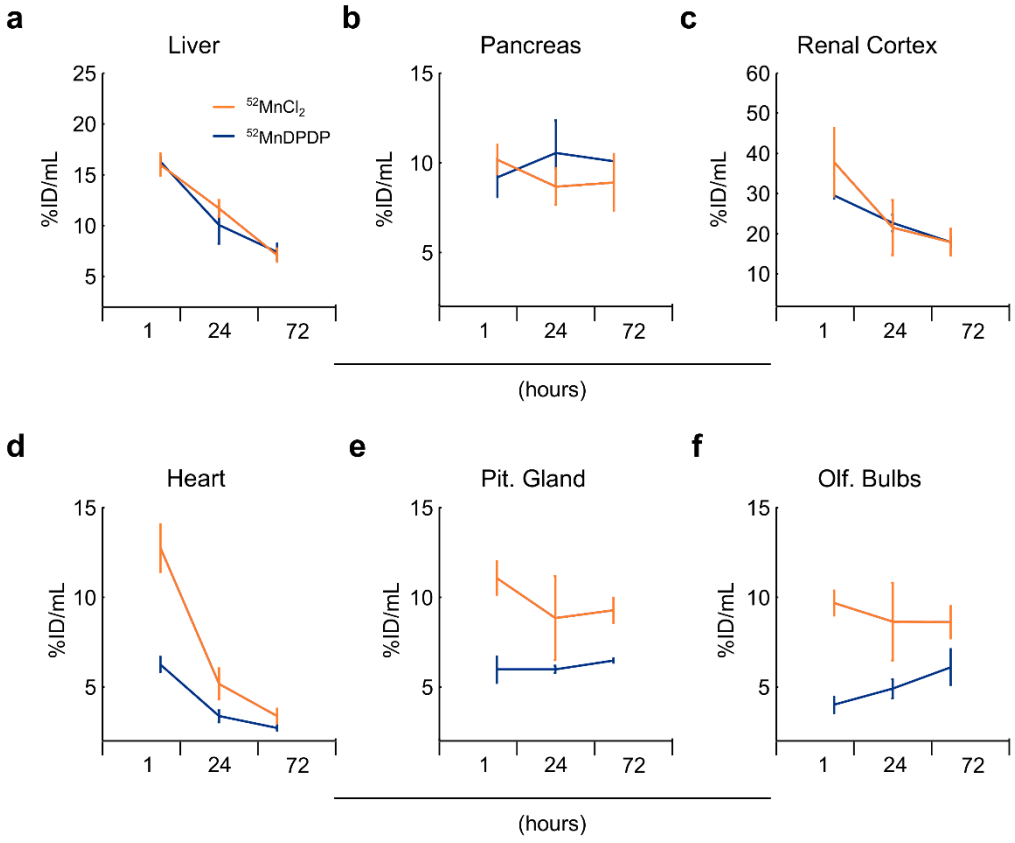

Fig. 4.4.3 Wash-out and retention of ^{52}Mn after $^{52}MnCl_2$ or $^{52}MnDPDP$ injection

The dynamic uptake curves display the mean values ± SD the %ID/mL in (**a**) the liver, (**b**) pancreas, (**c**) renal cortex, (**d**) the heart, and specific brain region like the (**e**) pituitary gland and (**f**) the olfactory bulbs. An overtime decrease of signal is observed in the liver, renal cortex and heart, compared to the region of brain and pancreas showing a stable retention of ^{52}Mn.

Table 4.4.1 Tissue uptake of ^{52}Mn measured overtime by PET

^{52}Mn tissue uptake measured *in vivo* overtime

	$^{52}MnCl_2$			$^{52}MnDPDP$		
Time point	1 h	24 h	72 h	1 h	24 h	72 h
Liver	16.0±1.1	11.7±0.8	7.1±0.7	16.3±0.5	10.0±1.8	7.4±0.8
Pancreas	10.2±0.8	8.7±1.0	8.9±1.6	9.2±1.1	10.5±1.8	10.1±0.1
Renal cortex	37.8±8.5	21.5±6.8	17.9±3.3	29.5±0.7	22.7±2.1	17.9±1.4
Heart	12.7±1.3	5.2±0.9	3.4±0.4	6.2±0.4	3.4±0.3	2.7±0.1
Pit. gland	11.0±0.9	8.8±2.4	9.2±0.7	5.9±0.7	5.9±0.2	6.4±0.1
Olf. bulbs	9.7±0.7	8.6±2.2	8.6±0.9	4.0±0.5	4.9±0.5	6.1±1.0

The ratio calculated between 1 h and 24 h, heart (t(2.12)=-11.80, ***p<0.01) and renal cortex (t(3.82)=-6.20, ***p<0.01) were significantly lower in the group of mice injected with ^{52}MnDPDP (Fig. 4.4.4), which can be due to the stronger wash-out of ^{52}Mn from those tissues in the animals that were treated with $^{52}MnCl_2$. By contrast, only slight differences were observed in the pancreas (t(2.86)=-2.35, p=0.10) and the other tissues between the groups.

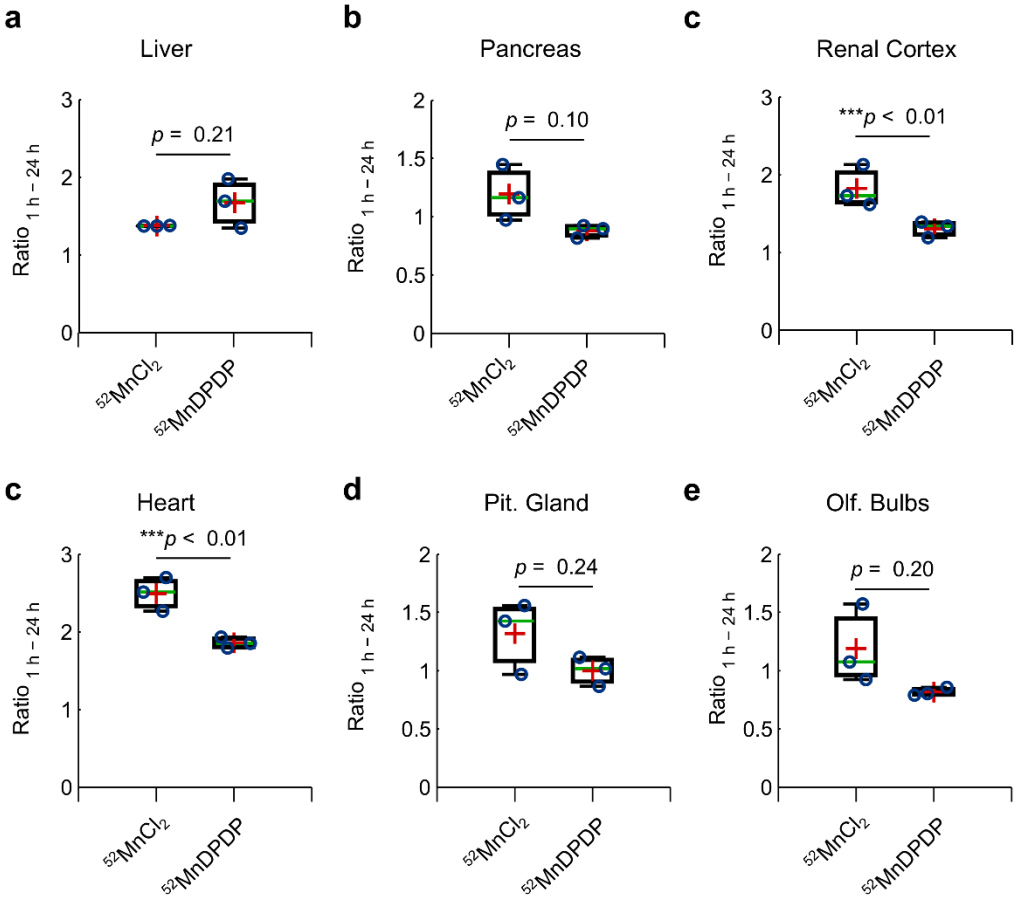

Fig. 4.4.4 Overtime retention of $^{52}MnCl_2$ and ^{52}MnDPDP

The boxes show interquartile range, the mean (red crosses) and the median values (green line) of the ratio calculated between the PET measurements performed at early and late time points (ratio$_{1\,h\,-\,24\,h}$). Differences between the groups in the ratios of (**a**) the liver, (**b**) pancreas, (**c**) renal cortex, (**d**) the heart, and specific brain region like the (**e**) pituitary gland and (**f**) the olfactory bulbs were calculated by a two-sample Student's *t*-test.

The biodistribution studies and autoradiography analysis were performed after the last imaging session, to assess the accumulation of ^{52}Mn. In agreement with the results obtained from the *in vivo* measurements, the quantification of tracer uptake from the brain sections showed signal-to-background indexes lower for

the mice injected with ^{52}MnDPDP (t(2.2)=-4.30, *p=0.04) (Fig. 4.4.5a-b). By contrast, the pancreas sections of mice treated either with ^{52}MnDPDP or $^{52}MnCl_2$ showed no clear difference in the tracer uptake (Fig. 4.4.5c).

The quantification of tracer that was performed *ex vivo* in isolated tissues and measured by *γ*-counter agreed well with the *in vivo* PET measurements. Indeed, the uptake values of ^{52}Mn normalized for the weight of tissues (%ID/g) were significantly lower in the heart of mice that were injected with ^{52}MnDPDP (t(2.69)=-3.44, *p=0.04). Similar tendencies were also observed from the analysis of other organs, such as brain (t(2.05)=-2.30, p=0.14) and bone (t(3.22)=-2.56, p=0.08), in comparison with the muscle, that showed a higher accumulation of ^{52}Mn in the mice that were treated with ^{52}MnDPDP (Fig. 4.4.5d).

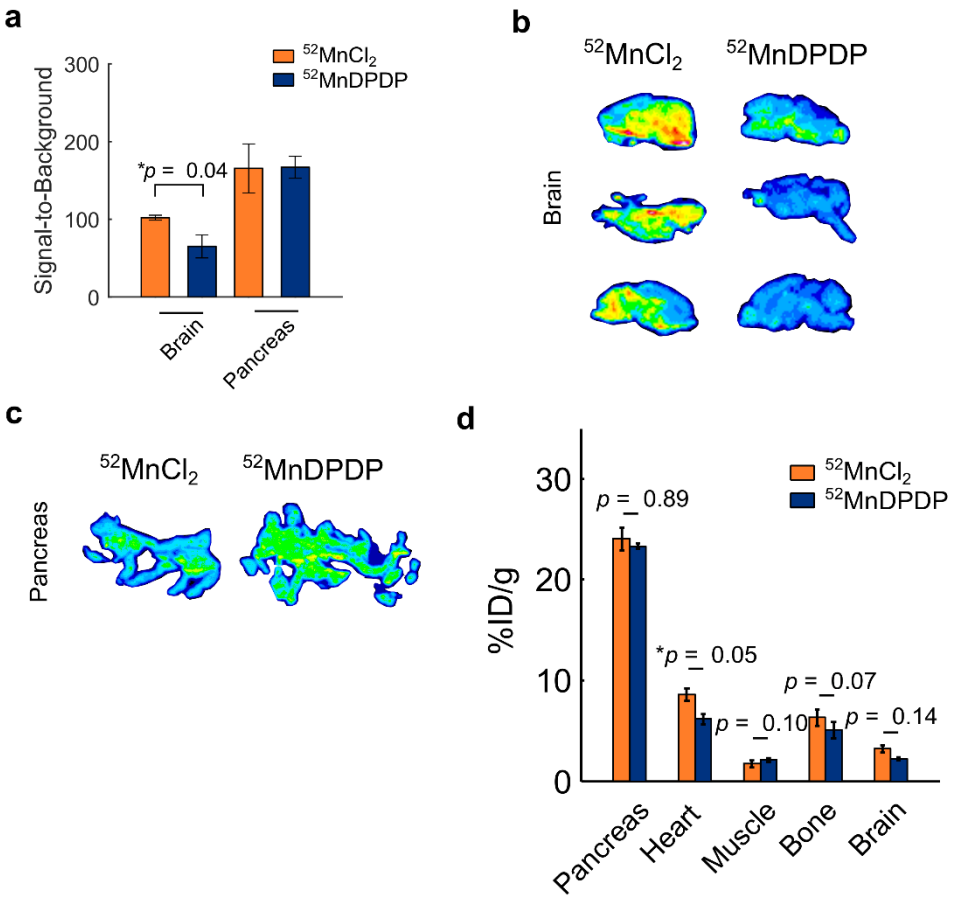

Fig. 4.4.5 Lower brain and heart ^{52}Mn uptake by using ^{52}MnDPDP

(**a**) The bar plots show the mean values ± SD of signal measured from the autoradiography of brain and pancreas sections. (**b**) Sequential brain cryosections were obtained from the groups of mice injected with $^{52}MnCl_2$ or ^{52}MnDPDP (n=3/3), respectively, after the last imaging session (72 h). (**c**) *Ex vivo* autoradiography of the pancreas sections in both the groups and (**d**) bar plots depicting the mean values ±

SD of the %ID/g of the tissues measured by γ-counter for the respective groups. Statistical significances between the groups in the late accumulation of ^{52}Mn were calculated by a two-sample Student's *t*-test assuming unequal variance between the groups.

4.5 PET Imaging to Investigate the Effect of a Quinoxaline Derivative

4.5.1 Radiolabeled Ex4 Binds GLP-1R in an INS-1 Tumor Model

A preliminary study examined whether the accumulation of [^{64}Cu]Ex4 was specific for the receptor expressed in the INS-1 cells-derived tumors. For this purpose, tumor-bearing mice were treated either with C2 (7 or 14 mg/kg) or with an excess of non-radioactive Ex4 (30 mg/kg) at 15 and 3 minutes, respectively, prior to the administration of the PET tracer. The treated groups and the control group of mice were measured with 10-min static PET at 1 h post injection.

Tumor uptake values in the mice treated with 14 mg/kg and in the control group were similar, showing %ID/mL equal to 8.7±2.7 and 9.1±1.5, respectively. The mouse treated with 7 mg/kg showed %ID/mL equal to 15.9. A drastic reduction in the tracer uptake was observed in both groups of mice treated with non-radioactive Ex4 (Fig. 4.5.1a). A statistical comparison was thus performed by grouping those mice treated with only non-radioactive Ex4 (n=1) or in combination with C2 (n=1). The comparison of groups showed tracer uptake values that were significantly lower in the INS-1 tumors ($t(2.1)=9.8$, $*p=0.01$), with %ID/mL equal to 0.4±0.1 and 9.1±1.5 for the group treated with the non-radioactive peptide and the control group, respectively (Fig. 4.5.1a, b). By contrast, the other reference tissues showed similar tracer uptake values, with %ID/mL equal to 0.2±0.0 and 0.3±0.2 in the muscle of the treated and the control group, respectively, and 50.8±8.1 and 58.0±10.9 in the kidneys of the respective groups.

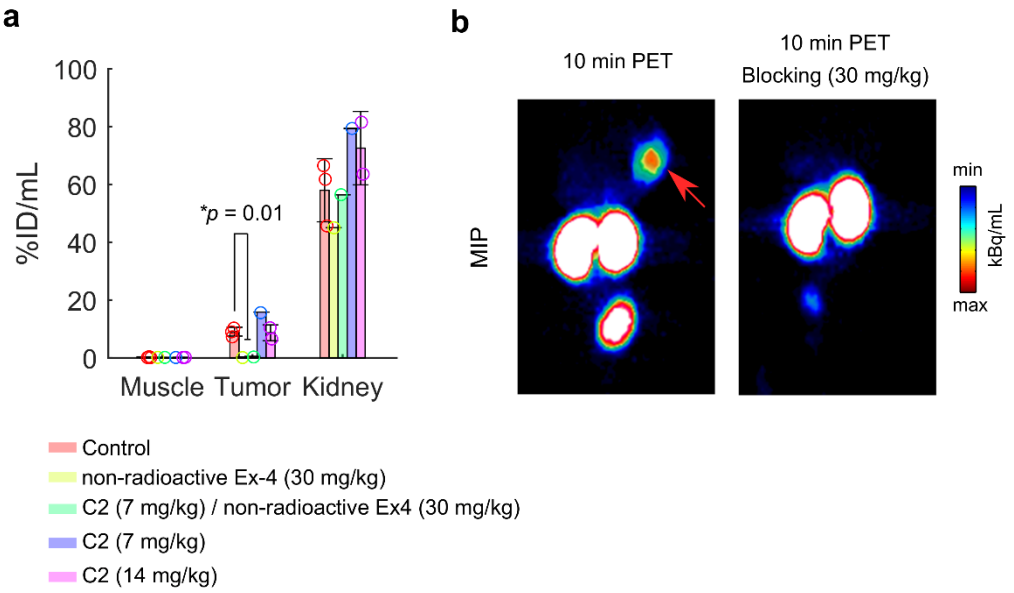

Fig. 4.5.1 Blocking studies revealed a specific decrease of tracer uptake by INS-1 tumors

(**a**) The bar plots show the mean values ± SD (%ID/mL) and the individual data points (circles) reflecting the tracer uptake for the INS-1 cells-derived tumors, muscle and renal cortex. A comparison of tracer uptake values between the groups are calculated by a two-sample Student's *t*-test. (**b**) Representative maximal intensity projections (MIP) obtained from 10-min static PET scans show the tracer uptake (kBq/mL) in the tumors (red arrow), renal cortex and bladder in the control group (right) and the group treated with 30 mg/kg of non-radioactive peptide (right) before the injection of [^{64}Cu]Ex4.

4.5.2 Effect of Quinoxaline on the Uptake of Radiolabeled Ex4 in an INS-1 Xenograft Mouse Model

To determine whether the administration of C2 might modulate the specific binding of [^{64}Cu]Ex4 for the GLP-1R, eight cohorts of tumor-bearing mice were treated using different doses of C2 (15, 25, 35 mg/kg) and at different injection times (0, 15, 30 min before the PET tracer injection).

Along with a progressive decrease observed in the blood glucose level, increasing values in the area of tumors were measured between 1 and 3 weeks after the inoculation of INS-1 cells (Fig. 4.5.2a, b).

In vivo measurements were typically performed three weeks after the subcutaneous inoculation of INS-1 cells. By evaluating the dynamic uptake curves measured by PET, the mice treated with C2 (25 mg/kg) showed uptake values between 0-30 min that were slightly lower in comparison with the values measured from the mice receiving only a vehicle solution at 15 min before the

injection of the PET tracer (Fig. 4.5.2c). Subsequently, the uptake values measured between 30-60 min were analogues in both the groups.

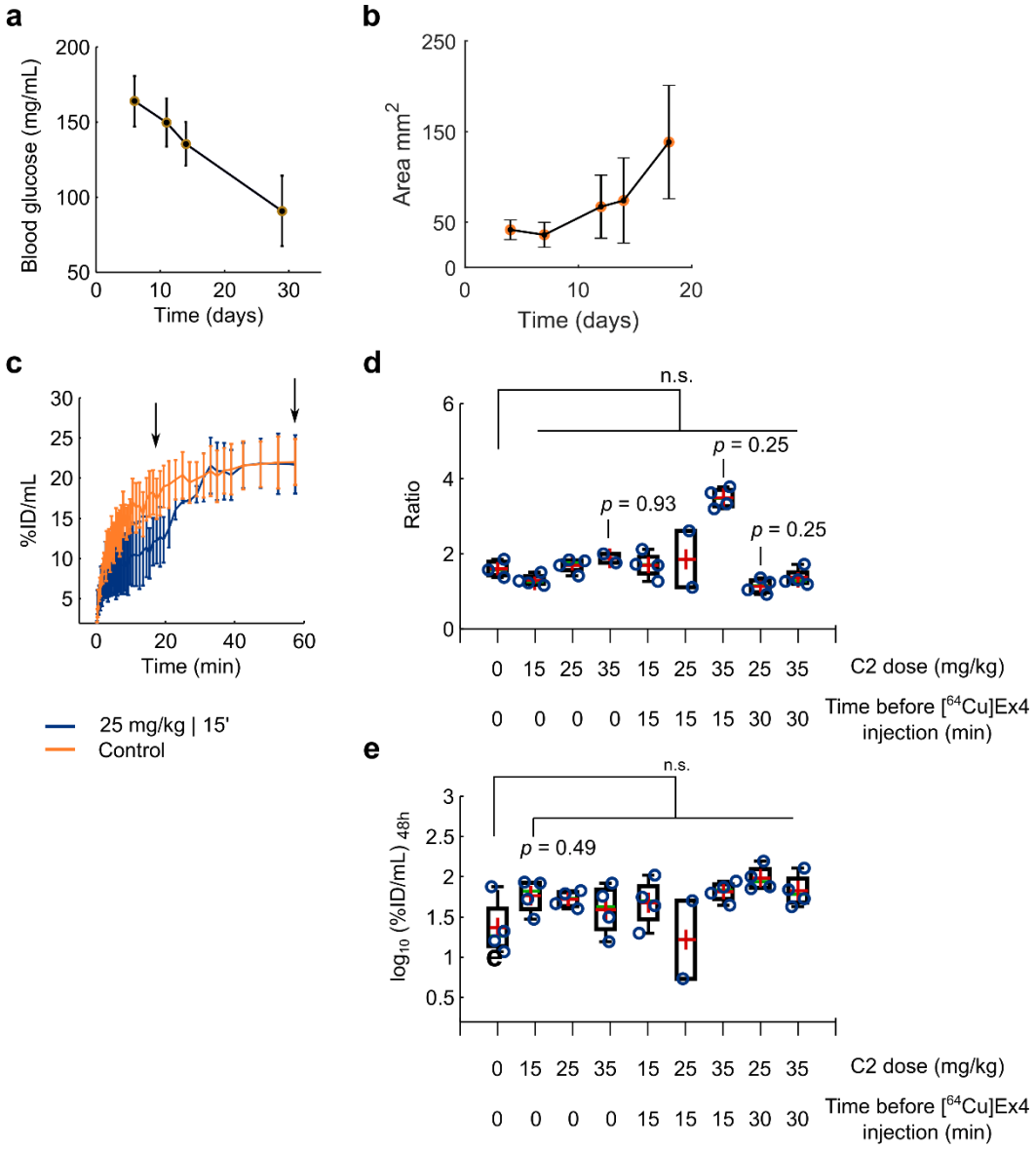

Fig. 4.5.2 Dynamic PET during C2 challenge and quantification of tracer retention

The mean values ± SD of the (**a**) blood glucose levels (mg/dL) and (**b**) tumor growth (mm^2) are plotted along the time (days) after the inoculation of INS-1 cells. (**c**) The dynamic curves show the mean values ± SD (%ID/mL) plotted from the INS-1 tumors of control and mice treated with 25 mg/kg of C2 solution 15 min before the administration of the tracer. The boxes depict the 1st, 2nd (green line), the 3rd and the mean values (red crosses) of (**d**) the ratios calculated between the PET signal measured at 1 h and 24 h post injection. (**e**) The quantification of tracer uptake in the tumors were performed at 48 h post injection. The boxes show the interquartile range of the log_{10}(%ID/mL) calculated for each group. Differences between the control and the treated groups were calculated by multiple comparison Steel's method.

Follow-up of tracer uptake in the tumors was performed through the acquisition of static PET scans at 1 h and 24 h post injection. Regarding the comparison of groups, only slight differences were observed between the groups that were injected either at different injection time or doses of C2 before the PET tracer. Slight tendencies were observed in the group of mice treated with 35 mg/kg, which showed higher ratio values (Fig. 4.5.2d). In opposite tendency, the group of mice receiving 25 mg/kg of compound 30 min before the tracer injection showed lower ratio values compared to the control group (Z=-1.94, *p*=0.25).

Table 4.5.1 Ratio calculated between the PET signal measured at 1 h and 24 h post injection

Ratio at different injection time and doses of C2

	Ratio		
Doses (mg)	0 min	15 min	30 min
0	1.6 ± 0.2	-	-
15	1.3 ± 0.1	1.7 ± 0.3	-
25	1.7 ± 0.2	1.9 ± 1.1	1.1 ± 0.2
35	1.9 ± 0.2	3.5 ± 0.3	1.4 ± 0.2

The biodistribution of tracer was performed at later time points (48 h) to enable the wash-out of tracer from the non-specific tissue. The tracer amount calculated from the groups treated with C2 showed slightly higher values. However, the statistical analysis revealed only slight differences with the control mice, which were treated with a vehicle solution (Fig. 4.5.2e).

4.5.3 Dynamic PET to Monitor the Effect of Quinoxaline Challenge in Engrafted Islets During a Constant Infusion of Radiolabeled Ex4

For animal safety reason, further studies were carried-out to determine the effect of lower doses of C2 (2 and 5 mg/kg).

To assess the viability of engrafted islets, mice were previously examined through the acquisition of dynamic PET scans. From the evaluation of tracer uptake curves, heart and muscle tissues showed a peak within the first minutes which

was followed by a progressive decrease in the calculated %ID/mL with values decreasing from 18.5±0.8 to 1.1±0.2 and 1.4±0.5 to 0.2±0.1, respectively. In comparison to those tissues displaying a progressive wash-out of tracer, the engrafted islets showed uptake values (Fig. 4.5.3a) equal to 1.6±0.3 and 1.1±0.2 %ID/mL, suggesting a stable retention of the PET tracer overtime at 1 h after [^{64}Cu]Ex4 injection. This behavior was also observed by evaluating the ratio obtained from the normalization of the signal measured from the engrafted islets with that of the muscle or heart, which are used as reference tissue for the non-specific specific binding of the tracer (Fig. 4.5.3b).

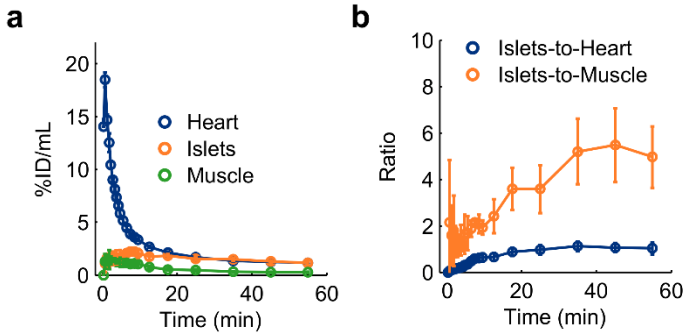

Fig. 4.5.3 Dynamic PET imaging of [^{64}Cu]Ex4 of islet cell transplant

A group of C3H mice was dynamically measured (0-1 h) with PET to evaluate the engraftment efficiency of islets 4 weeks after the transplantation in the right calf of mice. (**a**) The dynamic PET tracer uptake curves show the mean values ± SD (%ID/mL) for the islet transplant, the heart and the muscle. (**b**) As further reference, the mean values ± SD of islet-to-heart and islet-to-muscle ratios are plotted over time.

The mice that were found with detectable engrafted islets (n=6 out 10) were furtherly measured to investigate the effect of C2, which was administered as a bolus injection 20 min after the infusion of [^{64}Cu]Ex4 solution. The PET tracer was continuously administered until 50 min after the start of dynamic PET measurements. A bolus injection of C2 solution at 2 or 5 mg/kg of dose (n=3/3) was subsequently administered 20 min after the infusion of radioactive tracer. The measured uptake curves showed a progressive accumulation of the PET tracer in the muscle and heart until 50 min from the start of the measurements (Fig. 4.5.4a, b). When the infusion pump was stopped, a progressive decrease in the signal was observed in the muscle and heart between 50 and 60 min, indicating a progressive wash-out of the PET tracer from the same tissues. By contrast, the engrafted islets showed a steady increase of the signal over the

entire measurement time. The analysis of the ratio values between the engrafted islets and the muscle of the calf revealed no clear differences between the uptake curves with 2 or 5 mg/kg (Fig. 4.5.4c).

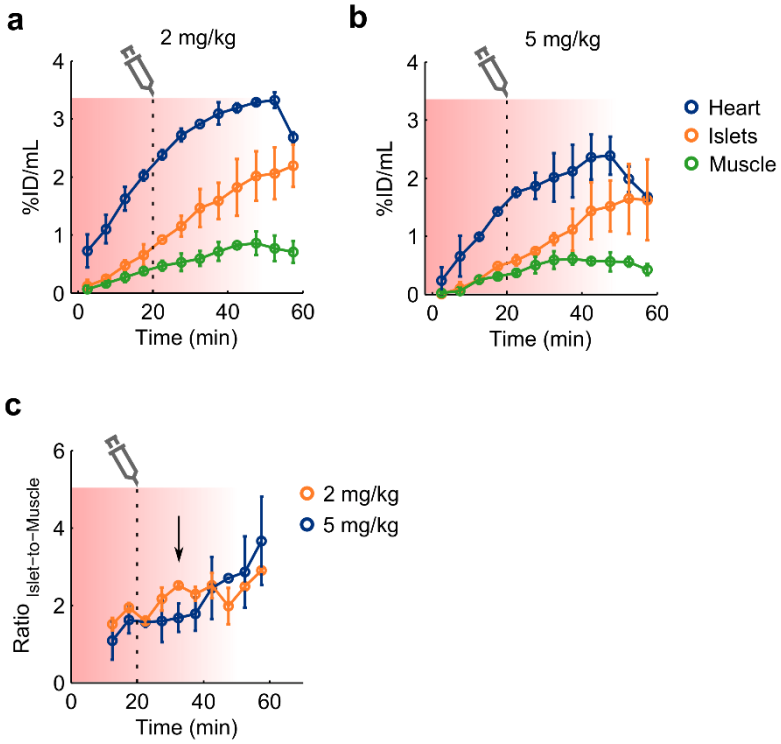

Fig. 4.5.4 Dynamic PET imaging monitors the challenge of GLP-1R by bolus injection of C2

The dynamic PET tracer uptake curves show the mean values ± the SD (%ID/mL) plotted over the time for the region of interest including the islet transplant, the heart and the muscle of the group treated with (a) 2 mg/kg or (**b**) 5 mg/kg of C2 dose. (**c**) The dynamic uptake curves display the mean values ± SD of the ratio values calculated between the %ID/mL measured from the engrafted islets and the surrounding muscle.

4.5.4 A Bolus-Infusion Protocol and Dynamic PET to Assess the Effect of Quinoxaline in the Pancreas of Healthy Mice

In the next experiment, the effect of C2 was examined by measuring the dynamic uptake curve of tracer in the native pancreas of healthy C3H mice. Compared to the previous protocol, the PET tracer and C2 (5 mg/kg) were simultaneously administered using a bolus-infusion protocol and through the same tail vein catheter.

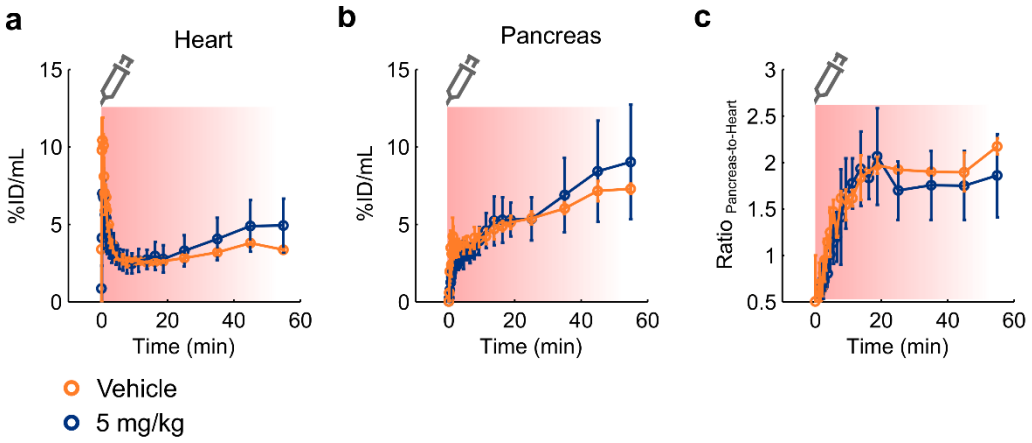

Fig. 4.5.5 Monitor the GLP-1R occupancy by constant infusion of C2

The dynamic uptake curves show the mean uptake values ± SD (%ID/mL) plotted over the time measured in (**a**) the heart and (**b**) the pancreas of both groups (n=4/2). (**c**) The pancreas-to-heart ratios are plotted over the time.

The analysis of the uptake curves measured from the heart indicated a rapid perfusion followed then by a rapid wash-out of the PET tracer. Subsequently, a steady increase of signal was observed, due to the constant infusion of tracer solution (Fig. 4.5.5a, b). Interestingly, both the regions of pancreas and heart showed tracer uptake values that were slightly higher in the treated group compared to the group of mice receiving only the vehicle solution. The ratio values calculated between the signal of the pancreas and heart decreased approximatively 20 min after the infusion of C2 and the radiotracer (Fig. 4.5.5c). By contrast, the control group showed steady ratio values until the end of the measurements.

5 Discussion

In the last decades, imaging methods have been developed to assess β-cell mass (BCM) and function from the native and diseased pancreas (Andralojc et al., 2012, Gotthardt et al., 2014). In this respect, GLP-1R has been shown to be a promising target to estimate BCM *in vivo* using radiolabeled exendin-derivatives probes (Eriksson et al., 2016). Although only little is known on the specificity of Mn for the pancreatic islets, probing the activity of VDCC seems to be a promising approach to assess the functionality of the pancreas. Thus, it has been demonstrated the feasibility of a dual PET/MRI approach to quantitatively correlate BCM and function *in vivo* by simultaneously targeting the GLP-1R and the activity of VDCC of β-cells.

5.1 A ME-MRI Protocol to Assess *In Vivo* β-cell Function

The aim of this section was to implement a quantitative ME-MRI protocol to measure the uptake of Mn in the whole pancreas. To achieve this, a VFA approach, that enables the acquisition of parametric T_1 maps at high temporal resolution, was examined to yield accurate T_1 values. The calculation of longitudinal relaxivity coefficients regarding the effect of $MnCl_2$ and Gd-based contrast agents is in good agreement with the previous studies (Kreft et al., 1993, Shen et al., 2015).

Regarding the optimization of flip angles for the quantification of a range of T_1 values, the values calculated using three and four FAs led to a drastic improvement of the T_1 accuracy compared to a two-angle method, which is in agreement with the reports of other studies (Wang et al., 1987, Deoni et al., 2003). At the same time, other *in vitro* experiments showed a deterioration in the T_1 accuracy using a multiple FAs approach, especially for the images with artificially high numbers of acquisitions. In this regard, previous studies

suggested that the introduction of a noise bias is more likely when more data points are included for the calculation of T_1 (Cheng and Wright, 2006). Another potential source of error consists of the residual transverse magnetization after each excitation RF pulse. It is known that the complete spoiling of the transversal magnetization is especially important for the acquisition of GRE images set to very low TR (<10 ms), larger flip angles as well as for the quantification of samples containing T_1 values higher than 1000 ms (Lin and Song, 2009). A further experiment was performed using a higher gradient field (600 mT/m) and by acquiring GRE images at high spatial resolution (0.2 mm). In this case, an improvement of the T_1 accuracy using multiple FAs was observed only from the images acquired at low numbers of acquisitions, while the images acquired at high numbers of acquisitions resulted again in a strong deterioration of T_1 accuracy.

Due to the possible inhomogeneities in the RF-transmitter, further corrections of T_1 values could be achieved by the acquisition of B_1 maps using an actual flip angle method. This would ideally lead to a further reduction of the error along the entire volume.

The *in vivo* measurements using a two-angle method showed high concentrations of contrast agent until 24 h after the administration of $MnCl_2$. The measured T_1 values correlated with signals acquired using a STIR protocol that was designed for the suppression of signal from the pancreas. Altogether, those results suggest that both measurements can be accurate for the detection of low Mn concentrations in the pancreas until 24 h after the injection of $MnCl_2$.

By contrast, the negative correlation coefficients obtained from the correlation analysis of PET/MRI signals of pancreas could be associated to the different distribution of Mn and the PET tracer throughout the pancreas. In comparison with the PET signal that was measured from the renal cortex, the tracer was retained in the pancreas of healthy mice. As it has been shown in other studies (Wild et al., 2006, Connolly et al., 2012b), the high accumulation of radiolabeled exendin-derivatives in the renal cortex is a problematic issue for the correct

quantification of the pancreas because of spill-over effects, as well as for the high radiation doses to the kidney .

The combination with MRI with PET represents a main advantage for the quantification of the PET tracer from the entire pancreas. In perspective, the implementation of multiparametric and co-registered PET/MR images would enable the automated detection, segmentation and quantification of the different pancreatic regions.

5.2 The Role of Exocrine and Endocrine Pancreas on the Uptake of Mn

In this work, the feasibility of a PET/MRI approach to measure both BCM and function was investigated by comparing the measurements performed to measure the pancreas of control and transgenic RIP1-Tag2 mice. A multimodal PET/MRI approach could localize the pancreata at high anatomical resolution and quantify the PET signal originated from the pancreatic tumors of transgenic mice.

In vivo PET of radiolabeled Ex4 suggested levels of GLP-1R which were approximatively three times higher in 13 to 15-week-old RIP1-Tag2 mice compared to the control group. Analysis of autoradiography of the pancreas sections confirmed higher ratio values for the pancreas of the transgenic mice. As the regression analysis yielded strong positive R^2 coefficients between the islet-to-exocrine ratios and the dimension of spots, the *ex vivo* quantification of the PET tracer can be related to the actual BCM. Compared to the healthy mice, the analysis of the relationship between the quantified PET signal and the islet dimension was weaker for the pancreas of the transgenic mice. Those differences between the groups could be due to the dysregulations in the expression of GLP-1R in the islets of transgenic RIP1-Tag2 mice undergoing β-cell hyperplasia (Bergers et al., 1999). The mechanisms and the uptake of radiolabeled exendin-derivatives have been already demonstrated in previous studies showing the specific accumulation of tracer within the pancreatic cells expressing both GLP-1R and insulin (Berclaz et al., 2015, Brom et al., 2014, Connolly et al., 2012a).

Here it has been demonstrated that the uptake of radiolabeled Ex4 was specific for the insulin-secreting cells of pancreata of RIP1-Tag2 mice. The distribution of biometals, analyzed through LA-ICP-MS imaging showed clear similarities with the accumulation of the radioactive tracer especially by evaluating the distribution of important endogenous biometals, such as calcium and zinc, which are essential for the metabolism of insulin. The recruitment of high levels of zinc within the pancreatic β-cells has been shown to be coupled with the synthesis and the storage of insulin complexes. Furthermore, the oscillations in the intracellular levels of calcium are linked with the fusion and the release of insulin granules in the extracellular space in response to glucose (Cabrera et al., 2006). In the *ex vivo* analysis, it was not possible to exclude whether the tracer has been internalized by other islet cell types. On the other hand, previous studies showed that rodent islets are predominantly constituted by a dense core of β-cells (85-90%), surrounded by a mantle of α-cells (10-15%) (Kim et al., 2009).

In the present study, it has been shown the first validation of *in vivo* MRI measurements related to the functionality of β-cells. To achieve this purpose, follow-up of the PET tracer and the MRI contrast agent was performed at early and late time points by using both *in vivo* and *ex vivo*. *In vivo* MRI measurements suggested that the uptake of Mn was not related with the accumulation of the PET tracer. The estimated concentrations of Mn were almost two times higher for the pancreas of control mice. Furthermore, those measurements were in contrast with the indexes reflecting the physiological response of insulin to glucose measured in isolated islet cells. Indeed, the islets of transgenic mice showed elevated insulin levels, which could be related to an elevated functionality of the pancreas and the consequent hypoglycaemia in RIP1-Tag2 mice. The images of ^{55}Mn showed levels of contrast agents that were inversely related to the levels of calcium and zinc, indicating that the distribution of Mn was not specific for endocrine pancreas. Furthermore, the comparison of elemental images with the autoradiography of radiotracer revealed that the accumulation of radioactive Ex4 does not correlate with the distribution of Mn throughout the native pancreas. Altogether, those results indicate that *in vivo* MRI measurements at early time points, are not directly related to the functionality of the endocrine pancreas.

Here it has not been investigated whether the exposure of mice to high glucose concentrations might influence the accumulation of Mn in the pancreas. In this regard, previous studies suggested that the enhancement in the MRI signal can be due to the stimulation of the specific accumulation of Mn in the pancreatic β-cells (Antkowiak et al., 2012, Hernandez et al., 2017). By assessing the distribution of Mn on a further group of mice that was not previously stimulated with glucose, we obtained similar results. On the other hand, here it has been demonstrated that only late imaging of Mn can be related to the endocrine pancreas. This is probably due to the gradual wash-out of the contrast agent from the exocrine pancreas, contemporary to the the specific retention of Mn by the pancreatic islets. A reduction of Mn uptake in the pancreas has been shown to be associated with the loss of BCM in a diabetic murine model (Antkowiak et al., 2012, Hernandez et al., 2017). Instead, other studies monitoring the wash-in and wash-out of Mn suggested that the loss of signal is mainly related to a lack of the islet microvasculature rather than the loss of pancreatic islets in STZ-treated animals (Dhyani et al., 2013). Botsikas et al. showed a decrease in the enhancement of signal from the pancreas in diabetes patients compared the healthy controls (Botsikas et al., 2012) that were measured few minutes after the injection of MnDPDP. In the past, MnDPDP was introduced into the clinical market with applications in the detection of liver and pancreatic lesions (Ahlstrom and Gehl, 1997). The retrospective evaluation of clinical data suggested that imaging of MnDPDP at late time points might improve the detection and the characterization of endocrine tumors, which is due to the lower contrast enhancement found in the liver parenchyma in comparison with the signal from the liver lesions (King et al., 2002, Wang, 1998).

Those evidences suggest that, during the early distribution of contrast agent, Mn transiently binds the exocrine tissue following then a gradual wash-out of the contrast agent. This hypothesis is supported by the positive correlation between PET and MR images acquired at late time points in our studies. Further confirmations were provided by the *ex vivo* analysis of pancreata. Indeed, the retention of Mn merged with the accumulation of the PET tracer binding GLP-1R and the endogenous levels of calcium and zinc.

Regarding the potential toxic effects of Mn exposure, high concentrations of Mn might negatively affect the secretion of insulin. The analysis performed on isolated islets showed similar physiological response of insulin to glucose between the groups of mice assessed at different time points (1 h and 24 h) after the injection of the contrast agent. Further studies would be required to evaluate the effect of prolonged exposures to Mn on the secretion of insulin.

In conclusion, the retention of Mn in the endocrine tumors and the native islet cells is associated with β-cell function. The development of novel carrier systems would reduce the risk of high Mn exposure in the off-target tissues, thus facilitating the translation of Mn-based imaging methods into the clinic. Further investigations would be required to determine the mechanisms underlying the retention of Mn within the pancreatic islet cells. Since Mn has been localized in dense cores nearby the nucleus of β-cells (Leoni et al., 2011), monitoring of Mn transport could be important to characterize the early dysregulations in the secretory pathway occurring during the early pre-diabetic stages.

5.3 Mn Can Readily Enter the Engrafted Islet cells

In the next future, cell therapy by implantation of previously isolated and viable islets aims to substitute long-term insulin treatments in patients with severe type-1 diabetes. In this work, a combined PET/MRI approach was tested to determine useful information on the viability of engrafted islets, especially regarding the feasibility to measure mass and function. In agreements with other studies, an increase of signal has been observed until 4 weeks after the transplantation of islet cells in the calf of the leg of healthy mice. The overtime increase of PET signal, reflecting an increase of the uptake of a radiolabeled exendin-derivative targeting GLP-1R, could be associated with a progressive increase in the expression of viability, such as the vascularization markers (Eter et al., 2015). In this perspective, the quantification of radiolabeled Ex4 could be potentially exploited to investigate the islet viability in response to the treatments as well as to optimize new protocols for increase the survival of islets after transplantation.

Similar conclusions could also be drawn from the evaluation of *in vivo* ME-MRI measurements. The combination of *ex vivo* autoradiography and elemental

imaging techniques confirmed the specific distribution of exogenous Mn and the PET tracer within the engrafted islets. Indeed, the results showed that the elemental images of exogenous ^{55}Mn matched with those obtained from the measurement of other divalent cations, which are known to be involved in the processing and the secretion of insulin (Hou et al., 2009).

The increase of ME-MRI signal could ideally be related to the changes overtime of VDCC activity and therefore, to the metabolism of glucose and the secretion of insulin. To provide supporting evidences on the specificity of Mn uptake, a separated group of transplanted mice was treated with a Ca^{2+}-blocker to suppress the internalization of free Mn in the intracellular space of the engrafted islets. However, both *in vivo* and *ex vivo* measurements could not detect discriminate whether a single administration of diazoxide affected the uptake of Mn by the engrafted islets.

A limiting factor for the validation of methods was the inter-variability in the number islet cells survived after the inoculation. In this regard, further studies based on the histological evaluation of islet cells would provide a better estimation of the actual number of cells. Another possible limitation is the experimental workflow that was used in the studies. Indeed, a single administration of diazoxide following stimulation of mice with high glucose concentrations might be not sufficient to suppress the VDCC activity on the surface of islet β-cells. The blocking of VDCC is mediated by the opening of ATP-sensitive potassium channels after the binding with diazoxide. By contrast, a previous study focusing on the functionality of perfused pancreata showed that the secretion of insulin, after inhibition with diazoxide, can be rescued by the administration of high glucose concentrations (Burr et al., 1971).

Although the engrafted islet cells were shown to internalize Mn at higher efficiency compared to the surrounding muscle tissue, *ex vivo* analysis of the pancreas indicated that Mn was not specific for the native pancreatic islets.

Altogether, a combined PET/MRI approach has the potential to investigate the viability of engrafted islet cells overtime in a rodent model. In agreement with other studies focused on the validation of PET and MRI, (Antkowiak et al., 2012,

Meyer et al., 2015, Hernandez et al., 2017) Mn-based imaging methods have the potential to non-invasively assess the functionality of the whole pancreas.

5.4 ^{52}MnDPDP, an Achievable Clinical Alternative for the Assessment of β-cell Function and Mass

This study focused on the characterization of the pharmacokinetics of ^{52}Mn using *in vivo* PET imaging. For this purpose, separated cohorts of healthy mice were administered either with $^{52}MnCl_2$ or ^{52}Mn radiolabeled with DPDP ligand.

It is already known that the accumulation of Mn is regulated by the activity of specialized excitable cells enabling the gating of free Mn and other divalent cations (Silva et al., 2004, Pan et al., 2011a, Pan et al., 2011b). Thus, a major concern about using of Mn-based compounds designed for imaging is their potential adverse effects on off-target tissues. In this context, ^{52}Mn represents a novel radioactive isotope of manganese that offers the possibility to monitor the pharmacodynamics of Mn-based imaging probes at high sensitivity by PET using trace amount of Mn ions.

Here we showed a drastic reduction in the PET signal detected from the heart, bone and brain in the group treated with ^{52}MnDPDP, which can be related to a lower availability of free Mn ions, that are, instead, partially bound to DPDP. The biodistribution of ^{52}MnDPDP agreed well with the previous MRI studies focused on the pharmacokinetic of paramagnetic MnDPDP (Jynge et al., 1997, Ni et al., 1997), suggesting that ^{52}Mn complexed with DPDP is safer in comparison to ^{52}Mn administered as the free salt.

Previous studies suggested that the chelation of Mn might not prevent the accumulation in the CNS, mostly because of the gradual release of metal in the circulating blood (Gallez et al., 1998). Our data show in contrast that the delivery of ^{52}Mn with DPDP resulted in decreased binding of free ^{52}Mn in some brain regions, including the pituitary gland and the olfactory bulbs. High concentrations of Mn in the same areas were shown in the human brain (Bonilla et al., 1982). However, the accumulation of ^{52}Mn observed overtime until 72 h post injection might be related to the releasing of metal from the complex as well as to the

recruitment of tracer in the tissues like pancreas and brain which are characterized by a high turnover of the divalent metals.

In comparison with those results, the distribution of the tracer, administered either as free salt or complexed with DPDP, was analogue in the liver and pancreas. This might indicate that other factors, including the perfusion and other physiological processes, play a crucial role in the biodistribution of ^{52}Mn. In this regard, the diffusion of DPDP through the cellular membrane can be associated with a greater accumulation of tracer in the muscle compared to the mice that were administered with free Mn. Regarding the biodistribution of ^{52}Mn delivered by DPDP, it has been shown that a release of free Mn occurs by transmetallation of Mn^{2+} with Zn^{2+} within the complex. Simultaneously to the release of Mn in the blood plasma, the diffusion of metabolites throughout the plasma membrane is promoted by the cleavage of phosphate groups by the alkaline phosphatases (Toft et al., 2001, Schmidt et al., 2002). The transport of ^{52}Mn complexed with DPDP ligand was demonstrated by the high accumulation of ^{52}Mn measured in the bladder of mice. Previous studies using paramagnetic MnDPDP showed that the complex is metabolized and rapidly transferred from the plasma to the urine through the renal excretion (Hustvedt et al., 1997).

To suppress the internalization of free ^{52}Mn released from the complex, a separated group of healthy mice was treated with a Ca^{2+}-blocker few minutes before the injection of ^{52}MnDPDP. The similarities observed in the uptake curves measured suggest that a single high dose of blocking compound did not efficiently affect the intracellular uptake of ^{52}Mn.

Due to the high retention of Mn in the pancreas, PET imaging of radioactive manganese with short half-life can be applied to evaluate the functionality of the pancreas and to monitor the diabetes stages progression (Graves et al., 2017, Topping et al., 2017). Regarding the accumulation of ^{52}Mn in the pancreatic islets, the low tissue contrast observed from the analysis of the autoradiography of pancreata sections indicate that both radioactive tracers accumulate at low tissue specificity within the pancreatic islet cells compared to the surrounding exocrine pancreas.

Because the accumulation of Mn is potentially toxic, the main strategies focused on the delivery of detectable amounts of tracer while reducing the accumulation in off-target tissue with potential toxic effects (Silva et al., 2004). Altogether, the evidences that are provided here corroborate previous results conducted to determine the higher safety of ^{52}MnDPDP compared to $^{52}MnCl_2$, mostly because of the lower accumulation in the brain region and the heart. The translation of Mn imaging methods can find potential applications in the evaluation of cellular and molecular mechanisms linked to the turnover of divalent ions, such as zinc and calcium, including the secretion of insulin by the pancreatic β-cells.

In these investigations, only ^{52}Mn biodistribution and the potential toxicity by high accumulation of $^{52}MnCl_2$ and ^{52}MnDPDP in off-target tissues have been studied.

Previous *in vivo* PET studies at early time points (1 h) have shown the potential of $^{52}MnCl_2$ in assessing the functionality of the pancreas in both models of type 1 and type 2 diabetes (Hernandez et al., 2017). However, since Mn accumulates at high concentrations in the exocrine pancreas at early time points (Michelotti et al., 2020), it would be important in the subsequent studies to validate the actual contribution of the endocrine pancreas in the tracer uptake in a diabetic mouse model.

5.5 C2 Might Negatively Affect the Internalization of Radiolabeled Ex4

In this study we aimed to monitor the action of C2, a known positive ago-allosteric modulator of GLP-1R, by *in vivo* PET. In the present study, the accumulation of radiolabeled Ex4 was shown to be specific for the INS-1 tumors in a xenograft mouse model. The following studies aimed to examine the effect of C2 on the tracer uptake by the INS-1 cells. A bolus injection of C2 seemed to induce a lower tracer uptake during the early distribution of the tracer. This outcome could be related to the lower availability of receptors on the surface of INS-1 cells. Furthermore, high ratio values, calculated between the PET signal measured at early and late time points, were found in the group of mice receiving C2 at high doses (35 mg/kg). Although the statistical analysis revealed no significant differences, those results suggest that increasing amounts of C2 might negatively influence the accumulation and the retention of the PET tracer in the tumors.

Using a different approach, similar tendencies were obtained by monitoring the dynamic PET signal from the engrafted and pancreatic islets by administering lower dose of C2 (2 and 5 mg/kg).

In conclusion, discerning the effects of C2 was challenging and concerned many aspects of the experimental design, including the choice of the dose, injection time and animal model. Nevertheless, the modulation through ago-allosteric small molecules is a novel strategy for the development of drugs. It may find potential applications in the modulation of the binding affinity of radiotracers. (Conn et al., 2012, Wild et al., 2014). Thus, even if an enhanced the specific uptake of radiolabeled Ex4 was not achieved, a dynamic PET imaging protocol remains a promising approach to investigate the ago-allosteric effects of small molecules targeting GLP-1R non-invasively.

6 Conclusion

The combination of *in vivo* and *ex vivo* imaging methods represented a powerful approach for the validation of biomarkers that are related to the viability of pancreatic β-cells. Our studies supported the feasibility of simultaneous PET/MRI to assess BCM and function using radiolabeled Ex4 and Mn, respectively. In this regard, Mn was shown to be retained until late time points within the native pancreatic islet cells as well as in the pancreatic insulinomas. The outcome of this research finds potential applications in the optimization and the translation of Mn-based imaging protocols to non-invasively measure β-cell function. In the clinic, diabetic patients with low innate BCM and impaired insulin response to glucose would benefit from a tool to monitor the progressive deterioration of the endocrine pancreas. The development of novel carrier systems delivering low Mn amounts to the pancreatic islets would reduce the unspecific uptake by the exocrine pancreas and the risk of cellular toxicity in off-target tissues caused by the elevated Mn accumulations. In this perspective, further investigations would be required to elucidate the cellular processes involved in the late sequestration of Mn by the excitable cells of pancreas.

7 Summary

The goal of this project was the development of a PET/MRI method to simultaneously measure BCM and function. Towards the establishment of *in vivo* ME-MRI, a VFA T_1 mapping protocol was optimized *in vitro* and *in vivo.* Simultaneous PET/MRI was shown to quantify and correlate radiolabeled Ex4 and Mn uptake throughout the pancreas of healthy and transgenic RIP1-Tag2 mice, a spontaneous model of pancreatic neuroendocrine tumors. Most importantly, the validation of *in vivo* imaging methods was performed by combining *ex vivo* autoradiography and LA-ICP-MS imaging. In this regard, the distribution of Mn in the pancreas was cross-validated with the accumulation of the PET tracer and with the endogenous levels of calcium and zinc at both early and late time points post injection. The research findings indicated that Mn accumulated at higher binding affinity in the exocrine pancreas during the early distribution of the contrast agent. By contrast, the retained amount of Mn measured in the pancreas was localized within the native islet cells and insulinomas, suggesting that late MRI measurements of Mn might be linked with β-cell function. The accumulation of Mn was also associated with the accumulation of the PET tracer and the endogenous levels of calcium and zinc. Using a similar procedure in the methodologies, the specificity of Mn uptake was validated in a transplanted mouse model. In this regard, longitudinal measurements by using a combined PET/MRI approach was shown to provide useful information on the viability of engrafted islets between 1 and 4 weeks after the transplantation. By using a different approach, the pharmacokinetics of radioactive ^{52}Mn was investigated on healthy animals. The results obtained from the PET measurements confirmed previous reports regarding the higher safety of MnDPDP, especially regarding the lower tracer uptake that was observed in off-target tissues, such as the heart and specific regions of the brain. In parallel,

different approaches were investigated to non-invasively determine the effects of quinoxaline on the modulation of the uptake of radiolabelled Ex4. *In vivo* PET studies conducted in different animal model could not discern a significant effect of quinoxaline. Nevertheless, a dynamic PET protocol is a promising method to monitor the modulation of the PET tracer uptake.

8 German Summary

Das Ziel dieses Projekts war die Entwicklung einer PET/MRT-Methode zur gleichzeitigen Messung von Beta-Zellmasse und ihrer Funktion. Zur Etablierung einer *in vivo* ME-MRT wurde ein VFA T_1 map Protokoll *in vitro* und *in vivo* optimiert. Simultane PET/MRT wurde verwendet, um in der Bauchspeicheldrüse von gesunden und transgenen RIP1-Tag2 Mäusen, einem spontanen Modell von neuroendokrinen Pankreastumoren, die radiomarkierte Ex4 und Mn Aufnahme zu quantifizieren und die Korrelation aufzuzeigen. Hervorzuheben ist vor allem, dass die Validierung von *in vivo* Bildgebungsmethoden durch Kombination von *ex vivo* Autoradiographie und LA-ICP-MSI durchgeführt wurde. Unter Verwendung des entwickelten Verfahrens wurde die Verteilung von Mn in der Bauchspeicheldrüse mit der Akkumulation des PET Tracers und mit den endogenen Calcium- und Zinkspiegeln sowohl zu frühen also auch zu späten Zeitpunkten nach der Injektion kreuzvalidiert. Die Ergebnisse zeigten, dass sich Mn während der frühen Phase der Kontrastmittelverteilung mit einer höheren Bindungsaffinität in der exokrinen Bauchspeicheldrüse ansammelte. Konträr hierzu war die im Pankreas gemessene Menge an zurückgebliebenem Mn in den nativen Inselzellen und Insulinomen lokalisiert, was auf einen Zusammenhang von späten MRT-Messungen von Mn mit der β-Zellfunktion schließen lässt. Die Anreicherung von Mn war auch mit der Anreicherung des PET Tracers und den endogenen Gehalten an Calcium und Zink verbunden. Unter Verwendung einer ähnlichen Verfahrensmethode wurde die Spezifität der Mn Aufnahme in einem transplantieren Mausmodell validiert. In diesem Modell wurde gezeigt, dass longitudinale Messungen unter Verwendung eines kombinierten PET/MRT Ansatzes nützliche Informationen über die Lebensdauer von transplantieren Inseln zwischen 1. und 4. Woche nach der Transplantation liefern. Mit einem anderen Ansatz wurde die Pharmakokinetik von radioaktivem ^{52}Mn an gesunden

Tieren untersucht. Die aus den PET Messungen erhaltenen Ergebnisse bestätigten frühere Berichte zur höheren Sicherheit von MnDPDP, insbesondere zur geringeren Tracer-Aufnahme in Geweben außerhalb des Zielorgans, wie dem Herzen und bestimmten Regionen des Gehirns. Parallel dazu wurden verschiedene Ansätze untersucht, um auf nicht-invasive Weise die Auswirkungen von Quinoxaline auf die Modulation der Aufnahme von radioaktiv markiertem Ex4 zu bestimmen. *In vivo* PET Studien, die in verschieden Tiermodellen bereits durchgeführt wurden, konnten keinen signifikanten Effekt von Quinoxaline feststellen. Dennoch ist ein dynamisches PET Protokoll eine vielversprechende Methode, um die Modulation der PET-Tracer-Aufnahme zu evaluieren.

9 Bibliography

AHLSTROM, H. & GEHL, H. B. 1997. Overview of MnDPDP as a pancreas-specific contrast agent for MR imaging. *Acta Radiol,* 38**,** 660-4.

AMIEL, S. A., CAPRIO, S., SHERWIN, R. S., PLEWE, G., HAYMOND, M. W. & TAMBORLANE, W. V. 1991. Insulin resistance of puberty: a defect restricted to peripheral glucose metabolism. *J Clin Endocrinol Metab,* 72**,** 277-82.

ANDRALOJC, K., SRINIVAS, M., BROM, M., JOOSTEN, L., DE VRIES, I. J., EIZIRIK, D. L., BOERMAN, O. C., MEDA, P. & GOTTHARDT, M. 2012. Obstacles on the way to the clinical visualisation of beta cells: looking for the Aeneas of molecular imaging to navigate between Scylla and Charybdis. *Diabetologia,* 55**,** 1247-57.

ANDREW, A., KRAMER, B. & RAWDON, B. B. 1998. The origin of gut and pancreatic neuroendocrine (APUD) cells--the last word? *J Pathol,* 186**,** 117-8.

ANTKOWIAK, P. F., STEVENS, B. K., NUNEMAKER, C. S., MCDUFFIE, M. & EPSTEIN, F. H. 2013. Manganese-enhanced magnetic resonance imaging detects declining pancreatic beta-cell mass in a cyclophosphamide-accelerated mouse model of type 1 diabetes. *Diabetes,* 62**,** 44-8.

ANTKOWIAK, P. F., VANDSBURGER, M. H. & EPSTEIN, F. H. 2012. Quantitative pancreatic beta cell MRI using manganese-enhanced Look-Locker imaging and two-site water exchange analysis. *Magn Reson Med,* 67**,** 1730-9.

ARTINYAN, A., SORIANO, P. A., PRENDERGAST, C., LOW, T., ELLENHORN, J. D. & KIM, J. 2008. The anatomic location of pancreatic cancer is a prognostic factor for survival. *HPB (Oxford),* 10**,** 371-6.

BAEKKESKOV, S., AANSTOOT, H. J., CHRISTGAU, S., REETZ, A., SOLIMENA, M., CASCALHO, M., FOLLI, F., RICHTER-OLESEN, H. & DE CAMILLI, P. 1990. Identification of the 64K autoantigen in insulin-dependent diabetes as the GABA-synthesizing enzyme glutamic acid decarboxylase. *Nature,* 347**,** 151-6.

BAGGIO, L. L. & DRUCKER, D. J. 2007. Biology of incretins: GLP-1 and GIP. *Gastroenterology,* 132**,** 2131-57.

BANTING, F. G., BEST, C. H., COLLIP, J. B., CAMPBELL, W. R. & FLETCHER, A. A. 1922. Pancreatic extracts in the treatment of diabetes mellitus. *Can Med Assoc J,* 12**,** 141-146.

BARRNETT, R. J. & SELIGMAN, A. M. 1952. Histochemical demonstration of protein-bound sulfhydryl groups. *Science,* 116**,** 323-7.

BASU, R., BREDA, E., OBERG, A. L., POWELL, C. C., DALLA MAN, C., BASU, A., VITTONE, J. L., KLEE, G. G., ARORA, P., JENSEN, M. D., TOFFOLO, G., COBELLI, C. & RIZZA, R. A. 2003. Mechanisms of the age-associated deterioration in glucose tolerance: contribution of alterations in insulin secretion, action, and clearance. *Diabetes,* 52**,** 1738-48.

BAUM, J., SIMONS, B. E., JR., UNGER, R. H. & MADISON, L. L. 1962. Localization of glucagon in the alpha cells in the pancreatic islet by immunofluorescent technics. *Diabetes,* 11**,** 371-4.

BELL, G. I., SANTERRE, R. F. & MULLENBACH, G. T. 1983. Hamster preproglucagon contains the sequence of glucagon and two related peptides. *Nature,* 302**,** 716-8.

BERCLAZ, C., PACHE, C., BOUWENS, A., SZLAG, D., LOPEZ, A., JOOSTEN, L., EKIM, S., BROM, M., GOTTHARDT, M., GRAPIN-BOTTON, A. & LASSER, T. 2015. Combined Optical Coherence and Fluorescence

Microscopy to assess dynamics and specificity of pancreatic beta-cell tracers. *Sci Rep,* 5**,** 10385.

BERGERS, G., JAVAHERIAN, K., LO, K. M., FOLKMAN, J. & HANAHAN, D. 1999. Effects of angiogenesis inhibitors on multistage carcinogenesis in mice. *Science,* 284**,** 808-12.

BLACKMORE, C. G., VARRO, A., DIMALINE, R., BISHOP, L., GALLACHER, D. V. & DOCKRAY, G. J. 2001. Measurement of secretory vesicle pH reveals intravesicular alkalinization by vesicular monoamine transporter type 2 resulting in inhibition of prohormone cleavage. *J Physiol,* 531**,** 605-17.

BLOOM, W. A new type of granular cell inthe islets of Langerhans of man. *Anat Rec,* 49**,** 363-371.

BONILLA, E., SALAZAR, E., VILLASMIL, J. J. & VILLALOBOS, R. 1982. The regional distribution of manganese in the normal human brain. *Neurochem Res,* 7**,** 221-7.

BONNEFOND, A., FROGUEL, P. & VAXILLAIRE, M. 2010. The emerging genetics of type 2 diabetes. *Trends Mol Med,* 16**,** 407-16.

BOTSIKAS, D., TERRAZ, S., VINET, L., LAMPRIANOU, S., BECKER, C. D., BOSCO, D., MEDA, P. & MONTET, X. 2012. Pancreatic magnetic resonance imaging after manganese injection distinguishes type 2 diabetic and normoglycemic patients. *Islets,* 4**,** 243-8.

BOYD, C. A. 2001. Amine uptake and peptide hormone secretion: APUD cells in a new landscape. *J Physiol,* 531**,** 581.

BROM, M., JOOSTEN, L., FRIELINK, C., BOERMAN, O. & GOTTHARDT, M. 2015. (111)In-exendin uptake in the pancreas correlates with the beta-cell mass and not with the alpha-cell mass. *Diabetes,* 64**,** 1324-8.

BROM, M., JOOSTEN, L., OYEN, W. J., GOTTHARDT, M. & BOERMAN, O. C. 2012. Radiolabelled GLP-1 analogues for in vivo targeting of insulinomas. *Contrast Media Mol Imaging,* 7**,** 160-6.

BROM, M., OYEN, W. J., JOOSTEN, L., GOTTHARDT, M. & BOERMAN, O. C. 2010. 68Ga-labelled exendin-3, a new agent for the detection of insulinomas with PET. *Eur J Nucl Med Mol Imaging,* 37**,** 1345-55.

BROM, M., WOLINER-VAN DER WEG, W., JOOSTEN, L., FRIELINK, C., BOUCKENOOGHE, T., RIJKEN, P., ANDRALOJC, K., GOKE, B. J., DE JONG, M., EIZIRIK, D. L., BEHE, M., LAHOUTTE, T., OYEN, W. J., TACK, C. J., JANSSEN, M., BOERMAN, O. C. & GOTTHARDT, M. 2014. Non-invasive quantification of the beta cell mass by SPECT with (1)(1)(1)In-labelled exendin. *Diabetologia,* 57**,** 950-9.

BROWN, J. C. 1971. A gastric inhibitory polypeptide. I. The amino acid composition and the tryptic peptides. *Can J Biochem,* 49**,** 255-61.

BROWN, J. C., PEDERSEN, R. A. GI hormones and insulin secretion. *In:* MEDICA, E., ed. Endocrinology. Proceedings of the Vth Intemational Congress of Endocrinology, 1977 Amsterdam. 568-570.

BUCHANAN, T. A., XIANG, A. H., PETERS, R. K., KJOS, S. L., MARROQUIN, A., GOICO, J., OCHOA, C., TAN, S., BERKOWITZ, K., HODIS, H. N. & AZEN, S. P. 2002. Preservation of pancreatic beta-cell function and prevention of type 2 diabetes by pharmacological treatment of insulin resistance in high-risk hispanic women. *Diabetes,* 51**,** 2796-803.

BURR, I. M., MARLISS, E. B., STAUFFACHER, W. & RENOLD, A. E. 1971. Diazoxide effects on biphasic insulin release: "adrenergic" suppression and enhancement in the perifused rat pancreas. *J Clin Invest,* 50**,** 1444-50.

BUSHBERG, J. T., SEIBERT, J. A., LEIDHOLDT JR, E. M. & BOONE, J. M. 2012. Magnetic Resonance Basics. *The Essential Physics of Medical Imaging* Third Edition ed.

BUTLER, A. E., JANSON, J., BONNER-WEIR, S., RITZEL, R., RIZZA, R. A. & BUTLER, P. C. 2003. Beta-cell deficit and increased beta-cell apoptosis in humans with type 2 diabetes. *Diabetes,* 52**,** 102-10.

CABRERA, O., BERMAN, D. M., KENYON, N. S., RICORDI, C., BERGGREN, P. O. & CAICEDO, A. 2006. The unique cytoarchitecture of human pancreatic islets has implications for islet cell function. *Proc Natl Acad Sci U S A,* 103**,** 2334-9.

CALNE, D. B., CHU, N. S., HUANG, C. C., LU, C. S. & OLANOW, W. 1994. Manganism and idiopathic parkinsonism: similarities and differences. *Neurology,* 44**,** 1583-6.

CAMPBELL, J. E. & DRUCKER, D. J. 2013. Pharmacology, physiology, and mechanisms of incretin hormone action. *Cell Metab,* 17**,** 819-37.

CANTLEY, J. & ASHCROFT, F. M. 2015. Q&A: insulin secretion and type 2 diabetes: why do beta-cells fail? *BMC Biol,* 13**,** 33.

CERANOWICZ, P., CIESZKOWSKI, J., WARZECHA, Z., KUSNIERZ-CABALA, B. & DEMBINSKI, A. 2015. The Beginnings of Pancreatology as a Field of Experimental and Clinical Medicine. *Biomed Res Int,* 2015**,** 128095.

CHEN, C., COHRS, C. M., STERTMANN, J., BOZSAK, R. & SPEIER, S. 2017. Human beta cell mass and function in diabetes: Recent advances in knowledge and technologies to understand disease pathogenesis. *Mol Metab,* 6**,** 943-957.

CHEN, D., LIAO, J., LI, N., ZHOU, C., LIU, Q., WANG, G., ZHANG, R., ZHANG, S., LIN, L., CHEN, K., XIE, X., NAN, F., YOUNG, A. A. & WANG, M. W. 2007. A nonpeptidic agonist of glucagon-like peptide 1 receptors with efficacy in diabetic db/db mice. *Proc Natl Acad Sci U S A,* 104**,** 943-8.

CHENG, H. L. & WRIGHT, G. A. 2006. Rapid high-resolution T(1) mapping by variable flip angles: accurate and precise measurements in the presence of radiofrequency field inhomogeneity. *Magn Reson Med,* 55**,** 566-74.

CHERA, S., BARONNIER, D., GHILA, L., CIGLIOLA, V., JENSEN, J. N., GU, G., FURUYAMA, K., THOREL, F., GRIBBLE, F. M., REIMANN, F. & HERRERA, P. L. 2014. Diabetes recovery by age-dependent conversion of pancreatic delta-cells into insulin producers. *Nature,* 514**,** 503-7.

CHERRY, S. R., SORENSON, J. A. & PHELPS, M. E. 2012a. Modes of Radioactive Decay. *Physics in Nuclear Medicine*

Fourth Edition ed.

CHERRY, S. R., SORENSON, J. A. & PHELPS, M. E. 2012b. Positron Emission Tomography. *Physics in Nuclear Medicine.*

CHO, N. H., SHAW, J. E., KARURANGA, S., HUANG, Y., DA ROCHA FERNANDES, J. D., OHLROGGE, A. W. & MALANDA, B. 2018. IDF Diabetes Atlas: Global estimates of diabetes prevalence for 2017 and projections for 2045. *Diabetes Res Clin Pract,* 138**,** 271-281.

CONN, P. J., KUDUK, S. D. & DOLLER, D. 2012. Drug Design Strategies for GPCR Allosteric Modulators. *Annu Rep Med Chem,* 47**,** 441-457.

CONNOLLY, B. M., VANKO, A., MCQUADE, P., GUENTHER, I., MENG, X., RUBINS, D., WATERHOUSE, R., HARGREAVES, R., SUR, C. & HOSTETLER, E. 2012a. Ex vivo imaging of pancreatic beta cells using a radiolabeled GLP-1 receptor agonist. *Mol Imaging Biol,* 14**,** 79-87.

CONNOLLY, B. M., VANKO, A., MCQUADE, P., GUENTHER, I., MENG, X. J., RUBINS, D., WATERHOUSE, R., HARGREAVES, R., SUR, C. & HOSTETLER, E. 2012b. Ex Vivo Imaging of Pancreatic Beta Cells using a Radiolabeled GLP-1 Receptor Agonist. *Molecular Imaging and Biology,* 14**,** 79-87.

COONS, A. H. & KAPLAN, M. H. 1950. Localization of antigen in tissue cells; improvements in a method for the detection of antigen by means of fluorescent antibody. *J Exp Med,* 91**,** 1-13.

CREUTZFELDT, W. 1979. The incretin concept today. *Diabetologia,* 16**,** 75-85.

DA SILVA XAVIER, G. 2018. The Cells of the Islets of Langerhans. *J Clin Med,* 7.

DEONI, S. C., RUTT, B. K. & PETERS, T. M. 2003. Rapid combined T1 and T2 mapping using gradient recalled acquisition in the steady state. *Magn Reson Med,* 49**,** 515-26.

DHYANI, A. H., FAN, X., LEONI, L., HAQUE, M. & ROMAN, B. B. 2013. Empirical mathematical model for dynamic manganese-enhanced MRI of the murine pancreas for assessment of beta-cell function. *Magn Reson Imaging,* 31**,** 508-14.

DI GIALLEONARDO, V., SIGNORE, A., SCHEERSTRA, E. A., VISSER, A. K., VAN WAARDE, A., DIERCKX, R. A. & DE VRIES, E. F. 2012. 11C-hydroxytryptophan uptake and metabolism in endocrine and exocrine pancreas. *J Nucl Med,* 53**,** 1755-63.

DOYLE, M. E. & EGAN, J. M. 2007. Mechanisms of action of glucagon-like peptide 1 in the pancreas. *Pharmacol Ther,* 113**,** 546-93.

DUNNING, B. E. & GERICH, J. E. 2007. The role of alpha-cell dysregulation in fasting and postprandial hyperglycemia in type 2 diabetes and therapeutic implications. *Endocr Rev,* 28**,** 253-83.

DUPRE, J., ROSS, S. A., WATSON, D. & BROWN, J. C. 1973. Stimulation of insulin secretion by gastric inhibitory polypeptide in man. *J Clin Endocrinol Metab,* 37**,** 826-8.

ENG, J., KLEINMAN, W. A., SINGH, L., SINGH, G. & RAUFMAN, J. P. 1992. Isolation and characterization of exendin-4, an exendin-3 analogue, from Heloderma suspectum venom. Further evidence for an exendin receptor on dispersed acini from guinea pig pancreas. *J Biol Chem,* 267**,** 7402-5.

ERIKSSON, O., ESPES, D., SELVARAJU, R. K., JANSSON, E., ANTONI, G., SORENSEN, J., LUBBERINK, M., BIGLARNIA, A. R., ERIKSSON, J. W., SUNDIN, A., AHLSTROM, H., ERIKSSON, B., JOHANSSON, L., CARLSSON, P. O. & KORSGREN, O. 2014a. Positron emission tomography ligand [11C]5-hydroxy-tryptophan can be used as a surrogate marker for the human endocrine pancreas. *Diabetes,* 63**,** 3428-37.

ERIKSSON, O., LAUGHLIN, M., BROM, M., NUUTILA, P., RODEN, M., HWA, A., BONADONNA, R. & GOTTHARDT, M. 2016. In vivo imaging of beta cells with radiotracers: state of the art, prospects and recommendations for development and use. *Diabetologia,* 59**,** 1340-1349.

ERIKSSON, O., SELVARAJU, R. K., JOHANSSON, L., ERIKSSON, J. W., SUNDIN, A., ANTONI, G., SORENSEN, J., ERIKSSON, B. & KORSGREN, O. 2014b. Quantitative imaging of serotonergic biosynthesis and degradation in the endocrine pancreas. *J Nucl Med,* 55**,** 460-5.

ETER, W. A., BOS, D., FRIELINK, C., BOERMAN, O. C., BROM, M. & GOTTHARDT, M. 2015. Graft revascularization is essential for non-invasive monitoring of transplanted islets with radiolabeled exendin. *Sci Rep,* 5**,** 15521.

FAGERHOLM, V., MIKKOLA, K. K., ISHIZU, T., ARPONEN, E., KAUHANEN, S., NAGREN, K., SOLIN, O., NUUTILA, P. & HAAPARANTA, M. 2010. Assessment of islet specificity of dihydrotetrabenazine radiotracer binding in rat pancreas and human pancreas. *J Nucl Med,* 51**,** 1439-46.

FONSLET, J., TIETZE, S., JENSEN, A. I., GRAVES, S. A. & SEVERIN, G. W. 2017. Optimized procedures for manganese-52: Production, separation and radiolabeling. *Appl Radiat Isot,* 121**,** 38-43.

GALLAMINI, A., ZWARTHOED, C. & BORRA, A. 2014. Positron Emission Tomography (PET) in Oncology. *Cancers (Basel),* 6**,** 1821-89.

GALLEZ, B., BAUDELET, C. & GEURTS, M. 1998. Regional distribution of manganese found in the brain after injection of a single dose of manganese-based contrast agents. *Magn Reson Imaging,* 16**,** 1211-5.

GARCIA, A., MIRBOLOOKI, M. R., CONSTANTINESCU, C., PAN, M. L., SEVRIOUKOV, E., MILNE, N., WANG, P. H., LAKEY, J., CHANDY, K. G. & MUKHERJEE, J. 2011. 18F-Fallypride PET of pancreatic islets: in vitro and in vivo rodent studies. *J Nucl Med,* 52**,** 1125-32.

GIMI, B., LEONI, L., OBERHOLZER, J., BRAUN, M., AVILA, J., WANG, Y., DESAI, T., PHILIPSON, L. H., MAGIN, R. L. & ROMAN, B. B. 2006. Functional MR microimaging of pancreatic beta-cell activation. *Cell Transplant,* 15**,** 195-203.

GOMORI, G. 1941. Observations with differential stains on human islets of langerhans. *Am J Pathol,* 17**,** 395-406 3.

GOTTHARDT, M., EIZIRIK, D. L., CNOP, M. & BROM, M. 2014. Beta cell imaging - a key tool in optimized diabetes prevention and treatment. *Trends Endocrinol Metab,* 25**,** 375-7.

GOTTHARDT, M., LALYKO, G., VAN EERD-VISMALE, J., KEIL, B., SCHURRAT, T., HOWER, M., LAVERMAN, P., BEHR, T. M., BOERMAN, O. C., GOKE, B. & BEHE, M. 2006. A new technique for in vivo imaging of specific GLP-1 binding sites: first results in small rodents. *Regul Pept,* 137**,** 162-7.

GRAVES, S. A., HERNANDEZ, R., VALDOVINOS, H. F., ELLISON, P. A., ENGLE, J. W., BARNHART, T. E., CAI, W. & NICKLES, R. J. 2017. Preparation and in vivo characterization of (51)MnCl2 as PET tracer of Ca(2+) channel-mediated transport. *Sci Rep,* 7**,** 3033.

GRIMELIUS, L. 1968. A silver nitrate stain for alpha-2 cells in human pancreatic islets. *Acta Soc Med Ups,* 73**,** 243-70.

HARRIS, M. I. 1995. Epidemiologic studies on the pathogenesis of non-insulin-dependent diabetes mellitus (NIDDM). *Clin Invest Med,* 18**,** 231-9.

HELLMAN, B. & HELLERSTROM, C. 1961. The specificity of the argyrophil reaction in the islets of Langerhans in man. *Acta Endocrinol (Copenh),* 36**,** 22-30.

HERNANDEZ, R., GRAVES, S. A., GREGG, T., VANDEUSEN, H. R., FENSKE, R. J., WIENKES, H. N., ENGLAND, C. G., VALDOVINOS, H. F., JEFFERY, J. J., BARNHART, T. E., SEVERIN, G. W., NICKLES, R. J., KIMPLE, M. E., MERRINS, M. J. & CAI, W. 2017. Radiomanganese PET Detects Changes in Functional beta-Cell Mass in Mouse Models of Diabetes. *Diabetes,* 66**,** 2163-2174.

HOKFELT, T., EFENDIC, S., HELLERSTROM, C., JOHANSSON, O., LUFT, R. & ARIMURA, A. 1975. Cellular localization of somatostatin in endocrine-like cells and neurons of the rat with special references to the A1-cells of the pancreatic islets and to the hypothalamus. *Acta Endocrinol Suppl (Copenh),* 200**,** 5-41.

HORNBLAD, A. & AHLGREN, U. 2009. Optical imaging of islets: New possibilities by the development of infrared fluorescent proteins. *Islets,* 1**,** 163-4.

HORNBLAD, A., CHEDDAD, A. & AHLGREN, U. 2011. An improved protocol for optical projection tomography imaging reveals lobular heterogeneities in pancreatic islet and beta-cell mass distribution. *Islets,* 3**,** 204-8.

HOU, J. C., MIN, L. & PESSIN, J. E. 2009. Insulin granule biogenesis, trafficking and exocytosis. *Vitam Horm,* 80**,** 473-506.

HUSTVEDT, S. O., GRANT, D., SOUTHON, T. E. & ZECH, K. 1997. Plasma pharmacokinetics, tissue distribution and excretion of MnDPDP in the rat and dog after intravenous administration. *Acta Radiol,* 38**,** 690-9.

IMPERIALE, A., SEBAG, F., VIX, M., CASTINETTI, F., KESSLER, L., MOREAU, F., BACHELLIER, P., GUILLET, B., NAMER, I. J., MUNDLER, O. & TAIEB, D. 2015. 18F-FDOPA PET/CT imaging of insulinoma revisited. *Eur J Nucl Med Mol Imaging,* 42**,** 409-18.

IONESCU-TIRGOVISTE, C., GAGNIUC, P. A., GUBCEAC, E., MARDARE, L., POPESCU, I., DIMA, S. & MILITARU, M. 2015. A 3D map of the islet routes throughout the healthy human pancreas. *Sci Rep,* 5**,** 14634.

IRWIN, D. M. 2001. Molecular evolution of proglucagon. *Regul Pept,* 98**,** 1-12.

JACKSON, I. M., SCOTT, P. J. H. & THOMPSON, S. 2017. Clinical Applications of Radiolabeled Peptides for PET. *Semin Nucl Med,* 47**,** 493-523.

JOHNSTON, N. R., MITCHELL, R. K., HAYTHORNE, E., PESSOA, M. P., SEMPLICI, F., FERRER, J., PIEMONTI, L., MARCHETTI, P., BUGLIANI, M., BOSCO, D., BERISHVILI, E., DUNCANSON, P., WATKINSON, M., BROICHHAGEN, J., TRAUNER, D., RUTTER, G. A. & HODSON, D. J. 2016. Beta Cell Hubs Dictate Pancreatic Islet Responses to Glucose. *Cell Metab,* 24**,** 389-401.

JUDENHOFER, M. S., WEHRL, H. F., NEWPORT, D. F., CATANA, C., SIEGEL, S. B., BECKER, M., THIELSCHER, A., KNEILLING, M., LICHY, M. P., EICHNER, M., KLINGEL, K., REISCHL, G., WIDMAIER, S., ROCKEN, M.,

NUTT, R. E., MACHULLA, H. J., ULUDAG, K., CHERRY, S. R., CLAUSSEN, C. D. & PICHLER, B. J. 2008. Simultaneous PET-MRI: a new approach for functional and morphological imaging. *Nat Med,* 14**,** 459-65.

JURGENS, C. A., TOUKATLY, M. N., FLIGNER, C. L., UDAYASANKAR, J., SUBRAMANIAN, S. L., ZRAIKA, S., ASTON-MOURNEY, K., CARR, D. B., WESTERMARK, P., WESTERMARK, G. T., KAHN, S. E. & HULL, R. L. 2011. beta-cell loss and beta-cell apoptosis in human type 2 diabetes are related to islet amyloid deposition. *Am J Pathol,* 178**,** 2632-40.

JYNGE, P., BRUROK, H., ASPLUND, A., TOWART, R., REFSUM, H. & KARLSSON, J. O. 1997. Cardiovascular safety of MnDPDP and MnCl2. *Acta Radiol,* 38**,** 740-9.

KAHN, S. E., COOPER, M. E. & DEL PRATO, S. 2014. Pathophysiology and treatment of type 2 diabetes: perspectives on the past, present, and future. *Lancet,* 383**,** 1068-83.

KAHN, S. E., PRIGEON, R. L., MCCULLOCH, D. K., BOYKO, E. J., BERGMAN, R. N., SCHWARTZ, M. W., NEIFING, J. L., WARD, W. K., BEARD, J. C., PALMER, J. P. & ET AL. 1993. Quantification of the relationship between insulin sensitivity and beta-cell function in human subjects. Evidence for a hyperbolic function. *Diabetes,* 42**,** 1663-72.

KELIHER, E. J., REINER, T., THURBER, G. M., UPADHYAY, R. & WEISSLEDER, R. 2012. Efficient (18)F-Labeling of Synthetic Exendin-4 Analogues for Imaging Beta Cells. *ChemistryOpen,* 1**,** 177-183.

KIEFFER, T. J. & HABENER, J. F. 1999. The glucagon-like peptides. *Endocr Rev,* 20**,** 876-913.

KIM, A., MILLER, K., JO, J., KILIMNIK, G., WOJCIK, P. & HARA, M. 2009. Islet architecture: A comparative study. *Islets,* 1**,** 129-36.

KIMMEL, J. R., POLLOCK, H. G. & HAZELWOOD, R. L. 1968. Isolation and characterization of chicken insulin. *Endocrinology,* 83**,** 1323-30.

KING, L. J., BURKILL, G. J., SCURR, E. D., VLAVIANOS, P., MURRAY-LYONS, I. & HEALY, J. C. 2002. MnDPDP enhanced magnetic resonance imaging of focal liver lesions. *Clin Radiol,* 57**,** 1047-57.

KINLAW, W. B., LEVINE, A. S., MORLEY, J. E., SILVIS, S. E. & MCCLAIN, C. J. 1983. Abnormal zinc metabolism in type II diabetes mellitus. *Am J Med,* 75**,** 273-7.

KNUDSEN, L. B., KIEL, D., TENG, M., BEHRENS, C., BHUMRALKAR, D., KODRA, J. T., HOLST, J. J., JEPPESEN, C. B., JOHNSON, M. D., DE JONG, J. C., JORGENSEN, A. S., KERCHER, T., KOSTROWICKI, J., MADSEN, P., OLESEN, P. H., PETERSEN, J. S., POULSEN, F., SIDELMANN, U. G., STURIS, J., TRUESDALE, L., MAY, J. & LAU, J. 2007. Small-molecule agonists for the glucagon-like peptide 1 receptor. *Proc Natl Acad Sci U S A,* 104**,** 937-42.

KODAMA, H., SHIMOJO, N. & SUZUKI, K. T. 1991. Distribution of manganese in rat pancreas and identification of its primary binding protein as pro-carboxypeptidase B. *Biochem J,* 278 (Pt 3)**,** 857-62.

KORNER, M., STOCKLI, M., WASER, B. & REUBI, J. C. 2007. GLP-1 receptor expression in human tumors and human normal tissues: potential for in vivo targeting. *J Nucl Med,* 48**,** 736-43.

KREFT, B. P., BABA, Y., TANIMOTO, A., FINN, J. P. & STARK, D. D. 1993. Orally administered manganese chloride: enhanced detection of hepatic tumors in rats. *Radiology,* 186**,** 543-8.

KREYMANN, B., WILLIAMS, G., GHATEI, M. A. & BLOOM, S. R. 1987. Glucagon-like peptide-1 7-36: a physiological incretin in man. *Lancet,* 2**,** 1300-4.

LA BARRE, J., STILL, D. U. 1930. Studies on the physiology of secretin. III Further studies on the effects of secretin on the blood sugar. *Am. J. Physiol,* 91**,** 649-653.

LACY, P. E. & DAVIES, J. 1959. Demonstration of insulin in mammalian pancreas by the fluorescent antibody method. *Stain Technol,* 34**,** 85-9.

LAGUESSE, É. 1893. Sur la formation des ilots de Langerhans dans le pancreas. *Comptes Rend Soc Biol,* 5**,** 819-820.

LAMPRIANOU, S., IMMONEN, R., NABUURS, C., GJINOVCI, A., VINET, L., MONTET, X. C., GRUETTER, R. & MEDA, P. 2011. High-resolution magnetic resonance imaging quantitatively detects individual pancreatic islets. *Diabetes,* 60**,** 2853-60.

LANE, M. A. 1907. The cytological characters of the areas of Langerhans *Am J Anat,* 7**,** 409-422.

LARSSON, L. I., SUNDLER, F., HAKANSON, R., POLLOCK, H. G. & KIMMEL, J. R. 1974. Localization of APP, a postulated new hormone, to a pancreatic endocrine cell type. *Histochemistry,* 42**,** 377-82.

LEE, Y., BERGLUND, E. D., WANG, M. Y., FU, X., YU, X., CHARRON, M. J., BURGESS, S. C. & UNGER, R. H. 2012. Metabolic manifestations of insulin deficiency do not occur without glucagon action. *Proc Natl Acad Sci U S A,* 109**,** 14972-6.

LEONI, L., DHYANI, A., LA RIVIERE, P., VOGT, S., LAI, B. & ROMAN, B. B. 2011. beta-Cell subcellular localization of glucose-stimulated Mn uptake by X-ray fluorescence microscopy: implications for pancreatic MRI. *Contrast Media Mol Imaging,* 6**,** 474-81.

LEONI, L., SERAI, S. D., HAQUE, M. E., MAGIN, R. L. & ROMAN, B. B. 2010. Functional MRI characterization of isolated human islet activation. *NMR Biomed,* 23**,** 1158-65.

LIN, W. & SONG, H. K. 2009. Improved signal spoiling in fast radial gradient-echo imaging: Applied to accurate T(1) mapping and flip angle correction. *Magn Reson Med,* 62**,** 1185-94.

LUFT, R., EFENDIC, S., HOKFELT, T., JOHANSSON, O. & ARIMURA, A. 1974. Immunohistochemical evidence for the localization of somatostatin--like immunoreactivity in a cell population of the pancreatic islets. *Med Biol,* 52**,** 428-30.

LYDEN, A., LARSSON, B. S. & LINDQUIST, N. G. 1983. Autoradiography of manganese: accumulation and retention in the pancreas. *Acta Pharmacol Toxicol (Copenh),* 52**,** 205-10.

MANANDHAR, B. & AHN, J. M. 2015. Glucagon-like peptide-1 (GLP-1) analogs: recent advances, new possibilities, and therapeutic implications. *J Med Chem,* 58**,** 1020-37.

MARSELLI, L., SULEIMAN, M., MASINI, M., CAMPANI, D., BUGLIANI, M., SYED, F., MARTINO, L., FOCOSI, D., SCATENA, F., OLIMPICO, F., FILIPPONI, F., MASIELLO, P., BOGGI, U. & MARCHETTI, P. 2014. Are we overestimating the loss of beta cells in type 2 diabetes? *Diabetologia,* 57**,** 362-5.

MATVEYENKO, A. V. & BUTLER, P. C. 2008. Relationship between beta-cell mass and diabetes onset. *Diabetes Obes Metab,* 10 Suppl 4**,** 23-31.

MCCARTHY, M. I. 2010. Genomics, type 2 diabetes, and obesity. *N Engl J Med,* 363**,** 2339-50.

MEIER, J. J., BUTLER, A. E., SAISHO, Y., MONCHAMP, T., GALASSO, R., BHUSHAN, A., RIZZA, R. A. & BUTLER, P. C. 2008. Beta-cell replication is the primary mechanism subserving the postnatal expansion of beta-cell mass in humans. *Diabetes,* 57**,** 1584-94.

MEIER, J. J., MENGE, B. A., BREUER, T. G., MULLER, C. A., TANNAPFEL, A., UHL, W., SCHMIDT, W. E. & SCHRADER, H. 2009. Functional assessment of pancreatic beta-cell area in humans. *Diabetes,* 58**,** 1595-603.

MENTLEIN, R., GALLWITZ, B. & SCHMIDT, W. E. 1993. Dipeptidyl-peptidase IV hydrolyses gastric inhibitory polypeptide, glucagon-like peptide-1(7-36)amide, peptide histidine methionine and is responsible for their degradation in human serum. *Eur J Biochem,* 214**,** 829-35.

MESCHAN, I., QUINN, J. L., WITCOFSKI, R. L. & HOSICK, T. A. 1959. The utilization of radioactive zinc and manganese in an effort to visualize the pancreas. *Radiology,* 73**,** 62-70.

MEYER, A., STOLZ, K., DREHER, W., BERGEMANN, J., HOLEBASAVANAHALLI THIMMASHETTY, V., LUESCHEN, N., AZIZI, Z., KHOBRAGADE, V., MAEDLER, K. & KUESTERMANN, E. 2015. Manganese-mediated MRI signals correlate with functional beta-cell mass during diabetes progression. *Diabetes,* 64**,** 2138-47.

MICHELOTTI, F. C., BOWDEN, G., KÜPPERS, A., JOOSTEN, L., MACZEWSKY, J., NISCHWITZ, V., DREWS, G., MAURER, A., GOTTHARDT, M., SCHMID, A. M. & PICHLER, B. J. 2020. PET/MRI enables simultaneous in vivo quantification of β-cell mass and function. *Theranostics,* 10**,** 398-410.

MIGLIORINI, A., BADER, E. & LICKERT, H. 2014. Islet cell plasticity and regeneration. *Mol Metab,* 3**,** 268-74.

MIKKOLA, K., YIM, C. B., FAGERHOLM, V., ISHIZU, T., ELOMAA, V. V., RAJANDER, J., JURTTILA, J., SAANIJOKI, T., TOLVANEN, T., TIRRI, M., GOURNI, E., BEHE, M., GOTTHARDT, M., REUBI, J. C., MACKE, H., ROIVAINEN, A., SOLIN, O. & NUUTILA, P. 2014. 64Cu- and 68Ga-labelled [Nle(14),Lys(40)(Ahx-NODAGA)NH2]-exendin-4 for pancreatic beta cell imaging in rats. *Mol Imaging Biol,* 16**,** 255-63.

MOHNIKE, K., BLANKENSTEIN, O., MINN, H., MOHNIKE, W., FUCHTNER, F. & OTONKOSKI, T. 2008. [18F]-DOPA positron emission tomography for preoperative localization in congenital hyperinsulinism. *Horm Res,* 70**,** 65-72.

MUKHERJEE, A., MORALES-SCHEIHING, D., BUTLER, P. C. & SOTO, C. 2015. Type 2 diabetes as a protein misfolding disease. *Trends Mol Med,* 21**,** 439-49.

MYERS, V. C. & BAILEY, C. V. 1916. The Lewis and Benedict method for the estimation of blood sugar, with some observations obtained in disease. *J Biol Chem,* 24**,** 147-161.

NAPIECZYNSKA, H., SEVERIN, G. W., FONSLET, J., WIEHR, S., MENEGAKIS, A., PICHLER, B. J. & CALAMINUS, C. 2017. Imaging neuronal pathways with (52)Mn PET: Toxicity evaluation in rats. *Neuroimage,* 158**,** 112-125.

NI, Y., PETRE, C., BOSMANS, H., MIAO, Y., GRANT, D., BAERT, A. L. & MARCHAL, G. 1997. Comparison of manganese biodistribution and MR contrast enhancement in rats after intravenous injection of MnDPDP and MnCl2. *Acta Radiol,* 38**,** 700-7.

NORMANDIN, M. D., PETERSEN, K. F., DING, Y. S., LIN, S. F., NAIK, S., FOWLES, K., SKOVRONSKY, D. M., HEROLD, K. C., MCCARTHY, T. J., CALLE, R. A., CARSON, R. E., TREADWAY, J. L. & CLINE, G. W. 2012. In vivo imaging of endogenous pancreatic beta-cell mass in healthy and type 1 diabetic subjects using 18F-fluoropropyl-dihydrotetrabenazine and PET. *J Nucl Med,* 53**,** 908-16.

OSTERHOLT, T., SALBER, D., MATUSCH, A., BECKER, J. S. & PALM, C. 2011. IMAGENA: Image Generation and Analysis – An interactive software tool handling LA-ICP-MS data. *International Journal of Mass Spectrometry*.

PAN, D., CARUTHERS, S. D., SENPAN, A., SCHMIEDER, A. H., WICKLINE, S. A. & LANZA, G. M. 2011a. Revisiting an old friend: manganese-based MRI contrast agents. *Wiley Interdiscip Rev Nanomed Nanobiotechnol,* 3**,** 162-73.

PAN, D., SCHMIEDER, A. H., WICKLINE, S. A. & LANZA, G. M. 2011b. Manganese-based MRI contrast agents: past, present and future. *Tetrahedron,* 67**,** 8431-8444.

PARWEEN, S., KOSTROMINA, E., NORD, C., ERIKSSON, M., LINDSTROM, P. & AHLGREN, U. 2016. Intra-islet lesions and lobular variations in beta-cell mass expansion in ob/ob mice revealed by 3D imaging of intact pancreas. *Sci Rep,* 6**,** 34885.

PEARSE, A. G. 1969. The cytochemistry and ultrastructure of polypeptide hormone-producing cells of the APUD series and the embryologic,

physiologic and pathologic implications of the concept. *J Histochem Cytochem,* 17**,** 303-13.

PEARSE, A. G. 1977. The diffuse neuroendocrine system and the apud concept: related "endocrine" peptides in brain, intestine, pituitary, placenta, and anuran cutaneous glands. *Med Biol,* 55**,** 115-25.

PERL, S., KUSHNER, J. A., BUCHHOLZ, B. A., MEEKER, A. K., STEIN, G. M., HSIEH, M., KIRBY, M., PECHHOLD, S., LIU, E. H., HARLAN, D. M. & TISDALE, J. F. 2010. Significant human beta-cell turnover is limited to the first three decades of life as determined by in vivo thymidine analog incorporation and radiocarbon dating. *J Clin Endocrinol Metab,* 95**,** E234-9.

PICTET, R. L., RALL, L. B., PHELPS, P. & RUTTER, W. J. 1976. The neural crest and the origin of the insulin-producing and other gastrointestinal hormone-producing cells. *Science,* 191**,** 191-2.

POITOUT, V. 2008. Glucolipotoxicity of the pancreatic beta-cell: myth or reality? *Biochem Soc Trans,* 36**,** 901-4.

RAHIER, J., GUIOT, Y., GOEBBELS, R. M., SEMPOUX, C. & HENQUIN, J. C. 2008. Pancreatic beta-cell mass in European subjects with type 2 diabetes. *Diabetes Obes Metab,* 10 Suppl 4**,** 32-42.

RIDDELL, C., CARSON, R. E., CARRASQUILLO, J. A., LIBUTTI, S. K., DANFORTH, D. N., WHATLEY, M. & BACHARACH, S. L. 2001. Noise reduction in oncology FDG PET images by iterative reconstruction: a quantitative assessment. *J Nucl Med,* 42**,** 1316-23.

ROCKLAGE, S. M., CACHERIS, W. P., QUAY, S. C., HAHN, F. E. & RAYMOND, K. N. 1989. Manganese(II) N,N'-dipyridoxylethylenediamine-N,N'-diacetate 5,5'-bis(phosphate). Synthesis and characterization of a paramagnetic chelate for magnetic resonance imaging enhancement. Inorganic Chemistry, 28(3), 477–485. doi:10.1021/ic00302a019 *Inorg. Chem.,* 28**,** 477–485.

RODRIGUEZ-DIAZ, R., ABDULREDA, M. H., FORMOSO, A. L., GANS, I., RICORDI, C., BERGGREN, P. O. & CAICEDO, A. 2011. Innervation patterns of autonomic axons in the human endocrine pancreas. *Cell Metab,* 14**,** 45-54.

ROED, S. N., WISMANN, P., UNDERWOOD, C. R., KULAHIN, N., IVERSEN, H., CAPPELEN, K. A., SCHAFFER, L., LEHTONEN, J., HECKSHER-SOERENSEN, J., SECHER, A., MATHIESEN, J. M., BRAUNER-OSBORNE, H., WHISTLER, J. L., KNUDSEN, S. M. & WALDHOER, M. 2014. Real-time trafficking and signaling of the glucagon-like peptide-1 receptor. *Mol Cell Endocrinol,* 382**,** 938-49.

ROUILLE, Y., MARTIN, S. & STEINER, D. F. 1995. Differential processing of proglucagon by the subtilisin-like prohormone convertases PC2 and PC3 to generate either glucagon or glucagon-like peptide. *J Biol Chem,* 270**,** 26488-96.

SAKULA, A. 1988. Paul Langerhans (1847-1888): a centenary tribute. *J R Soc Med,* 81**,** 414-5.

SCHAFER, M. K., HARTWIG, N. R., KALMBACH, N., KLIETZ, M., ANLAUF, M., EIDEN, L. E. & WEIHE, E. 2013. Species-specific vesicular monoamine transporter 2 (VMAT2) expression in mammalian pancreatic beta cells: implications for optimising radioligand-based human beta cell mass (BCM) imaging in animal models. *Diabetologia,* 56**,** 1047-56.

SCHIEBLER, T. H. & SCHIESSLER, S. 1959. [On the demonstration of insulin with the metachromatic reacting pseudoisocyanins]. *Z Zellforch Microsk Anat Histochem,* 1**,** 445-65.

SCHLYER, D. J. 2004. PET tracers and radiochemistry. *Ann Acad Med Singap,* 33**,** 146-54.

SCHMIDT, P. P., TOFT, K. G., SKOTLAND, T. & ANDERSSON, K. 2002. Stability and transmetallation of the magnetic resonance contrast agent MnDPDP measured by EPR. *J Biol Inorg Chem,* 7**,** 241-8.

SCOTT, R. A., LAGOU, V., WELCH, R. P., WHEELER, E., MONTASSER, M. E., LUAN, J., MAGI, R., STRAWBRIDGE, R. J., REHNBERG, E., GUSTAFSSON, S., KANONI, S., RASMUSSEN-TORVIK, L. J., YENGO, L., LECOEUR, C., SHUNGIN, D., SANNA, S., SIDORE, C., JOHNSON, P. C., JUKEMA, J. W., JOHNSON, T., MAHAJAN, A., VERWEIJ, N., THORLEIFSSON, G., HOTTENGA, J. J., SHAH, S., SMITH, A. V., SENNBLAD, B., GIEGER, C., SALO, P., PEROLA, M., TIMPSON, N. J., EVANS, D. M., POURCAIN, B. S., WU, Y., ANDREWS, J. S., HUI, J., BIELAK, L. F., ZHAO, W., HORIKOSHI, M., NAVARRO, P., ISAACS, A., O'CONNELL, J. R., STIRRUPS, K., VITART, V., HAYWARD, C., ESKO, T., MIHAILOV, E., FRASER, R. M., FALL, T., VOIGHT, B. F., RAYCHAUDHURI, S., CHEN, H., LINDGREN, C. M., MORRIS, A. P., RAYNER, N. W., ROBERTSON, N., RYBIN, D., LIU, C. T., BECKMANN, J. S., WILLEMS, S. M., CHINES, P. S., JACKSON, A. U., KANG, H. M., STRINGHAM, H. M., SONG, K., TANAKA, T., PEDEN, J. F., GOEL, A., HICKS, A. A., AN, P., MULLER-NURASYID, M., FRANCO-CERECEDA, A., FOLKERSEN, L., MARULLO, L., JANSEN, H., OLDEHINKEL, A. J., BRUINENBERG, M., PANKOW, J. S., NORTH, K. E., FOROUHI, N. G., LOOS, R. J., EDKINS, S., VARGA, T. V., HALLMANS, G., OKSA, H., ANTONELLA, M., NAGARAJA, R., TROMPET, S., FORD, I., BAKKER, S. J., KONG, A., KUMARI, M., GIGANTE, B., HERDER, C., MUNROE, P. B., CAULFIELD, M., ANTTI, J., MANGINO, M., SMALL, K., MILJKOVIC, I., et al. 2012. Large-scale association analyses identify new loci influencing glycemic traits and provide insight into the underlying biological pathways. *Nat Genet,* 44**,** 991-1005.

SHEN, Y., GOERNER, F. L., SNYDER, C., MORELLI, J. N., HAO, D., HU, D., LI, X. & RUNGE, V. M. 2015. T1 relaxivities of gadolinium-based magnetic resonance contrast agents in human whole blood at 1.5, 3, and 7 T. *Invest Radiol,* 50**,** 330-8.

SILVA, A. C., LEE, J. H., AOKI, I. & KORETSKY, A. P. 2004. Manganese-enhanced magnetic resonance imaging (MEMRI): methodological and practical considerations. *NMR Biomed,* 17**,** 532-43.

SIMPSON, N. R., SOUZA, F., WITKOWSKI, P., MAFFEI, A., RAFFO, A., HERRON, A., KILBOURN, M., JUREWICZ, A., HEROLD, K., LIU, E., HARDY, M. A., VAN HEERTUM, R. & HARRIS, P. E. 2006. Visualizing pancreatic beta-cell mass with [11C]DTBZ. *Nucl Med Biol,* 33**,** 855-64.

SLOOP, K. W., WILLARD, F. S., BRENNER, M. B., FICORILLI, J., VALASEK, K., SHOWALTER, A. D., FARB, T. B., CAO, J. X., COX, A. L., MICHAEL, M. D., GUTIERREZ SANFELICIANO, S. M., TEBBE, M. J. & COGHLAN, M. J. 2010. Novel small molecule glucagon-like peptide-1 receptor agonist stimulates insulin secretion in rodents and from human islets. *Diabetes,* 59**,** 3099-107.

SODDU, A., GOMEZ, F., HEINE, L., DI PERRI, C., BAHRI, M. A., VOSS, H. U., BRUNO, M. A., VANHAUDENHUYSE, A., PHILLIPS, C., DEMERTZI, A., CHATELLE, C., SCHROUFF, J., THIBAUT, A., CHARLAND-VERVILLE, V., NOIRHOMME, Q., SALMON, E., TSHIBANDA, J. F., SCHIFF, N. D. & LAUREYS, S. 2016. Correlation between resting state fMRI total neuronal activity and PET metabolism in healthy controls and patients with disorders of consciousness. *Brain Behav,* 6**,** e00424.

STEINER, D. J., KIM, A., MILLER, K. & HARA, M. 2010. Pancreatic islet plasticity: interspecies comparison of islet architecture and composition. *Islets,* 2**,** 135-45.

TALCHAI, C., XUAN, S., LIN, H. V., SUSSEL, L. & ACCILI, D. 2012. Pancreatic beta cell dedifferentiation as a mechanism of diabetic beta cell failure. *Cell,* 150**,** 1223-34.

TENG, M., JOHNSON, M. D., THOMAS, C., KIEL, D., LAKIS, J. N., KERCHER, T., AYTES, S., KOSTROWICKI, J., BHUMRALKAR, D., TRUESDALE, L., MAY, J., SIDELMAN, U., KODRA, J. T., JORGENSEN, A. S., OLESEN, P. H., DE JONG, J. C., MADSEN, P., BEHRENS, C., PETTERSSON, I., KNUDSEN, L. B., HOLST, J. J. & LAU, J. 2007. Small molecule ago-allosteric modulators of the human glucagon-like peptide-1 (hGLP-1) receptor. *Bioorg Med Chem Lett,* 17**,** 5472-8.

THOREL, F., NEPOTE, V., AVRIL, I., KOHNO, K., DESGRAZ, R., CHERA, S. & HERRERA, P. L. 2010. Conversion of adult pancreatic alpha-cells to beta-cells after extreme beta-cell loss. *Nature,* 464**,** 1149-54.

THUEN, M., BERRY, M., PEDERSEN, T. B., GOA, P. E., SUMMERFIELD, M., HARALDSETH, O., SANDVIG, A. & BREKKEN, C. 2008. Manganese-enhanced MRI of the rat visual pathway: acute neural toxicity, contrast enhancement, axon resolution, axonal transport, and clearance of Mn(2+). *J Magn Reson Imaging,* 28**,** 855-65.

TOFT, K. G., MYRSET, A. H. & SKOTLAND, T. 2001. Dephosphorylation of MnDPDP and related compounds by acid and alkaline phosphatase. *J Pharm Biomed Anal,* 25**,** 613-8.

TONG, S., ALESSIO, A. M. & KINAHAN, P. E. 2010. Image reconstruction for PET/CT scanners: past achievements and future challenges. *Imaging Med,* 2**,** 529-545.

TOPPING, G. J., YUNG, A., SCHAFFER, P., HOEHR, C., KORNELSEN, R., KOZLOWSKI, P. & SOSSI, V. 2017. Manganese concentration mapping in the rat brain with MRI, PET, and autoradiography. *Med Phys,* 44**,** 4056-4067.

VILLIGER, M., GOULLEY, J., MARTIN-WILLIAMS, E. J., GRAPIN-BOTTON, A. & LASSER, T. 2010. Towards high resolution optical imaging of beta cells in vivo. *Curr Pharm Des,* 16**,** 1595-608.

WANG, C. 1998. Mangafodipir trisodium (MnDPDP)-enhanced magnetic resonance imaging of the liver and pancreas. *Acta Radiol Suppl,* 415**,** 1-31.

WANG, H. Z., RIEDERER, S. J. & LEE, J. N. 1987. Optimizing the precision in T1 relaxation estimation using limited flip angles. *Magn Reson Med,* 5**,** 399-416.

WANG, X., MISAWA, R., ZIELINSKI, M. C., COWEN, P., JO, J., PERIWAL, V., RICORDI, C., KHAN, A., SZUST, J., SHEN, J., MILLIS, J. M., WITKOWSKI, P. & HARA, M. 2013. Regional differences in islet

distribution in the human pancreas--preferential beta-cell loss in the head region in patients with type 2 diabetes. *PLoS One,* 8**,** e67454.

WICKI, A., WILD, D., STORCH, D., SEEMAYER, C., GOTTHARDT, M., BEHE, M., KNEIFEL, S., MIHATSCH, M. J., REUBI, J. C., MACKE, H. R. & CHRISTOFORI, G. 2007. [Lys40(Ahx-DTPA-111In)NH2]-Exendin-4 is a highly efficient radiotherapeutic for glucagon-like peptide-1 receptor-targeted therapy for insulinoma. *Clin Cancer Res,* 13**,** 3696-705.

WIERUP, N., SVENSSON, H., MULDER, H. & SUNDLER, F. 2002. The ghrelin cell: a novel developmentally regulated islet cell in the human pancreas. *Regul Pept,* 107**,** 63-9.

WILD, C., CUNNINGHAM, K. A. & ZHOU, J. 2014. Allosteric Modulation of G Protein-Coupled Receptors: An Emerging Approach of Drug Discovery. *Austin J Pharmacol Ther,* 2.

WILD, D., BEHE, M., WICKI, A., STORCH, D., WASER, B., GOTTHARDT, M., KEIL, B., CHRISTOFORI, G., REUBI, J. C. & MACKE, H. R. 2006. [Lys40(Ahx-DTPA-111In)NH2]exendin-4, a very promising ligand for glucagon-like peptide-1 (GLP-1) receptor targeting. *J Nucl Med,* 47**,** 2025-33.

XU, Q., ZHU, C., XU, Y. P., PAN, D. H., LIU, P., YANG, R. L., WANG, L. Z., CHEN, F., SUN, X. C., LUO, S. N. & YANG, M. 2015. Preliminary evaluation of [F-18]AIF-NOTA-MAL-Cys(39)-exendin-4 in insulinoma with PET. *Journal of Drug Targeting,* 23**,** 813-820.

ZALEWSKI, P. D., MILLARD, S. H., FORBES, I. J., KAPANIRIS, O., SLAVOTINEK, A., BETTS, W. H., WARD, A. D., LINCOLN, S. F. & MAHADEVAN, I. 1994. Video image analysis of labile zinc in viable pancreatic islet cells using a specific fluorescent probe for zinc. *J Histochem Cytochem,* 42**,** 877-84.

10Declaration of Contribution

The dissertation work was carried out at the Department of Preclinical Imaging and Radiopharmacy within the Radiology at the University Hospital Tübingen under the supervision of Prof. Bernd J. Pichler.

10.1 Establishment of *In vivo* PET/ME-MRI Protocols

Filippo C. Michelotti designed the phantom studies and optimized the MR protocols for the acquisition of contrast-enhanced MR images. Filippo C. Michelotti implemented the MATLAB script used for the evaluation of multiple combination of flip angles. Barbara Schoerg carried out the breeding and the selection of control and transgenic RIP1-Tag2 mice. Radiolabeling of Ex4 and quality control were carried out by Dr. Gregory Bowden. Filippo C. Michelotti designed and carried out the PET/MRI experiments. Filippo C. Michelotti designed and performed the image data analysis. Dr. Andreas M. Schmid and Prof. Bernd J. Pichler supervised the progress of research.

10.2 Simultaneous PET/MRI Measures BCM and Function

The screening and the breeding of RIP1-Tag2 mice was performed by Barbara Schoerg. The radiolabeling of the PET tracer and quality control were evaluated by Dr. Gregory Bowden. The PET/MRI experiments were designed and carried out by Filippo C. Michelotti. The autoradiography was carried out by Filippo C. Michelotti. Astrid Zimmerman and Dr. Volker Nischwitz performed ICP-MS imaging of biometals. Image data analysis was designed and performed by Filippo C. Michelotti. Dr. Jonas Maczewsky. and Prof. Gisela Drews carried out and evaluated the insulin secretion assay. Dr. Andreas M. Schmid, Dr. Andreas Maurer, Prof. Martin Gotthardt and Prof. Bernd J. Pichler supervised and discussed the progresses of research.

10.3 Monitor of Islet Cell Engraftment by PET/MRI

Dr. Wael Eter carried out the isolation and the transplantation of islet cells. The radiolabeling of the PET tracer was performed by Dr. Gregory Bowden. The PET/MRI experiments, the autoradiography and the biodistribution study were designed and conducted by Filippo C. Michelotti. The analysis of PET/MR images, autoradiography and ICP-MS images was performed by Filippo C. Michelotti. The research outcome was supervised by Dr. Andreas M. Schmid, Dr. Andreas Maurer, Prof. Martin Gotthardt and Prof. Bernd J. Pichler.

10.4 Radioactive ^{52}Mn as Potential Dual PET/MRI Agent to Measure the Endocrine Pancreas

Dr. Jesper Fonslet carried out the production of ^{52}Mn. Gregory Bowden performed the synthesis of DPDP and the radiolabeling with ^{52}Mn. Filippo C. Michelotti designed and carried out the PET experiments. The autoradiography and the biodistribution studies were conducted and analyzed by Filippo C. Michelotti and Dr. Hanna Napieczynska. The analysis of PET was performed by Filippo C. Michelotti. The progress of research was discussed and supervised by Dr. Andreas M. Schmid, Dr. Andreas Maurer and Bernd J. Pichler.

10.5 PET Imaging to Investigate the Effect of a Quinoxaline Derivative

The PET experiments were designed by Dr. Gregory Bowden and Filippo C. Michelotti. The radiolabeling of the PET tracer was performed by Dr. Gregory Bowden. The PET and the biodistribution studies were conducted by Filippo C. Michelotti. Data analysis was performed by Filippo C. Michelotti. The progress of research was discussed and supervised by Dr. Valerie Honndorf-Schmit, Dr. Andreas Maurer, Dr. Andreas M. Schmid, Prof. Martin Gotthardt and Prof. Bernd J. Pichler.

Date / Signature

11Publications

Michelotti F. C., Bowden G., Küppers A., Joosten L., Maczewsky J., Nischwitz V., Drews G., Maurer A., Gotthardt G., Schmid A. M., Pichler B. J., *"PET/MRI enables simultaneous in vivo quantification of β-cell mass and function"*, *Theranostics* 2020;10(1):398-410

12Acknowledgments

Thanks to Gregory Bowden, Brett Buttliere and Hanna Höhne for proofreading the dissertation.

I thank Sandro Aidone, Funda Cay, Maren Harant and Natalie Mucha for their valuable technical assistance. Thanks to Andi, Chamba, Hanna, Sabina, Prateek and Jonathan for the fruitful scientific discussions.

The research of these studies has received funding from the European Research Council under the European Union's Seventh Framework Programme (FP7/2007-2013) grant agreement n° 289932 BetaTrain and by the Deutsche Forschungsgemeinschaft (DFG, German Research Foundation) under Germany's Excellence Strategy - EXC 2180 - 390900677.